Universidad de Oviedo

Optical Studies in Van der Waals Heterostructures using Micro-Photoluminiscence

Master's Thesis
Master's Degree in Advanced Physics: Particles, Astrophysics, Nanophysics and Quantum Materials
Academic Course 2023-2024

Author:
Pablo García García

Cotutors:
Javier Martín Sanchez
Aitana Tarazaga Martín-Luengo

Agradecimientos

Me gustaría expresar mi agradecimiento a Javier Martín y Aitana Tarazaga por su gran apoyo durante la realización de este trabajo. Valoro mucho todo lo que me han enseñado estos dos años, así como todas las conversaciones y reuniones que hemos compartido. Su entusiasmo y dedicación a este tema de investigación han sido fundamentales para ilusionarme y enamorarme con la nanoóptica.

También me gustaría agradecer a todo el grupo de Nanoóptica, especialmente a Abel y Adam, por soportar otro año más mis preguntas y dudas, por dedicarme su tiempo de manera tan generosa y por todo lo que me han enseñado durante la realización de este trabajo.

Por último, agradezco a mis seres queridos que me han acompañado durante este camino, sin ellos no estaría donde estoy ni sería quien soy.

Contents

1 Introduction

When working on a Master's thesis, there's always one simple question on everyone's mind: What exactly do you do on your master's thesis? The short answer for non-physicists is: "I play with Scotch tape to make very thin materials, put them together and then shoot them with lasers and see what happens". This may be an oversimplification, but it is a very accurate description of the basic activities of this research.

For those with a background in physics, a more rigorous description is required. This research focuses on transition metal dichalcogenides (TMDs), a family of semiconductors characterised by a layered structure that can be mechanically exfoliated down to a monolayer. In this single layer condition, TMDs exhibit a direct band gap within the visible spectrum and are therefore very suitable for optical studies. In addition, TMDs support the formation of excitonic quasiparticles at room temperature, which can lead to significant light absorption and complex light-matter interactions. In this context, this Master's thesis will focus on studying the fabrication process of these heterostructures and their characterization by micro-photoluminescence to study their optical emission properties.

Since the groundbreaking isolation of graphene by mechanical exfoliation in 2004, the field of 2D materials has expanded dramatically. Graphene's exceptional carrier mobility marked it as a potential game-changer for electronic applications, despite its intrinsic limitation as a bandgap-less semi-metal, making it unsuitable for optoelectronics or photonics. TMDs, on the other hand, are layered semiconductor materials composed of transition metals (e.g. tungsten or molybdenum) and chalcogens (e.g. sulphur, selenium or tellurium). Unlike graphene, as TMDs in their monolayer form have a direct band gap, they are promising candidates for applications in electronics and optoelectronics.

TMDs are van der Waals materials, which means that their layers are held together by weak van der Waals forces, allowing them to be easily exfoliated into atomically thin, flat layers. It has been shown that stacking layered materials to obtain heterostructures is a very powerful method to tailor their properties, combine them and also induce new ones.

This work aims to exploit these properties by stacking different 2D materials to create heterostructures with tailored optical properties. Mechanical exfoliation and dry transfer techniques are employed to create heterostructures with precise layer control. Specifically, heterostructures composed of hexagonal boron nitride (hBN), tungsten disulfide (WS_2), and tungsten diselenide (WSe_2) are fabricated. The hBN layers serve as encapsulating materials to preserve the intrinsic properties of the TMD layers from environmental contamination and to provide an atomically flat substrate, crucial for high-quality optical measurements.

Photoluminescence (PL) spectroscopy is the characterization tool used to probe the optical emission properties of these heterostructures. We conduct a detailed analysis of their optical emission properties, focusing on the effects of thermal annealing and the geometry of the heterostructures. Our experimental findings suggests that the emission characteristics are dependent on the quality of the hBN encapsulation and the structural arrangement of the TMD layers.

To explore the fundamental optical properties and excitonic behavior, we conduct low temperature experiments at 4K. These experiments reveal the formation of different species of interlayer and moiré excitons within the heterostructures and their dependence to incident power and polarization, providing insights into their potential origins and implications for future electronic and optoelectronic devices.

2 Theoretical overview

2.1 Optical processes in semiconductors

A semiconductor is a type of material whose electrical conductivity lies between that of a conductor and an insulator. The key characteristic of semiconductors is that their conductivity can be precisely controlled by adding impurities (doping) and by applying electromagnetic fields, light, or heat.

In the field of photonics, semiconductors play a crucial role due to their efficient interaction with light. They can absorb photons to create electron-hole pairs (charge generation) or emit photons when electrons and holes recombine (light emission). These properties are fundamental to devices such as light-emitting diodes (LEDs), solar cells, lasers and photodetectors. The ability to adjust the band gap is specially important for photonics applications since it determines the wavelengths of light the material can absorb or emit. By using materials with different band gaps, structures can be designed for particular applications.

The optical properties of semiconductors have a great importance in the field of solid state physics. By analyzing the response of materials when illuminated by different light sources, we can obtain a great deal of information about their fundamental properties. Photoluminescence (PL) spectroscopy is particularly valuable for studying the band structure and excited states that can form and then emit light from the material, using light of sufficient energy to excite electrons over the optical band gap of a material.

This section will introduce the processes of photon absorption and emission that underlie photoluminescence , establishing a foundation for understanding how these interactions reveal information about the band structure and excited states of the materials.

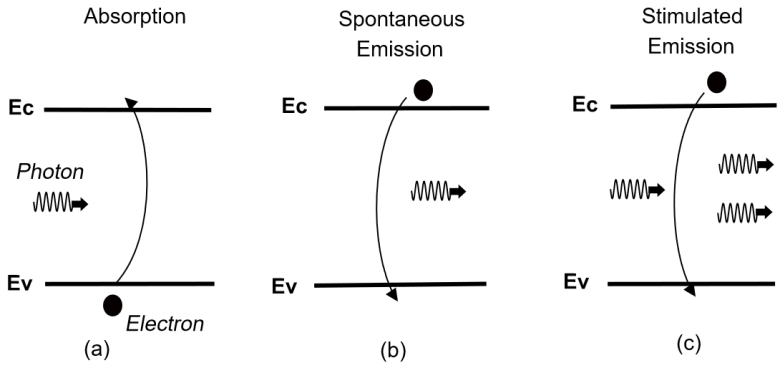

Figure 1: Energy band diagrams of a band gap semiconductor showing (a) photon absorption, (b) spontaneous emission and (c) stimulated emission. The upper band is the conduction band minimum, and the lower band is the valence band maximum.

2.1.1 Absorption processes

Figure 1.a shows a process of photon absorption in a semiconductor. Here, a photon incident on a sample can be absorbed and excite an electron from the lower energy valence band to the higher energy conduction band. The energy (E) and momentum (p) of the photon are given by the Planck-Einstein and de Broglie relations (Equation 1), where h is Planck's constant, c

is the speed of light and λ is the wavelength of the photon. The removal of an electron from the valence band leaves an empty state as an absence from the otherwise filled valence band. This absence may be treated as a quasi-particle, and is commonly known as a hole [1].

$$E = \frac{hc}{\lambda} = pc \tag{1}$$

In order for such a transition to occur, there must be an electron in the valence band and an unoccupied state at higher energy into which the electron can be excited. For an ideal semiconductor, this means fulfilling the following conditions:

The energy of the incident photon must be at or above the band gap energy, the energy difference between the highest energy point in the valence band and the lowest energy point in the conduction band. As these two points might not share the same value of k, there is also a need to conserve crystal momentum [2], imposing selection rules on the possible transitions that can occur.

In order for an absorption process to occur involving only an electron-hole and a photon, the wave vectors ($k = p/\hbar$) of the valence band wave function and the wave vector of the conduction band must differ by the wave vector of the photon. From Equation 1, we can calculate the wave vector of a photon in the visible wavelength to be 3 orders of magnitude smaller than the difference in the wave vectors of the indirect-band-gap structure, thus the only possible transitions are then between initial and final states of the same wave vector ($k_i = k_f$) and are called direct transitions (in k-space as displayed on Figure 2.a).

When the conduction band minimum and the valence band maximum are not the same value of k, assistance of a photon in necessary in order for the transition to conserve crystal momentum. This type of transition is called indirect (Figure 2.b). The requirement of an additional quasi-particle in the process reduces the probability of the transition occurring, greatly reducing the rate of absorption of photons at the band gap energy. However, for absorption processes with photon energies further away for the gap, higher energies band states are present in different k-positions, allowing some direct absorption transitions to occur in indirect band gap materials

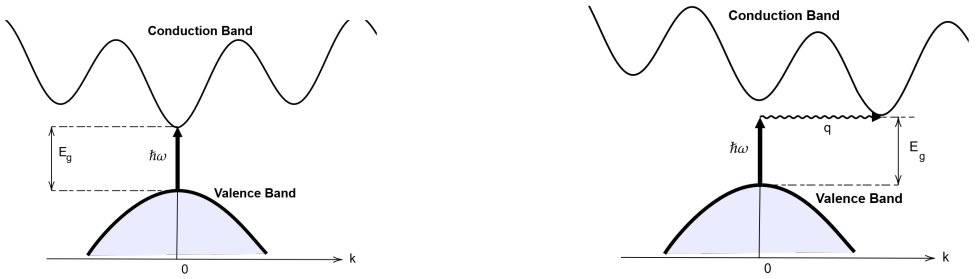

Figure 2: Inter band transitions in semiconductors with a E_g band gap.(a) Direct Transition (b) Indirect Transition. The vertical arrow represents the photon absorption process $\hbar\omega$, while the curved arrow in represents the absorption or emission of a phonon q.

2.1.2 Emission processes

Figure 1.b shows a process of spontaneous photon emission in a semiconductor. The process may be described as the reverse of the absorption process. Here, an electron from the conduc-

tion band recombines with a hole in the valence band, emitting a photon. The selection rules previously described are equally applicable to this case. Accordingly, energy and momentum must be preserved in any transition. As a result, recombination processes occur with greater frequency in direct band gap semiconductors than in indirect band gap semiconductors.

In general, it is important to take into account that although we have previously assumed that the energy of the emitted photon from the band to band recombination corresponds to the energy of the band gap, in practice, as due to a non-zero thermal energy electrons and holes reside slightly above and below their band energy, the photon energy emitted will be slightly larger or smaller than the band gap energy [2]. This broadening of the emission energy can be described by the combination of the density of states (Equation 2) and the Boltzmann distribution (Equation 3) visualized in Figure 3, thus giving a half power width in energy of around $1.8k_BT$, which in the emission in the middle of the visible wavelength of light the spectrum width is around 10 nm at 300K, calculated in the approximate relation given in Equation 4.

$$N(E) = \frac{(2m_r^*)^{3/2}}{2\pi^2\hbar^3}\sqrt{E - E_g} \tag{2}$$

$$F(E) = \exp -\frac{E}{k_BT} \tag{3}$$

$$\Delta\lambda \approx \frac{1.8k_BT\lambda^2}{hc} \tag{4}$$

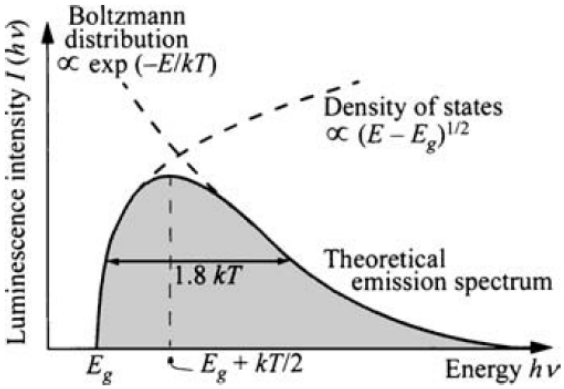

Figure 3: Theoretical spectrum of spontaneous emission [2]

Figure 1.c shows a process of stimulated photon emission in a semiconductor. When a photon of energy $h\nu$ interacts with an atom that is in an excited state, the electron is stimulated to make its transition into the ground state and gives off another photon of the same wavelength and in phase with the incident radiation [2]. This effect has two interesting properties. Firstly, one photon input is needed giving rise to two photons in the output, thus optical gain is achieved. Secondly, the two photons are in phase, making the output coherent. These two properties make stimulated photon emission the process laser devices rely on to produce high intensity light at a narrow wavelength width.

2.1.3 Photoluminescence

The photoluminescence (PL) phenomenon involves the combination of absorption and emission processes, which are used to probe the value of the band gap and electronic levels in semiconductor materials. The underlying mechanism for PL is illustrated in Figure 4.

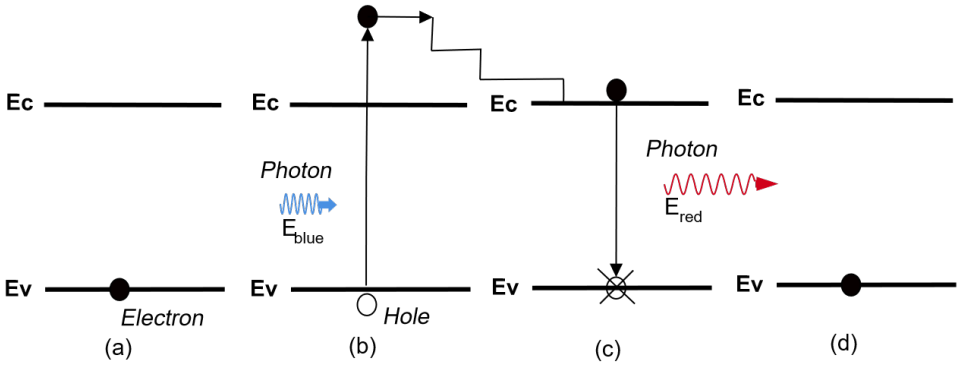

Figure 4: Steps of the photoluminescence process: (a) before absorption an electron is on the valence band, (b) absorption of a photon exciting an electron into the conduction band and creating a hole in the valence band, (c) radiative recombination of the electron and hole emitting a photon, (d) ground state with an electron on the valence band.

A light source, typically a laser, is used to illuminate a sample with photons whose energy is equal to or greater than the band gap of the material. In the majority of experiments, the laser is selected to have a high enough energy above the band gap, ensuring the emitted spectrum can be distinguished from the excitation source without interference [3].

In this process, the laser excites electrons to energies above the band gap, creating holes in the valence band. These charge carriers then relax to the border of the conduction and valence gaps through non-radiative transitions, where it is energetically favourable for them to reside, and eventually recombine, emitting a photon with energy close to the band gap.

The emission spectrum on an idealized semiconductor shows a sharp cutoff for energies below the band gap as there are no possible states available for the electron or the hole to reside inside the band gap of the material. This results in no photoluminiscence emission at energies below the band gap as shown in Figure 3. However, in a real semiconductor (or insulator) we can have the presence of defects in the crystal eventually introducing discrete electronic levels within the band gap, allowing relatively narrower additional optical emission peaks for energies below the band gap. These emissions can be due to the recombination of electron and holes either between individual electronic levels or from the edges of the bands to the electronic levels. Some of these defects can fit only one electron in their excited state, giving rise to single photon emission, a phenomenon specially important for applications in quantum photonics [4].

In summary, PL experiments provide insightful information about the optical band gaps, the presence of defects and the recombination processes of charge carriers in materials. Therefore, in the context of the present work, this technique is used experimentally to investigate the optical emission in novel TMD heterostructures in Section 2.1.3. In addition, the presence of exotic electron-hole bound states, the excitons (as discussed in Section 2.1.4), will also be studied by means of this technique.

2.1.4 Excitons

So far, electrons and holes in the material have been regarded as essentially free particles (or quasi-particles for the holes) that do not interact with each other. However, the reality is that charged particles do interact with each other through attractive and repulsive forces. The most relevant of these forces is the attractive Coulomb force between two oppositely charged carriers, namely, between an electron with a negative charge and a hole with a positive charge. When these are in close proximity, Coulomb forces will attract them towards each other, allowing the formation of a bound electron-hole pair, known as an exciton [1]. An exciton can move through a crystal and transport energy. However, it does not transport charge because it is electrically neutral.

Due to the Coulomb interaction between the electron and the hole that form the exciton, the emission energy of their recombination is different from the one that would be expected from the recombination of free electrons and holes. Namely, it is slightly lower than the energy of the band gap. The difference between the exciton emission energy and the band gap represents the binding energy of the exciton, which can be in the range of a few meV to eV. For instance, in commonly used III-IV semiconductor bulk materials, excitonic binding energies are in the order of up to tens of meV (4.2 meV for GaAs [1]). As this binding energy is much smaller than thermal energy at room temperature (≈30 meV), excitons can only reliably form at low temperatures in these materials.

In materials with a relatively low dielectric constant, the Coulomb interaction between an electron and a hole can be quite strong. This strong interplay results in excitons that are tightly bound and small in size, often comparable to the size of the unit cell of the material. In such cases the excitons, known as Frenkel excitons, are typically highly localised. They can even be completely confined to a single molecule, as is the case in materials such as fullerenes. The Frenkel exciton is characterised by its high binding energy, typically in the range of 0.1 to 1 eV in bulk materials. This high binding energy reflects the strong electron-hole interaction in materials with low dielectric constants. [1]

In semiconductors and other materials with relatively high dielectric constants, the scenario is quite different. The large dielectric constant leads to significant screening of the electric field, which in turn reduces the electron-hole Coulomb interaction. As a result, the excitons in these materials tend to be much less tightly bound and more delocalized. This type of exciton is known as a Wannier-Mott exciton. The Wannier-Mott exciton has a radius that is typically much larger than the lattice spacing of the material. This delocalization occurs because the reduced Coulomb interaction allows the electron and hole to be separated by a greater distance while still remaining bound. Additionally, the small effective mass of the electrons in semiconductors further contributes to the larger exciton radius. The effective mass is reduced due to the influence of the crystalline potential, which modifies the electron and hole masses in a way that favors larger spatial separation and thus larger exciton radii. The Wannier Mott exciton is characterised by its lower binding energy, typically in the range of 10-30 meV in bulk semiconductor materials. [1]

2.2 2D Materials

The isolation of a single layer of graphite, known as graphene, in 2004 marked the beginning of the field of two-dimensional (2D) materials. Bulk van der Waals (vdW) materials exhibit a layered structure in which the atoms in the monolayers exhibit strong in-plane covalent bonds, while the individual monolayers are held together by relatively weak out-of-plane van der Waals forces. As a consequence, single layers (monolayers) can be easily obtained from bulk

crystals by mechanical exfoliation. These monolayers usually present outstanding physical properties quite different from those found in their bulk counterpart [5]: 2D materials can exhibit semi-metallic, semiconducting, superconducting and topological insulators properties. These monolayers are stable, atomically flat and lack dangling bonds, a key reason why many other bulk materials cannot be reduced to atomic layers.

A common feature of two-dimensional materials is their exceptional mechanical properties, such as a high tensile strength or Young's modulus, which allows them to be used both as a mechanical reinforcement material and in the creation of flexible electronic devices. As a monolayer, they exhibit high resistance to lattice strain, with values of up to 11% in MoS_2[6]. Extremely high strength-to-weight ratios are achieved through the atomic thinness, as each atom in the material is actively involved in providing mechanical stability and increasing the overall strength of the material. Contributing to the material's exceptional mechanical properties, covalent bonds are highly stable and resistant to deformation and fracture.

Two-dimensional (2D) materials represent a new frontier in materials science, covering a wide range of material types including semiconductors, insulators, conductors and superconductors (Figure 5). These materials, including graphene, tungsten disulfide (WS_2), hexagonal boron nitride (hBN) and others, have the potential to serve as the basis for new multifunctional and flexible technologies due to their atomically thin structure.

One of the most remarkable features of 2D materials is their versatility in combining different physical properties without the need for complex alloying processes or chemical compounds. By stacking different layers of 2D materials, it is possible to create heterostructures with adjustable and customised properties. This ability to stack and tune at the atomic level enables the design of devices with specific functionalities by combining the properties present in different materials.

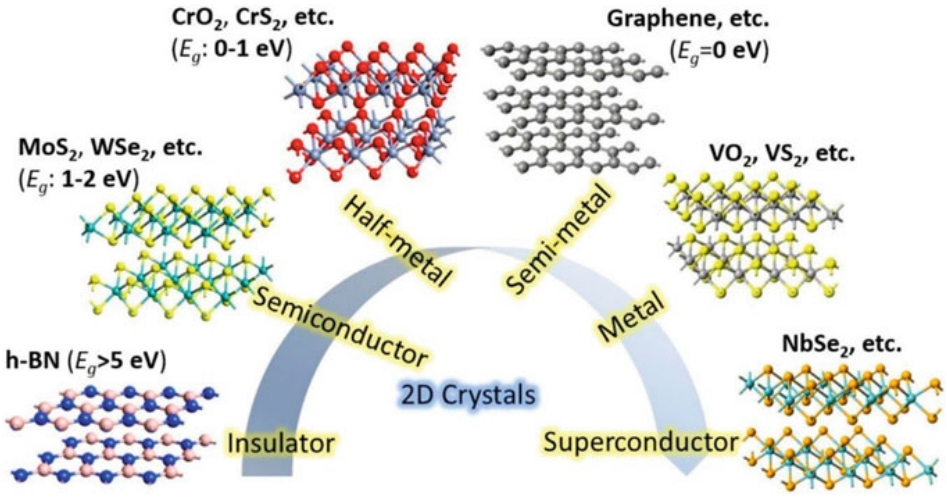

Figure 5: Different Types 2D Materials by their electronic properties and examples [7].

In this section we will introduce the optical properties of Transition Metal Dichalcogenides (TMDs), focusing on the naturally semiconducting TMDS, which can all be thinned down to the monolayer limit. We will discuss excitons in these materials and the reason why these materials are particularly interesting for studying novel physics phenomena and future optoelectronic applications. Finally, we will discuss possible exciton species that can also appear in TMDs.

2.2.1 Transition Metal Dichalcogenides

Transition Metal Dichalcogenides exhibit different bulk structural phases: 1T (octahedral) and 2H (trigonal prismatic). This work has focused exclusively on TMDs of the 2H phase as it is the most stable configuration. Figure 6 illustrates the 2H phase, showing the structure of a single layer and the stacking arrangement observed between two layers. A single layer of a TMD consists of strongly bonded MX_2 atoms, where X is the chalcogen atom, such as sulphur or selenium, and M is the transition metal, typically tungsten or molybdenum.TMD crystals consist of a triangular lattice structure with a three atom basis per unit cell, where one metal atom is sandwiched in between two chalcogen atoms (X-M-X) via strong covalent bonds. The atoms are arranged such that when considering a transition metal element, six chalcogen atoms are bonded to it in a trigonal prismatic arrangement. These layers are attached through weak Van der Waals forces to form a 3D structure.

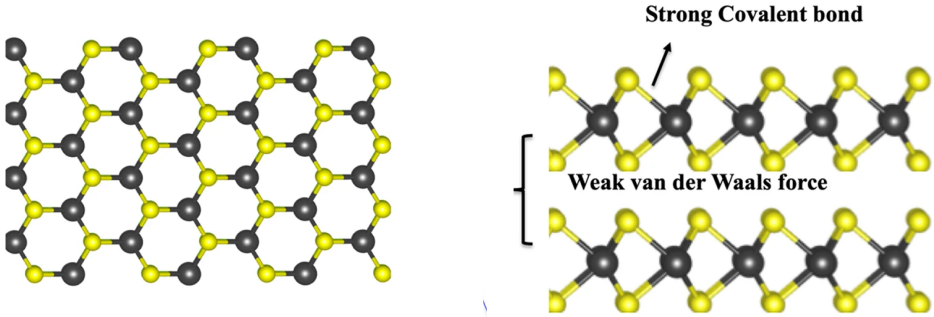

(a) *(b)*

Figure 6: 2H TMD molecular structure and stacking for a natural bilayer. Black spheres represent transition metal atoms while yellow spheres represent the chalcogen atoms. (a) Top View, (b) Side View. Adapted from [8]

Both the number of layers in a sample and the arrangement of atoms inside a single layer dictate the band structure and, in turn, the optical properties of TMDs [9]. Since bulk crystals made up of several TMD layers have an indirect band gap [10], optical emission is weak, limiting their optical applications. However, when the number of layers decreases, the band structure changes greatly, turning TMDs into direct band gap semiconductors at the monolayer limit (Figure 7).

Finally, in Figure 8 we can see a brief history and many applications of the applications that are currently being researched using TMD-based devices in the field of photonics and optoelectronics, ranging from single and few layer phototransistors [13], ultra sensitive photodectors [14], photovoltaic cells based on a p-n union of heterostructures [15], high quantum yield photoluminescence emitters [16] to new methods to study emerging physics phenomena such as valleytronics [17] (valley-selective optical excitation) and the emission of quantum light from localized states [18]

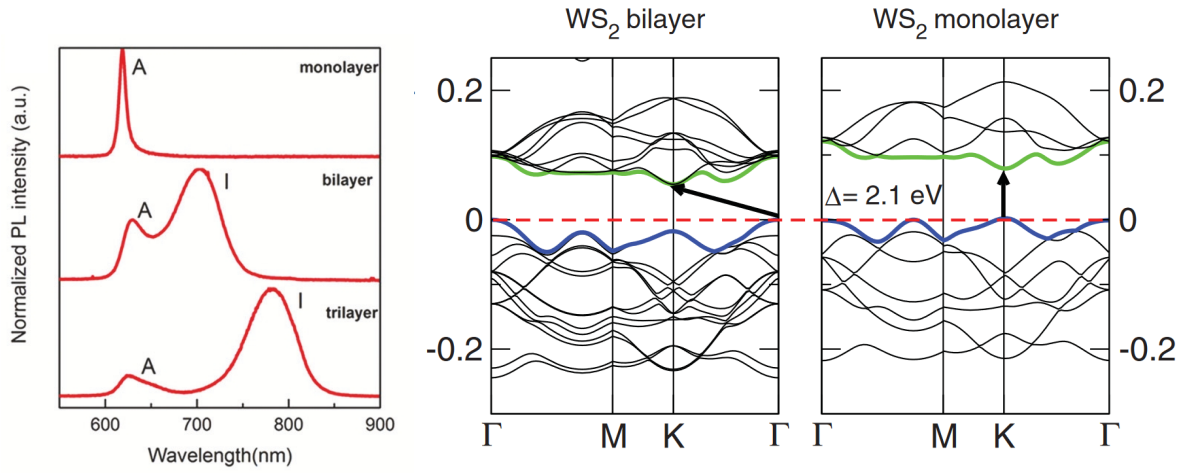

(a) *(b)*

Figure 7: (a) Photoluminescence spectra in relation to the number of layers for WS_2 . Indirect (bilayer) to direct (monolayer) transition. A: direct emission peak. I: indirect emission peak [11]. (b) Band Structure of WS_2 bilayer and monolayer. Black arrow: Γ to K indirect transition in bilayer; K to K direct transition in monolayer. Δ Band Gap energy (Adapted from [12])

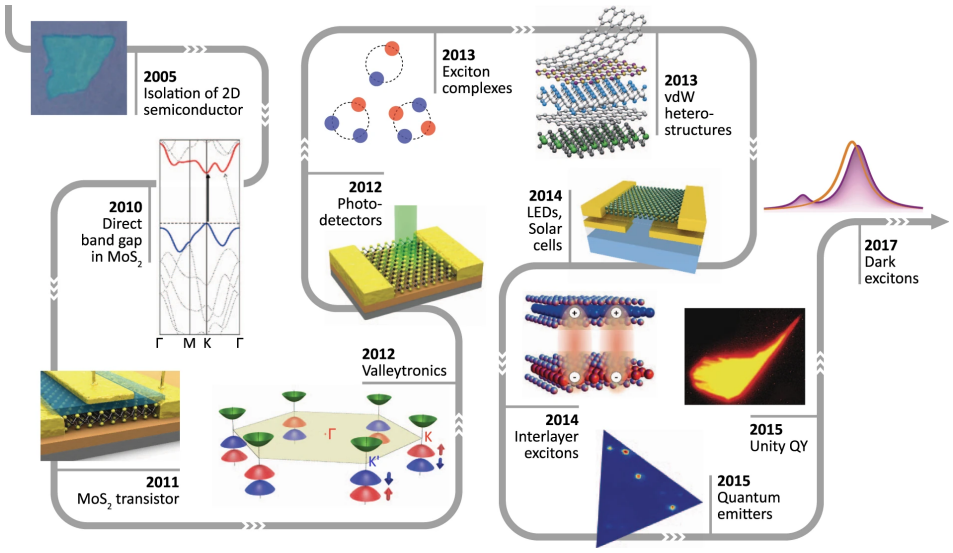

Figure 8: history of TMD exciton optics and optoelectronics[19]

2.2.2 Excitons in TMDs

For excitons in semiconducting TMDs, the estimated size of the Bohr radius is in the order of 1 to a few nm, which extends over a few lattice periods [20] (Figure 9). Although the semiconductor TMD has strongly bound excitons, since the Bohr radius of the excitons is many times the lattice constant, the Mott-Wannier picture adequately describes the excitonic behavior in the TMD.

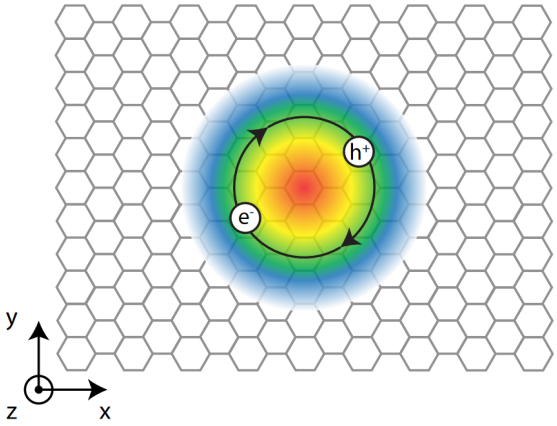

Figure 9: A Mott-Wannier exciton in a hexagonal lattice. Size of the exciton is approximately to scale with the lattice size. [20]

For Mott-Wannier excitons, we can calculate an approximate binding energy as the hydrogen atom problem inside a dielectric medium. In the simplest picture, we can solve for the binding energy using the locally screened Coulomb potential [20] given in Equation 5 where e is an electron charge, ϵ_{eff} is the effective dielectric constant of the lattice, and ϵ_0 is the vacuum permittivity.

$$V_{coulomb} = -\frac{1}{4\pi\epsilon_0}\frac{e^2}{\epsilon_{eff}r} \tag{5}$$

Solving for the energy eigenvalues in 2D, the binding energy of the exciton and its Rydberg series with quantum number n are shown in Equation 6, taking into account that the Rydberg series is defined by n - 1/2 in 2D. This is the energy required to dissociate the exciton, i.e. to return the electron and hole to the conduction and valence bands of the free particle, respectively. The emission energy is the energy of the emitted photon during the emission process and is defined by the difference between the band gap (E_{gap}) and the binding energy $E_\gamma^n = E_{gap} - E_b^n$. As the energy of most excitons correspond to their first excited state (n= 1), we can estimate the binding energy and Bohr radius using this state.

$$E_b^n = (\frac{1}{4\pi\epsilon_0})^2\frac{\mu e^4}{2\hbar^2\epsilon_{eff}^2(n-1/2)^2} \tag{6}$$

$$a_B = \frac{4\pi\epsilon_{eff}\epsilon_0\hbar^2}{\mu e^2} \tag{7}$$

Thus, taking into account Equation 7 and given $1/\mu = 1/m_e + 1/m_h$ the reduced mass we can estimate the Bohr radius of our exciton. Using equal effective electron and hole masses of $\approx 0.50m_0$ [21] and $\epsilon_{eff} \approx 20$ [22] for WSe_2, we can approximate a binding energy of $E_b \approx 700meV$, and a Bohr radius of $a_B \approx 0.8nm$. The large binding energy means that temperatures exceeding thousands of Kelvin are needed to thermally dissociate the exciton, ensuring radiative recombination at ambient temperature. Additionally, the relatively small Bohr radius indicates that the exciton is tightly bound around a few dozen unit cells. Another consequence of the large binding energies is the very short radiation lifetime of the excitons of about 0.3 ps to 3 ps at low temperatures. These lifetimes are ultra-fast, resulting in bright exciton emission in atomically thin material. In direct band gap materials, recombination or

absorption can be very efficient, allowing clear optical detection of the excitonic states and high PL emission.

Excitons are highly dependent on the dielectric screening. When there is no material on top (or bottom) of the material, the dielectric constant can be assumed that of air, greatly reducing dielectric screening, allowing longer range interactions between charged particles and higher excitonic binding energies (Figure 10). With the reduction of dielectric screening, by the relation given in Equation 6, we can see how there is an increase in the binding energy. That way, when binding energies are sufficiently large (i.e. dielectric screening is low enough), radiative recombination of excitons can occur at room temperature. This is the process that allows monolayers to show excitonic emission even at room temperature. This reduction also allows for charged particles inside the atomic layer to interact with other particles in the environment: another atomic layer or measurable environmental particles

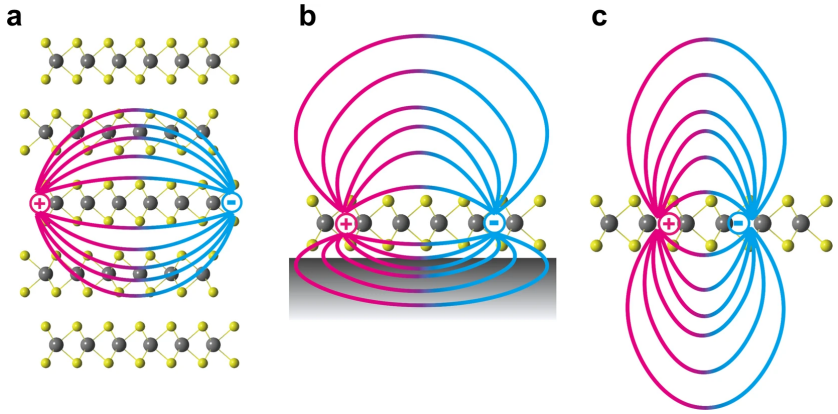

Figure 10: Schematic illustration of the dielectric screening of Coulomb interaction. (a) Increased dielectric screening in a bulk material, (b) Dielectric screening reduced at the top of a monolayer when deposited on a substrate, (c) Reduced dielectric screening on a free monolayer [23]

2.2.3 Charged excitons and biexcitons

So far, only the simplest type of exciton that be observed in TMDs has been considered: The neutral exciton, which consists of a single electron bound to a single hole. In addition to this neutral exciton, three more excitonic complexes can be observed in TMDs involving additional charge carriers: charged excitons or trions and biexcitons.

A trion is a charged exciton consisting either of two electrons and one hole, for a negatively charged trion, or two holes and one electron, for a positively charged trion. Observing such trions depends on the relative concentrations of the carriers, so that an excess of one type of carrier greatly increases the probability that trions will form. The additional carrier reduces the binding energy of the trion compared to the neutral exciton, resulting in additional peaks being observed in the PL spectrum. This binding energy is of the order of tens of meV. Thus, contributions from both neutral and charged excitons can be observed in overlapping peaks even at room temperature. In Figure 11, we can observe in a WSe_2 monolayer the neutral exciton peak at 1.649 eV and a tail-like behaviour at lower energies. This is due to the contribution of the trion, peaking at around 1.618 eV.

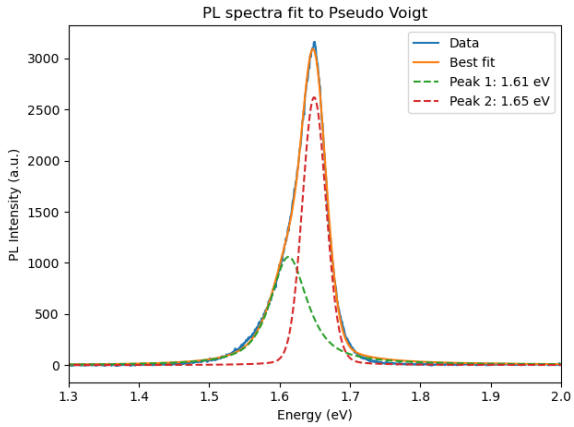

Figure 11: A WSe_2 monolayer PL spectra decomposed into two Pseudo-Voigt curves, showing a neutral exciton at 1.65 eV and a trion at 1.62 eV.

A biexciton is a system consisting of two neutral excitons. The binding energy is usually reduced in respect of that of the trion. Biexcitons are harder to measure at ambient temperature due to this reduced binding energy, in many cases being smaller than 30 meV [24], though, due to the high dependence on the surrounding environment that affects monolayers, binding energies for excitonic complexes can vary greatly. An important detail must be remarked: as dielectric screening is small, biexcitons can form when a pair of excitons interact from the same K valley (AA pair), or when one exciton is from the K valley and another from the K' valley (AA' pair).

In summary, although there are other excitonic complexes that can be present in TMD monolayers (charged biexcitons) we need to focus on the 3 main observable types of excitons: neutral excitons, trions and biexcitons. In Figure 12 we can see a scheme of the previously discussed excitonic complexes.

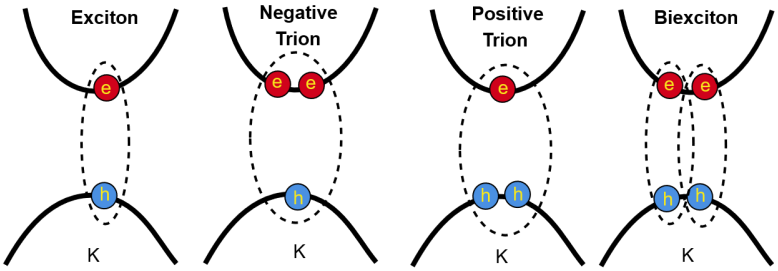

Figure 12: Illustration of the exciton, trion, and biexciton systems constructed from the electrons (e) on the conduction band and holes (h) in the valence band. K high symmetry point of the Brillouin zone of the TMD.

2.3 Van der Waals Heterostructures

As previously stated, a single layer of TMD material consists of a 3 atom thick of a trigonal prismatic lattice bonded by covalent bonds. These dangling-bond-free atomic sheets contrast with typical nanostructures, which have dangling bonds and surface traps. In addition, no covalent bonds at the surface lead to interactions between neighbouring layers characterised by van der Waals forces.

These weak van der Waals interactions allow very different materials to be stacked without concern for lattice constant mismatch. This allows considerable freedom in integrating layers of different materials to create diverse van der Waals heterostructures with properties that were not previously possible.[25].

In semiconductor heterostructures, band alignment refers to how the energy bands of two different materials align when they are brought together. There are three main types: Type I (straddling gap), Type II (staggered gap) and Type III (broken gap). In type I alignment, the conduction and valence bands of one material lie within the band gap of the other, trapping electrons and holes in the same region, which is beneficial for devices such as LEDs and lasers that rely on radiative recombination. Type II alignment features a staggered configuration where the conduction band minima and valence band maxima of the first material must be of a higher energy than those the second material, creating a new effective band gap from the conduction band of the second material to the valence band of the first material, resulting in a spatial separation of electrons and holes. This separation is beneficial for applications such as solar cells and photodetectors where efficient carrier separation is desired. Finally, type III alignment, or broken gap, occurs when the conduction band of one material is below the valence band of the other, creating unique electronic properties that can be exploited in advanced optoelectronic devices such as TFET [26](tunnel field-effect transistor) and for investigating new phenomena in semiconductor physics.

One can relate this freedom of integrating layered materials to a $LEGO^R$ game (Figure 13), whereby stacking different layers we can create new devices. Different 2D materials are stacked to form lateral and vertical heterostructures with hybrid bulk and interface properties. Layers are being stacked at controlled angles of twist, to reveal new physics and layer coupling [27]. There is a myriad of possible applications combining different TMDs, contacts and graphene as shown in Figure 14. These applications work with different possible combinations of materials and changes like twist angle or type of stacking to fulfill many different niches. For example, two side by side TMD layers in a p-n junction can work as photovoltaic cells in Figure 14.L [28], whereas top stacked layers work as tunable LEDS or as Field Effect Transistors with high on-off ratios in Figure 14.E [29].There are also three growing fields of physics thanks mainly to TMD heterostructures [30]: excitonics, twistronics and spintronics.

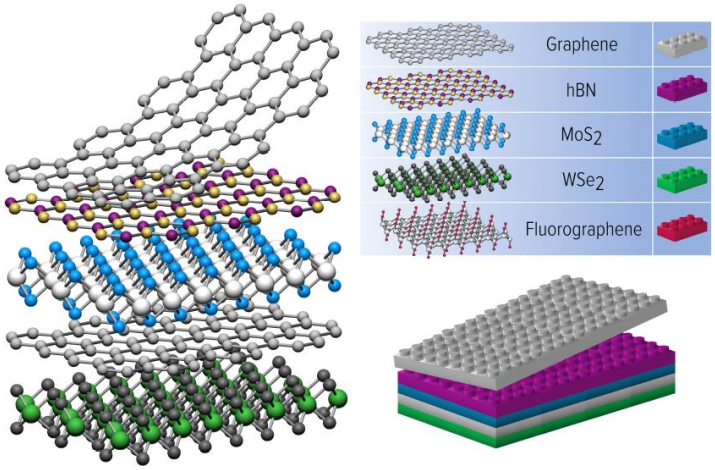

Figure 13: Lego-like stacking behaviour in heterostructures. [31]

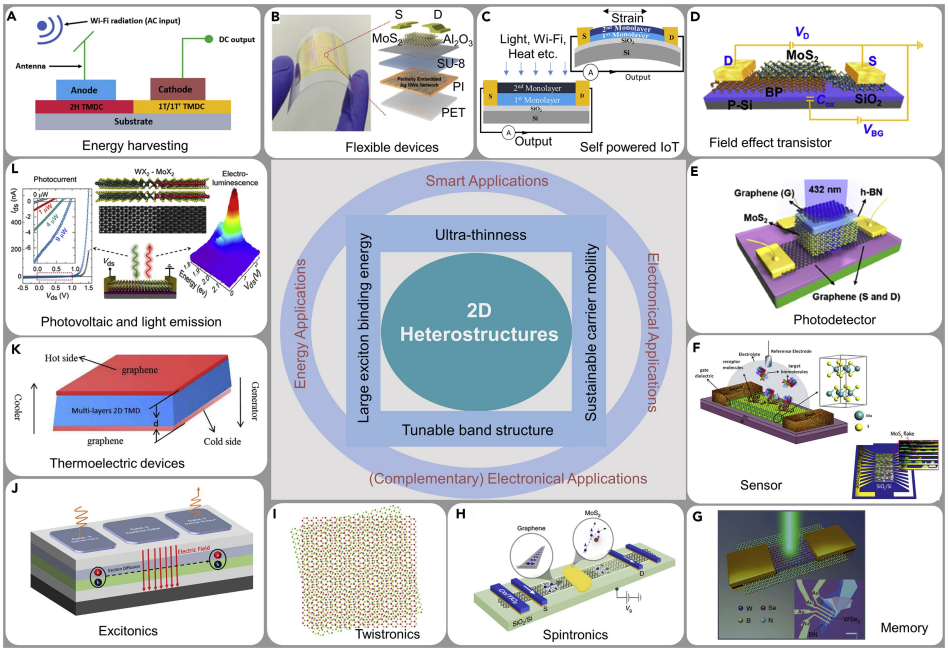

Figure 14: Potential applications of 2D materials based heterostructures[30]

2.3.1 Interlayer excitons

In single layer TMDs, excitons exist entirely in the plane of the layer. If two of these layers are stacked on top of each other, we can now have bound states that exist in the vertical direction across two layers. This type of excitons can then be distinguished as intralayer excitons, where electron and hole are localised in a single layer, or interlayer excitons (IEs), where electron and hole are located in separate layers (Figure 15).

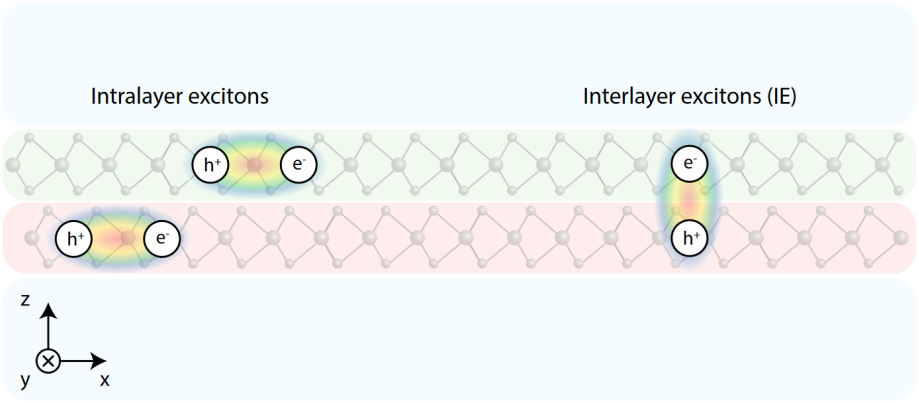

Figure 15: Schematic of the intralayer and interlayer excitons. The red and green layers represent WS2 and WSe2 layers while the blue encapsulating layers represent hBN [20]

As there are many different semiconducting TMDs to choose from when fabricating heterostructures, we have to choose the layers to stack on top of each other. To encourage formation of interlayer excitons [20], the heterostructure needs to have a staggered (Type II) band alignment. In Figure 16, we can see the different band alignments of TMDs. As most TMDs show Type II band alignment, we can choose the combination of monolayers that emits in a given optical spectrum or shows interesting properties. As an example, we fabricate heterostructures of stacked layers of WSe_2 and WS_2, this means that we will create an effective band gap for our interlayer exciton from the conduction band of WS_2 to the valence band of WSe_2, which should amount to an interlayer emission of around 1.3 eV, much lower than any of the intralayer emissions (1.65 eV and 2.1 eV, respectively). Therefore, another way to detect the interlayer exciton states is to find emission at lower energy than the expected direct band gap transitions in each single layer. This band gap can range from near infrared to infrared wavelengths, depending on the choice of materials.

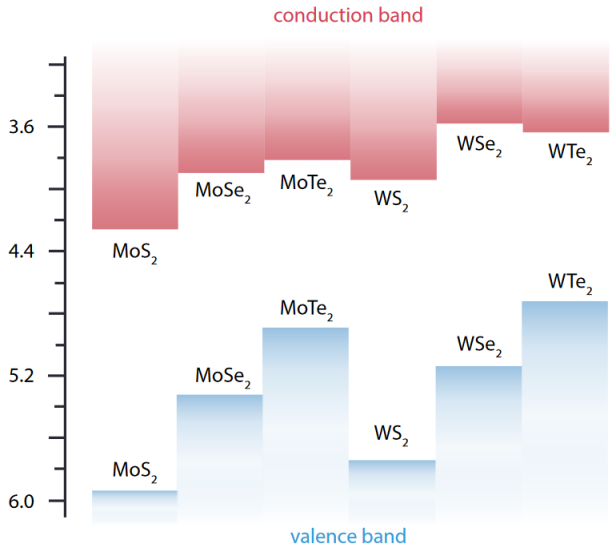

Figure 16: Monolayer band alignments of various semiconducting TMDs. Adapted from [32]

Since the electrons and holes are spatially separated, recombination becomes much harder, significantly increasing interlayer exciton lifetime. Measured lifetimes can range from 1 to 500 ns, 3 to 5 orders of magnitude longer than those of intralayer excitons [20]. In addition, depending on the twist angle between the layers, these lifetimes can vary one order of magnitude [33]. The interlayer exciton exhibits greater dielectric screening because the field lines are mostly within the TMDs, however, binding energies are still very high, within 50 meV to 360 meV [34], allowing them to be observed at ambient temperature.

Due to the inevitable lattice mismatch and/or twist angle between the two layers, the electron and hole bands from the two layers are displaced from each other. The radiative recombination of interlayer excitons with zero kinetic energy is forbidden by momentum conservation [34]. Thus, interlayer excitons are indirect in the k space, requiring the interaction with a phonon to produce interlayer recombination (Figure 17).

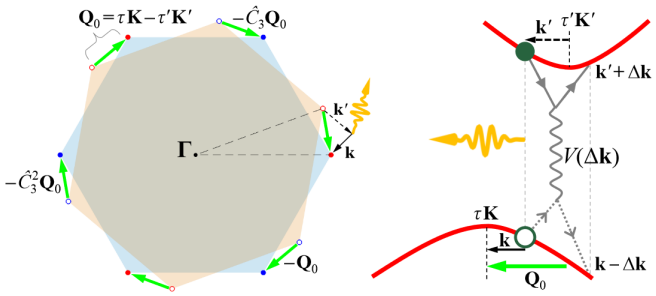

Figure 17: Heterostructes create a momentum mismatch between K valleys. Interlayer Coulomb recombination between the electron and hole conserves momentum in a twisted heterostructure. Adapted from [35]

2.3.2 Moiré patterns

The discussed momentum mismatch and effect of twist angles in heterostructures creates new fabrication problems and effects, creating new physics, twistronics. For example, two layers of monolayer graphene placed on top of each other and rotationally misaligned at a specific "magic-angle" drastically changes the behavior such that superconductivity and other highly correlated physics can emerge [36]. Changing the twist angle between layers changes the interlayer interactions, offering new ways to control them. The physical phenomena associated with these structures can be understood in terms of an interference pattern created by the small misalignment between the grids in each layer. These interference patterns are called moiré patterns [37].

A moiré pattern is a large-scale, periodic interference pattern between the crystal lattice of the two layers. There are three scenarios that give rise to a moiré pattern :

- a relative misorientation of two periodic lattices or twist angle θ
- a relative lattice mismatch $\delta = \frac{a_1 - a_2}{a_1}$ between the lattice constants a_1 and a_2
- a combination of both a misorientation and a lattice mismatch

As heterostructures both present a lattice mismatch and a twist angle, we will always have a combination of both of these effects, the wavelength of the moiré pattern is given in Equation 8. To explain clearly what affects a moiré pattern in heterostructures, first we need

to explain the first two scenarios, then combine them to get to a real heterostructure's moiré pattern.

$$L \approx \frac{a_1}{\sqrt{\delta^2 + \theta^2}} \tag{8}$$

First, we will study the effect of twist angle. Figure 18 shows a moiré pattern formed in a twisted homobilayer system. The hexagonal moiré pattern that forms can easily be seen, as outlined by the black hexagon. If the twist angle increases, the moiré wavelength will decrease. A new periodicity in reciprocal space arises from the periodic structure of the moiré pattern. For a twisted homobilayer with reciprocal lattice vectors b_1 and b_2 of the top and bottom monolayers, the lattice vector for the moiré reciprocal lattice is $g = b_2 - b_1$ [38] and giving rise to moiré high symmetry points shown in Figure 19. Since the moiré supercell is bigger than the unit cell of the crystal lattice in real space, the moiré supercell is smaller than the unit cell of the crystal lattice in reciprocal space. At high symmetry points the local lattice of the twisted bilayer approximates the structure of a nonrotated bilayer except for a displacement of the layers.

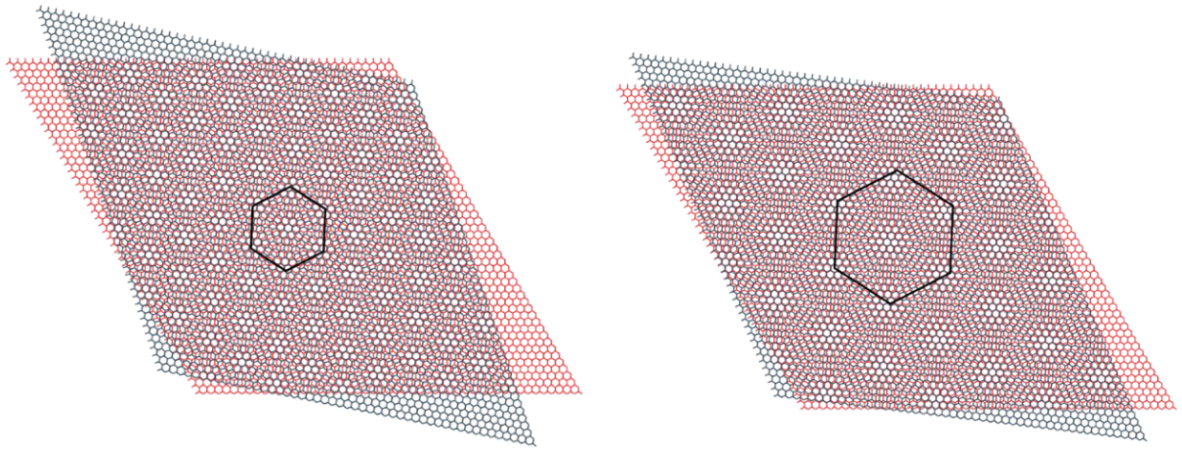

(a) *(b)*

Figure 18: In a) and b) the lattice constants are the same, but there is a rotational misalignment θ The moiré pattern is smaller (larger) for a larger (smaller) twist angle. (a) $\delta = 0, \theta$ large, (b) $\delta = 0, \theta$ small Adapted from [37]

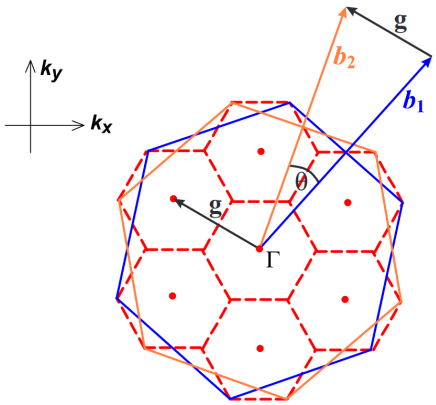

Figure 19: Reciprocal space of a TMD homobilayer with twist angle $\theta = 22°$. Reciprocal lattice vectors b_1, b_2 and the Brillouin zones (blue, orange lines) of the monolayers and the reciprocal lattice vector g of the moiré unit cell are depicted. The Wigner-Seitz cells of the moiré superlattice in reciprocal space (red dashed lines) and points equivalent to Γ (red dots) are marked [38]

Now we will study the effect of the lattice mismatch: Figure 20 shows the formation of a moiré pattern in a rotationally aligned $\theta = 0$ heterostructure where the top lattice has a slightly larger lattice constant than the bottom $\delta > 0$. It can be seen that even though there is a lattice mismatch, there is still a periodicity arising from the moiré pattern, the same effect as in the homobilayer. It naturally follows that for larger lattice mismatches the moiré pattern will be smaller. Aditionally, we can see that there are still high symmetry points arising from this pattern, where the heterostructure approximates the structure of a homobilayer in some points.

Combining both effects we can see that although understandably moiré pattern wavelengths will be much smaller when taking into account both $\theta, \delta \neq 0$, for lower twist angles, observable moiré patterns will still form. As many different notations in literature are used for the high symmetry points, we will denote the places where the lattices overlap as AA^Z_θ stacking and places where the atom of one layer sits above the center of the hexagon of the other layer as AB^Z_θ stacking (Figure 21). Meanwhile, as we are working with hexagonal lattices, 0^o and 60^o are different symmetry points. For Z, the top atom in the hollow center of the hexagon, h denotes a hollow site, X a chalcogen atom and M a metal atom. Two main effects can result from this variation in local stacking arrangements:

- The interaction energies will be different for the different stacking regimes.
- As in the case of twisted bilayer graphene, where AB stacking is preferred over AA stacking, one stacking arrangement may be preferred over the other.

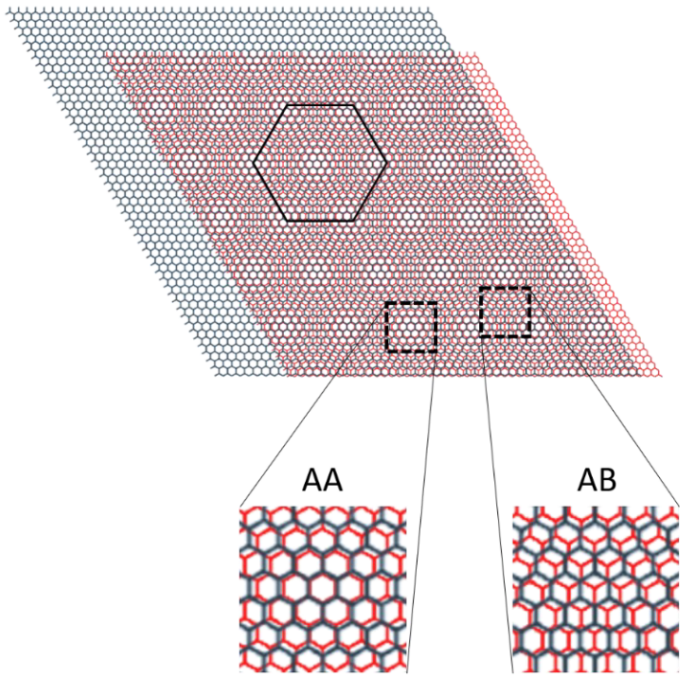

Figure 20: Layers are rotationally aligned $\theta = 0$, but the blue lattice has a slightly larger lattice constant than the red lattice $\delta > 0$. Adapted from [37]

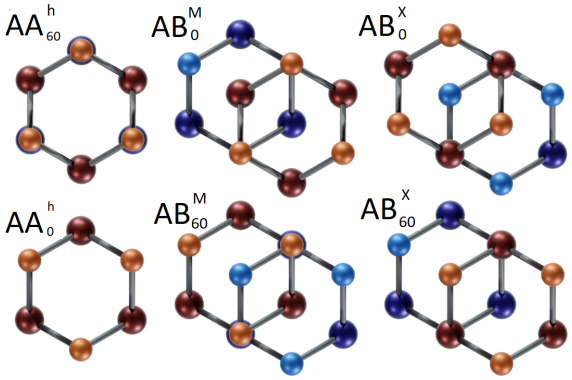

Figure 21: Top view of the high symmetry stacking configurations in TMD heterostructures. The top layer is depicted in red (metal atoms) and orange (chalcogen atoms). The bottom layer is depicted in blue (metal atoms) and turquoise (chalcogen atoms) Adapted from [37] for this master's thesis nomenclature.

As the interaction energies can vary greatly, electronic structure can also vary significantly with the moiré periodicity, changing bandgap in heterostructures or recombination probabilities. In heterostructures of WSe_2/WS_2, the lattice constant mismatch is of $\approx 4\%$, quite large for heterostructures, giving us an upper range of moiré periodicity using Equation 8 of $\approx 8nm$. From experimental results given by heterostructures with different twist angles measured at 4K in [39], it seems that there are 3 different groups: A first group with heterostructures of a

really small twist angle (< 1), where the absorption spectra shows three prominent absortion peaks in the WSe_2 energy range from the moiré exciton states giving rise to local energy minima. For heterostructures of higher twist angle (> 3), spectra is similar to the response of weakly-coupled bilayers, behaving like isolated monolayers. For twist angles, between 1 and 3 degrees, spectra show intermediate behaviours, with higher energy absorption peaks barely observable leaving only one exciton peak. For AB stacking, the behaviour is similar.

As one type of stacking is usually preferred, the layers in that region of the moiré pattern will tend to relax such that the lattices become rotationally aligned and lattice matched in order to reduce the energy of the system. Due to this, elsewhere in the moiré pattern these layers may misalign and mismatch giving rise to other stacking arrangements (Figure 22). Thus, interaction energy around the space will determine the behaviour of the moiré pattern, the different interlayer interaction energies can also give rise to corrugation of the layers since interlayer separations will be different across the moiré pattern. For a large twist angle, relaxation of the atomic lattices will not occur because the layers energetically prefer to behave like isolated monolayers as moiré wavelengths are too small giving rise to many domain walls. Normal moiré wavelength range from 10nm to 100nm.

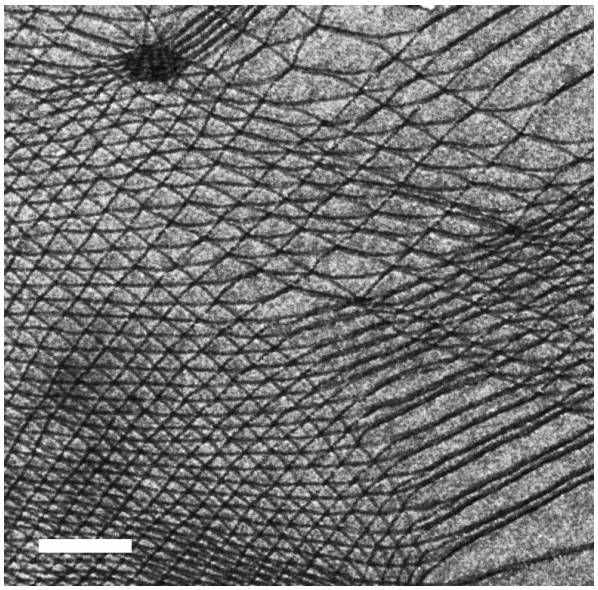

Figure 22: Figure 7: Experimental Dark Field Image of a $MoSe_2/WSe_2$ heterostructure exhibiting a variety of moiré patterns due to a non-uniform strain field. [40]

Thus, as seen in Figure 22, when we measure a real heterostrucure we expect to find different moiré patterns depending on the strain between the heterostructures due to the existence of contaminants or broken parts of the heterostrucure. Additionally, the heterostructure may suffer from atomic reconstruction minimizing the energy configurations in some points in space, thus achieving different moiré patterns even in the absence of applied external strain or environmental effects.

3 Sample Fabrication

In this section, we will present all of the sample fabrication methods that were used in this work. We will also provide an overview of best practices for the fabrication of high quality heterostructures. After the introduction of the techniques, the fabrication steps of one of the heterostructures under investigation in this work will be described in detail. Finally, we will explain the thermal annealing process to reduce interlayer spacing and impurities.

3.1 Mechanical Exfoliation

Many different processes have been developed for the manufacture of two-dimensional materials and monolayers [41] [42]. The most common method of fabricating good quality monolayers for heterostructures is mechanical micro exfoliation, followed by chemical vapour deposition.

Mechanical exfoliation is the least technological and cheapest method available for preparing 2D TMDs from bulk materials, ever since the discovery of graphene. However, it boasts high optical quality compared to its alternatives. The process consists of placing a massive crystal of the material to be exfoliated on a strip of adhesive tape (Blue Nitto Tape) on which, by folding this strip, the crystal is divided into two thinner parts. With successive folds we obtain a thinner and thinner material, i.e. we exfoliate it [43].

The best approach is not to fold it too many times, an optimal value is 5-6 folds, so that the original crystal is spread all over the Blue Tape, in the form of small shiny dots concentrated in clusters that are visible to the naked eye as in Figure 23.

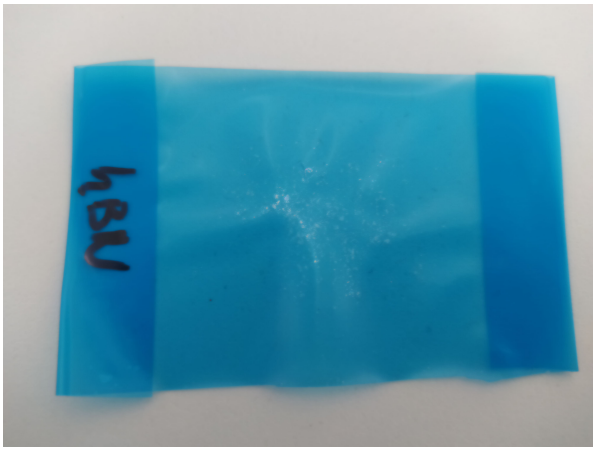

Figure 23: Blue Nitto Tape with 2D hBN crystals exfoliated on top.

A sheet of flexible, optically transparent polymer (PDMS) taped to a glass sample holder is used. This PDMS has a small protective film that is removed just before placing it in an ozone generator (Figure 24) to clean the sample for 15 minutes in such a way that we minimize the organic residues that we may transfer and activate the dangling bonds present in PDMS for an increase in adhesion force [44], thus facilitating exfoliation of bigger monolayers. This is particularly important in our case, because for heterostructure fabrication it is particularly important to ensure a residue-free surface with a large surface area in each of our monolayers.

Figure 24: Ozone generating system using UV lamp

Once the PDMS has been prepared, we will gently place the blue tape on top of the PDMS so that small bubbles appear in the contact area, allow these bubbles to slowly dissipate ensuring contact, and then gently remove the blue tape perpendicularly from the PDMS. This will transfer some 2D crystals from the blue tape to the PDMS (Figure 25). These crystals should be manually detected with a light microscope, scanning the entire PDMS for possible monolayers or other crystals of interest.

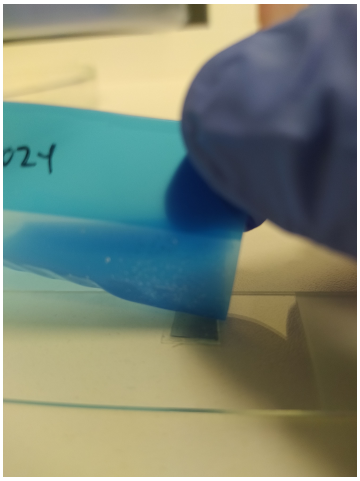

Figure 25: 2D flakes transference from Blue Tape to PDMS supported in glass sample holder

When looking for monolayers, it is important to remember that that their thinness renders them almost transparent, so one should look for them at least at 10x magnification to be able to distinguish them (Figure 26). Once they have been found, a simple way to assist in their identification from a bilayer to a monolayer is to see whether or not the monolayer, which is almost transparent in transmission, can be seen when the microscope is switched to the reflection mode. If a shadow is hardly visible, it is most likely a monolayer (Figure 26), although verification of the thickness must be made by other methods such as photoluminescence or atomic force microscopy.

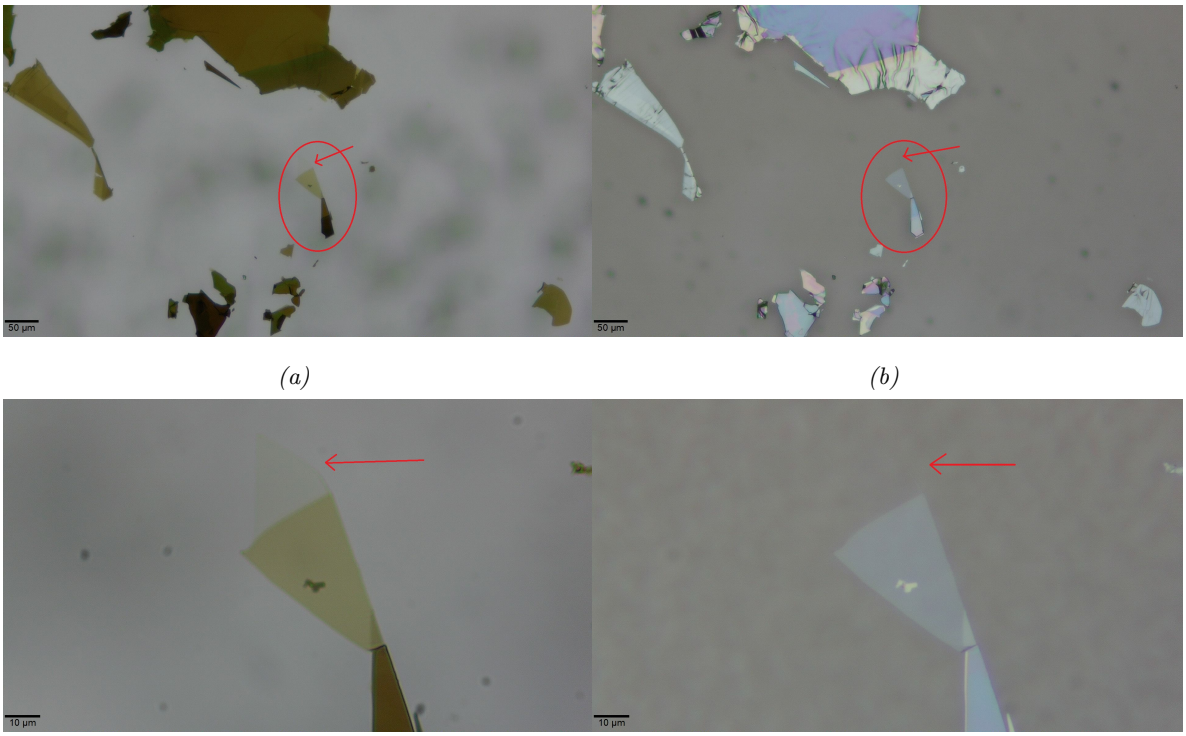

(a) *(b)*

(c) *(d)*

Figure 26: WS_2 Monolayer exfoliated on PDMS as seen on an optical microscope. Flake of interest marked and arrow pointing at the monolayer. (a) 10x Transmission, (b) 10x Reflection, (c) 50x Transmission, (d) 50x Reflection

The properties and appearances of different materials will make it easier or more challenging to distinguish monolayers of these materials under a microscope. WSe_2 will exhibit reddish hues (Figure 27.a), due to its relatively less energetic band gap. Conversely, hBN will appear transparent when the thickness is less than about 15nm. At this magnification, the hBN monolayer is indistinguishable from the PDMS. Therefore, it is extremely challenging to identify by optical microscopy without the help of a portable spectrometer (Figure 27.c). However, for the purposes of this work, the objective is to utilize hBN as a protective and dielectric layer, which requires only a thin layer, not a monolayer.

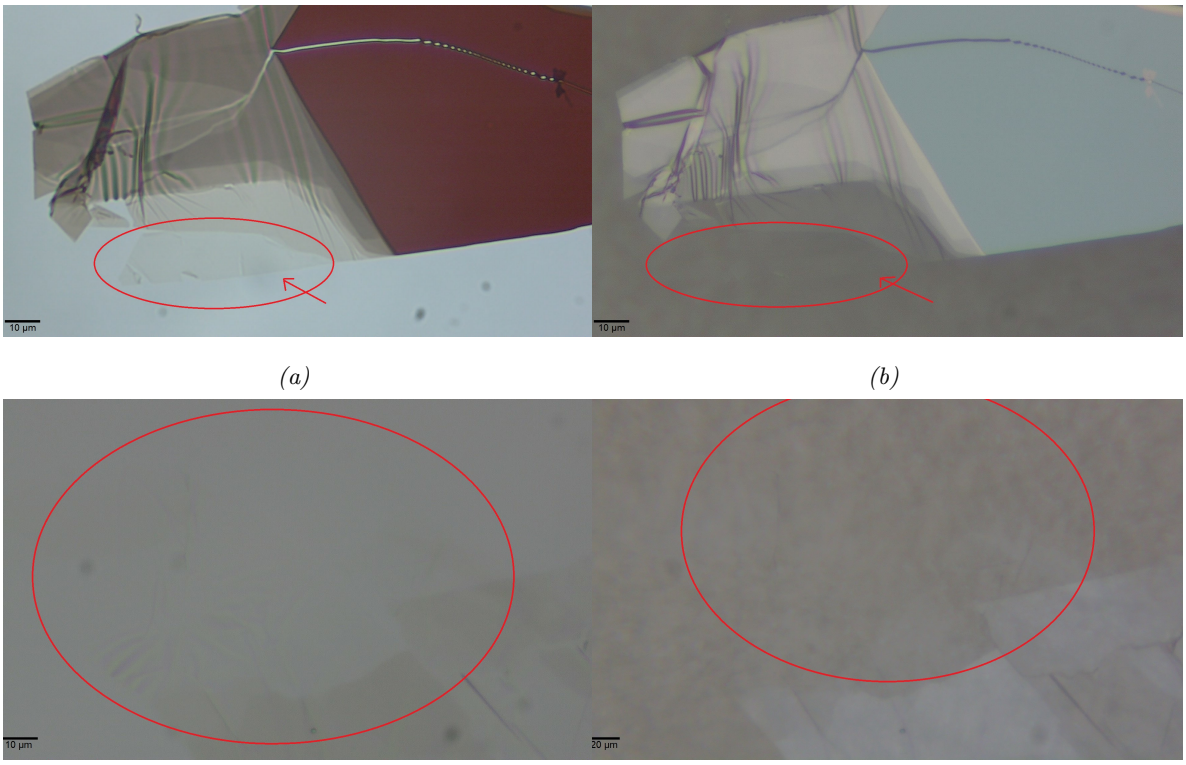

(a) *(b)*

(c) *(d)*

Figure 27: (a) and (b) WSe_2 Monolayer exfoliated on PDMS as seen on an optical microscope. (c) and (d) hBN thin flake exfoliated on PDMS. (a,c) 50x Transmission, (b,d) 50x Reflection

It is important to note that these exfoliated monolayers are in the range of $20 - 50\mu m$, denoting a small size compared to other research groups and chemical fabrication processes. This is most probably due to two main factors: the humid climate of Asturias and other environmental factors and the inexperience of the author, with more experienced members of the research group able to exfoliate monolayers of up to $100 - 200\mu m$.

3.2 Dry Transfer

In the process of dry transfer, a moving platform system is employed in order to bring the monolayer obtained on PDMS in proximity to a silicon substrate coated with a silicon oxide thin film bearing gold markers. This facilitates subsequent steps by rendering the monolayer easier to locate. Once the monolayer has been brought into sufficient proximity, van der Waals forces will adhere it to the silicon substrate.

The objective of this section is to facilitate the contact between the PDMS, attached to a sample holder that is pressed against a mobile platform, and the substrate, fixed with a vacuum pump to another platform that can be moved vertically. Figure 28 illustrates the transfer machine. Once in contact, the surfaces will experience the combined action of elastic and Van der Waals forces. As the sample approaches the PDMS, micrometer screws are used to move the platform and substrate in all three axes, as well as rotating the substrate up to 90° along the plane. Abrupt contact between sample and substrate is very likely to damage, break or bend the sample in a way that would destroy both the sample and any 2D crystals on the substrate at that point. thus, it is of vital importance to exercise caution when approaching the PDMS with the sample.

In order to avoid this type of situation, contact should be made very slowly and once contact has been made where air bubbles are present, complete contact should be achieved by the elimination of these bubbles. The contact should then be broken slowly, controlling the speed at which the surfaces separate. Ideally, the monolayer should remain intact on the substrate.

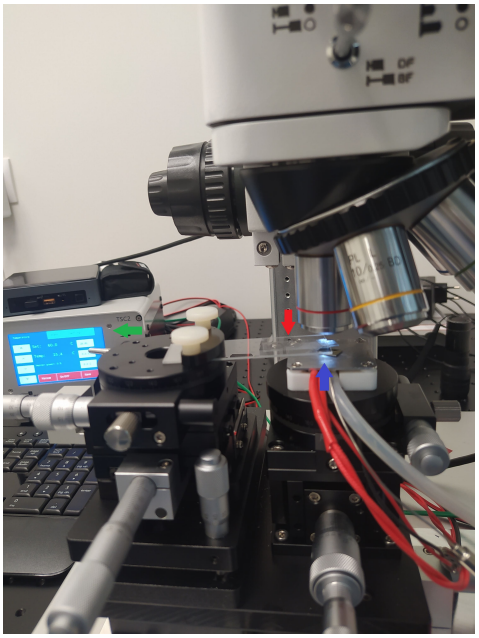

Figure 28: Dry transfer System. In red the mobile platform with the PDMS. Marked in blue is the substrate platform. Marked in green is the unit for vacuum and temperature control

It may be necessary to apply pressure with tweezers to improve contact, always touching away from the 2D crystals being transferred to avoid breaking them. It is also advisable to perform the transfer at temperatures of 60-80ºC using a thermoresistor. This weakens the adhesion of the PDMS, making the transfer easier and less likely to fail. [45].

It is important to note that after the fabrication of the samples used in this work, it was noted by the group that although a transfer at higher temperatures does aid the transference, thermal gradients might wrinkle or break the monolayer when transferring. Although monolayers break easily, some of the wrinkles and breakages in the studied monolayers can be attributed to heating during transference.

3.3 Heterostructure Fabrication

We have fabricated 5 different heterostructures in this work. All of them were composed of hBN/WS_2/WSe_2/hBN layers from top to bottom. All of them adhered over a substrate of Si with a $300nm$ layer of SiO_2 to increase contrast and adhesion. The WS_2 and WSe_2 bulk materials were obtained from HQ Graphene, a commercial supplier of high quality crystals for exfoliation. hBN for heterostructures 1-3 was also obtained from HQ Graphene's crystals. For heterostructures 4-5, there was a collaboration with Japan's Research Center for Electronic and Optical Materials researchers K. Watanabe and T. Taniguchi who supplied high quality hBN crystals prized for their low amount of defects and extremely high purity [36].

Now, we present in Figure 29 all of the hBN flakes and monolayers used in one of the heterostructures (Sample 4) and how by transferring each layer on top in Figure 30 we are

able to fabricate a heterostructure. We can clearly see the contrast between the monolayers deposited on PDMS and on hBN and SiO_2. This is mainly due to an interference pattern arising from the light in the microscope. We can also see that we will have a region where both monolayers overlap and this is where the heterostructure is defined.

As it is not a trivial task to perfectly transfer one monolayer onto another, we can also see small wrinkles in the heterostructure and even some slightly broken spots. This means that there is likely to be uneven strain in the heterostructure. There can also be some monolayers of water and contaminants between the monolayers, increasing the interlayer distance. This distance might be too great for interlayer excitons to appear in some heterostructures.

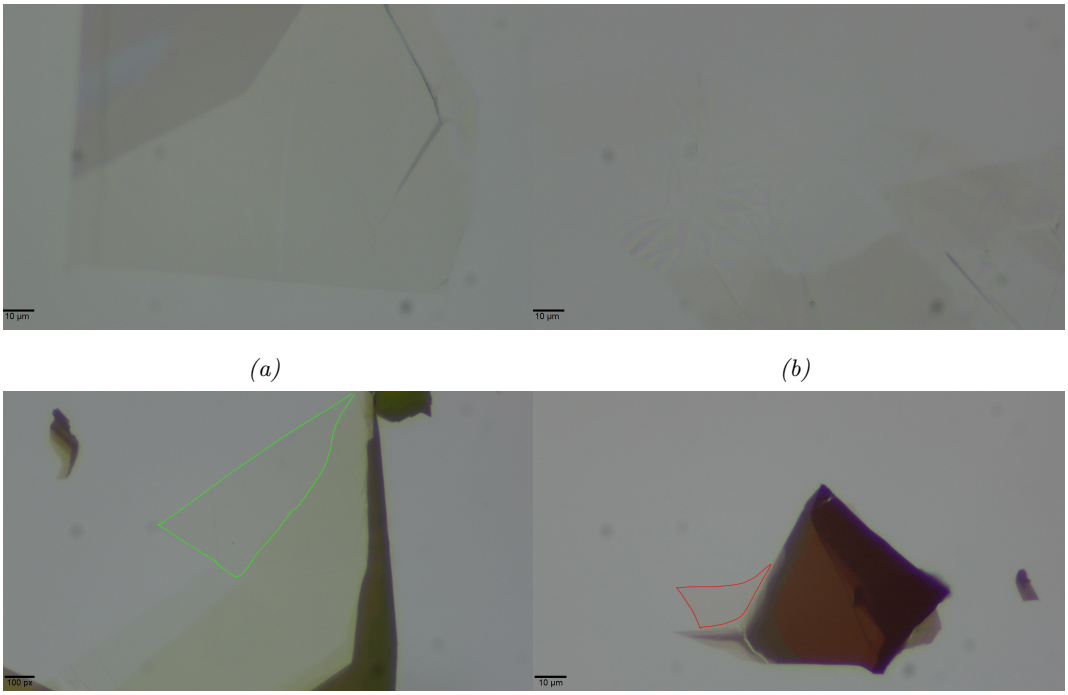

(a) *(b)*

(c) *(d)*

Figure 29: Heterostructure 4 hBN,WSe_2 and WS_2 monolayers and flakes in PDMS before transference. (a) 50x Bottom hBN, (b) 50x Top hBN, (c) 50x WS_2, (d) 50x WSe_2. WS_2 monolayer marked in green, WSe_2 monolayer marked in red.

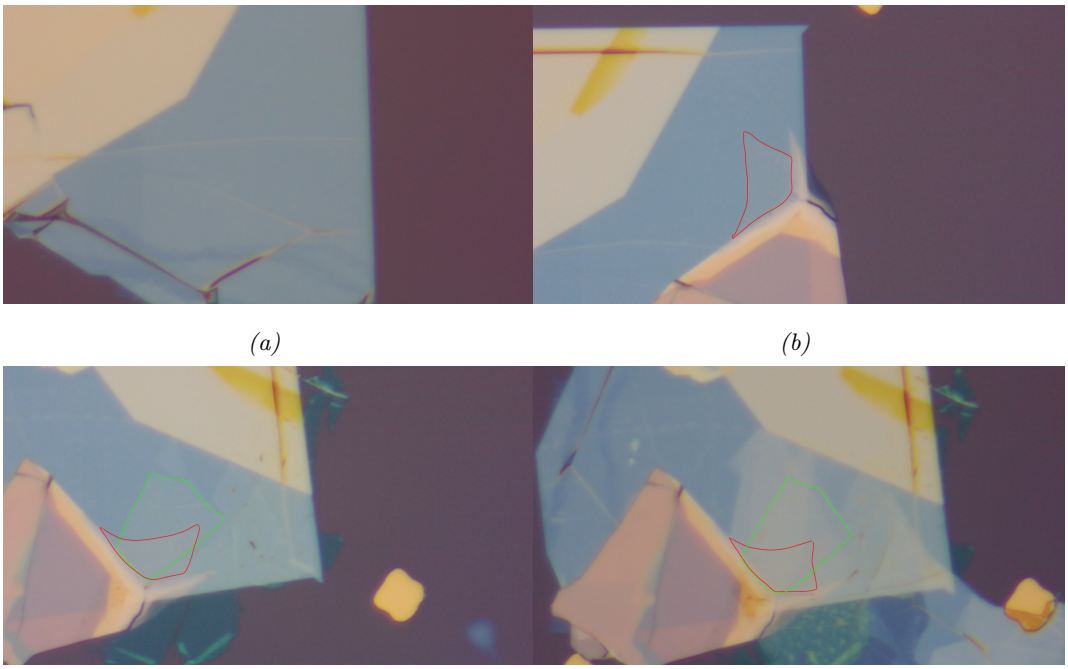

Figure 30: Heterostructure 4 transference process onto SiO_2 substrate. (a) First hBN, (b) hBN/WSe_2 (c)hBN/WSe_2/WS_2 (d) hBN/WSe_2/WS_2/hBN. WS_2 monolayer marked in green, WSe_2 monolayer marked in red.

3.4 Thermal Annealing

To measure the behaviour of the heterostructure, we will use a convection oven to anneal the sample for a certain amount of time. The heat will evaporate any water monolayers between the layers and the air bubbles. This will bring the monolayers closer together, allowing interlayer excitons to form. Additionally, this annealing can also help relax the heterostructure into positions minimizing energy, so that according to Section 2.3.2 might break the heterostructure into different moiré patterns, each of them minimizing energy in their local space.

Annealing is performed at 200ºC [46], [47], [48]. where we ensure good relaxation and cleaning of residues between the heterostructure with low risk of wrinkling or breakage due to thermal expansion. Although it can be noted that according to some research groups this process of annealing might actually be detrimental in ensuring higher quality heterostructures, in this work, as a previous study in heterostructures showed promising results from annealing, the annealing was kept in the process. Additionally, oxidation of monolayers is negligible at 200 °C [49], while there has not been found a paper where defects in hBN were created at less than 500º [50]

4 Optical Characterization

4.1 Micro-PL System

Now we will show how we will characterize the samples using the technique of PhotoLuminiscence, the basics of which were explained in Section 2.1.3. Thus, for the basic design of our characterization setup, we will need a laser, a set of mirrors and optical elements that can direct the laser beam to the sample, and then take the emission of the sample to a detector, and a filter to protect and avoid saturation of the spectrometer from the laser beam.

As we want to study smaller systems (in the micro-scale), we need a way to focus the laser beam and collect from a small spot in our sample. For that objective, an ideal element is a high quality optical microscope objective with 100x magnification. When we add an objective to a PL system it is called a Micro-PL System.

As we want to study emissions in the 1.3 eV (950 nm)- 2.0 eV (620 nm) range, it is advisable to choose lasers that emit in 532 nm (2.3 eV) or 505 nm (2.45 eV) range. As the difference in bandgap will allow for a green filter (532 nm) to eliminate almost all of the intensity of the laser while behaving almost transparently to the sample emission.

Finally, the next element in the Micro-PL system is the detector, in this case an ANDOR Kymera 328i spectrometer, with a 1200 lines/mm difraction grating, allowing us a resolution of 0.1 nm, coupled with a Newton CCD, a silicon based charge coupled device that allows for both high luminosity measurements and detections of up to a single photon thanks to its high quantum efficiency. With this setup we are able to separate the different wavelengths of the emitted light and measured their intensity (in counts) for a correct study of the heterostructure's emission.

4.1.1 Setup

The optical setup used in this work is complex and spans different z-levels and optical tables. To understand the setup, Figure 31 has a scheme of the full system using ray optics simulation. The core process is as follows: A laser beam (green) is passed trough a power regulator to control the intensity of the incident light. Then, the beam is incident on a dichroic mirror, which acts as a mirror for light of the laser's wavelength, while being transparent for light with bigger wavelengths. The laser beam is thus reflected into a steering mirror, a mirror that using an electromagnet is able to change its position and incident angle with nanometric precision. This steering mirror coupled with a 4f system (explained in detail in Section 4.1.2) allows to focus the laser beam and subsequent recollection in different places in the XY plane of the sample. Enabling the measurement of different points of the sample by only changing the angle of the steering mirror.

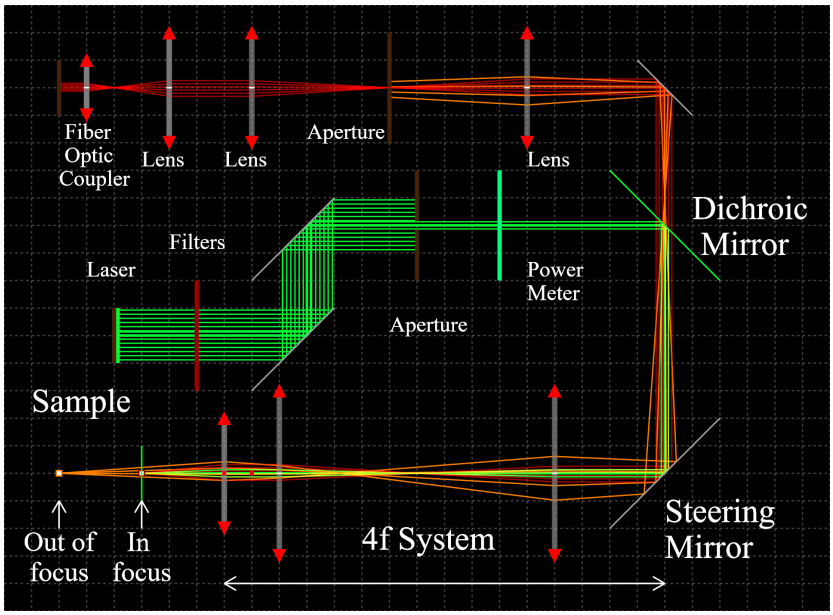

Figure 31: Scheme of the Optical Setup used in measurements at room temperature using Ray Optics Simulations

After passing through the 4f system, the laser beam is then focused on the Z plane using a lens coupled with stepper motors, allowing the focus of the beam along different points along the depth of the sample. Once incident on the sample, it will emit both light from the focused (in depth) part of the sample (red) and the out of focus part (orange) although with lower intensity. Both of these emissions and the reflected laser beam pass through the 4f system and onto the dichroic mirror, which is transparent to the sample emission wavelength. After that, it is then passed through a confocal system (explained in detail in Section 4.1.3) which allow us to remove most of the out of focus light enabling us to only collect light from a small range of depth of the sample.

After the confocal system a fiber optics coupler allows for the collected light to incide on the spectrometer, resulting in a measurement of the intensity of the excitons found in the point of the sample. As the 4f system coupled with the dichroic mirror is able to achieve spatial resolutions much smaller than the wavelength of incident light (10 nm -50 nm) , and the confocal system allow us to collect light of a given depth with around 10nm in resolution; we can create a spatial map of an heterostructure in XY eliminating the contributions from the substrate (Figure 32).

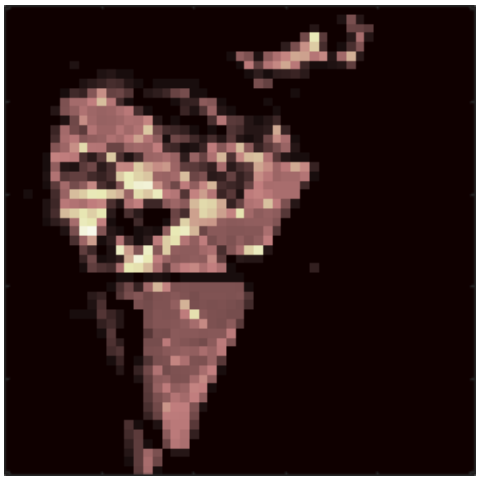

Figure 32: PL Map of heterostructure 4. Represented intensity of the emission peak around 1.65 eV in a $50x50\mu m$ space

Once understood the core process of the Micro-PL system in the schematic, we can understand the real system used in the laboratory (Figure 33): In this setup, we add a few more important elements. First of all, the laser source is brought to the optical table with optical fiber from another optical table. A motorized filter holder blocks the laser's emission when it is not necessary, while a set of two adjustable mirrors between the laser and an aperture (diaphragm) allows us to control the height and angle of the laser beam in order to align it with the optical table plane. A set of two abatible beam splitters between the dichroic mirror and the 4f system allows us to couple a white light source and a camera to the setup, for an easy visualization of the zone of interest.

Finally, in the sample side, an adjustable power meter allows to measure the incident power over the sample and the sample is placed on a motorized holder using stepper motors for rough movement around the sample to find the zone of interest. These stepper motors can also work as a backup for the PL-Map, as they have a resolution of around $0.1\mu m$.

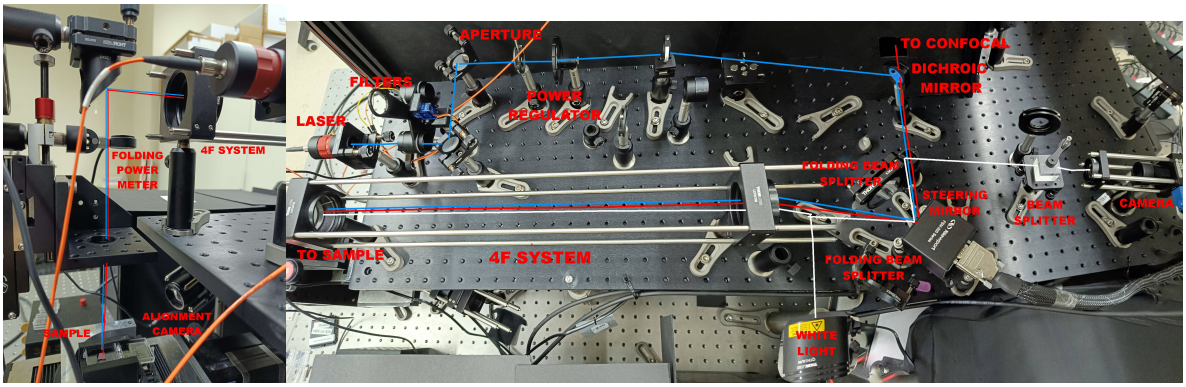

(a) *(b)*

Figure 33: Real Micro-PL system configuration. (b) All of the optical elements without sample and confocal perspectives. (a) Sample Perspective. Composed with Photoshop

To analyze the measured spectra. A custom PL map software made in the research group is used (Figure 34) . This map allows for the selection of the given spectra in Figure 34.1,

the selection of the interval to show in a map in Figure 34.2, the map visualization given a wavelength interval of their intensity values at Figure 34.3 and the visualization of a clicked point in the map an possible integration results in Figure 34.4. This software facilitates the analysis of mappings, allowing for the selection of different measured points in the sample via visual means instead of by spectra number.

To decompose peaks that overlap each other i.e, deconvolute them, custom python scripts were used. Allowing for a selection of intervals where peaks where located, the script is able to fit them to a Gaussian, Lorentzian or Pseudovoigt function. The script uses a least-squared fitting model with a combination of bounded and unbounded parameters to achieve the best fit for the given spectra.

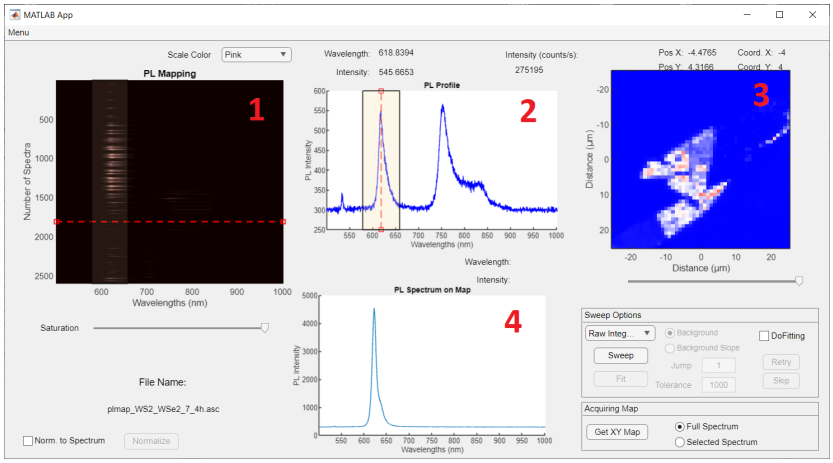

Figure 34: Micro PL map analysis software.

4.1.2 4f System

A four focal system is capable of performing a Fourier transform operation on the light passing through it. The initial lens performs the Fourier transform of the object, and the subsequent lens reconstructs the image. It consists of two lenses with focal lengths of f_1 and f_2, where the distance between the lenses is equal to the sum of their focal lengths. These lenses can be used to generate various kinds of filtering in the fourier plane, magnification and spatial transforms.

When both lenses have the same focal length the image output from the second lens will be exactly the same as the one from the first lens but mirrored (Figure 35.a). When coupled with a steering mirror, the angle of the incident beam will change, an output with that same angle. If another lens of focal length f' is placed after the second lens, the output beam can be focused on a single point(Figure 35.b). With this approach, we can convert angular changes in our steering mirror into spatial changes of out beam. When f_1 and f_2 are large, a small change in angle can produce a great change in space. With the current setup at the laboratory, spatial ranges of up to $100x100\mu m$ can be mapped easily with this system.

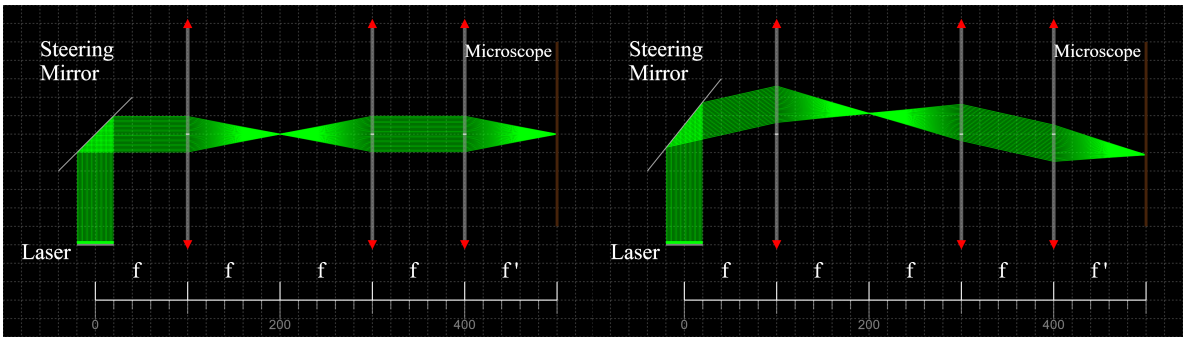

(a) Steering Mirror at 90º angle

(b) Steering Mirror with a small change in angle

Figure 35: 4F system simulation using Ray Optics.

As this system lacks mobile parts, there is a much lesser impact of vibrations and it is much more robust. The only element needed to control for the spatial change is the steering mirror, which can be steered by applying a small Voltage in the electromagnet applying a force on permanent magnets behind the mirror. As there is no need to wait for the stepper motors to accelerate and stop, measurement times can be cut by a factor of 2-4x, while allowing for a greater spatial resolution and being less prone to drift during the measurement. However, this type of setup requires large lenses as the spherical aberration must be minimal.

4.1.3 Confocal System

A confocal system allows focusing on a specific plane within a sample, while rejecting out of focus light from other planes. This system allows to reduce the amount of scattered or out of focus light, resulting in reduced background noise. Additionally, by changing the focus, one can capture optical sections from different depths, allowing for the examination of different layers within the sample.

In our case, we will use a variation of the 4f system shown above to create a confocal system by placing a small aperture in the middle of the two lenses (Figure 36). In this scheme, three point sources at different focal lengths are created, which are collimated in the first focusing lens. The red point source is exactly at the focal point of the focusing lens, while the blue and green points are slightly out of focus.

As the out of focus rays can not collimate, when going through the 4f system the image rays will not converge at exactly the focal length, but farther or closer to the first lens, depending on whether they were closer to the focusing lens or farther, respectively. As there is a small aperture exactly at the 4f system focal length, only those rays from the in focus source can pass through, while the rays from the out of focus sources will collide with the blocker. However, as no aperture can be infinitely small, there will always be a small contribution from the out of focus rays on the output, giving rise to a minimal resolution in the depth given primarily by the aperture size.

Figure 37 shows the Confocal system placed in the lab after the dichroic mirror. It also shows a removable 532 nm filter to remove even more of the laser's contribution to the spectra, ensuring no saturation of the detector. Finally, the light beam is coupled to a fiber optic cable directly connected to the spectrometer.

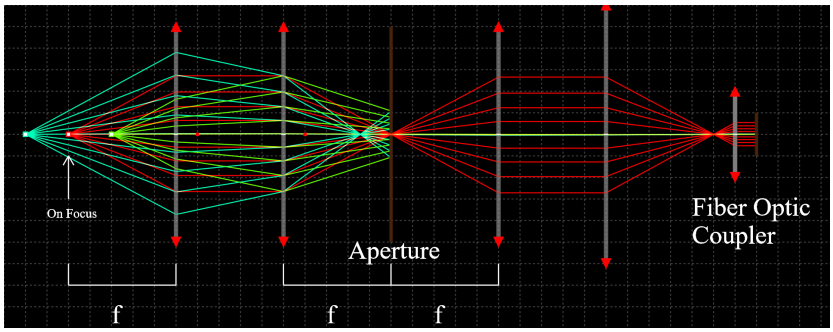

Figure 36: Confocal system simulation using Ray Optics. Red light in focus. Blue and green light out of focus

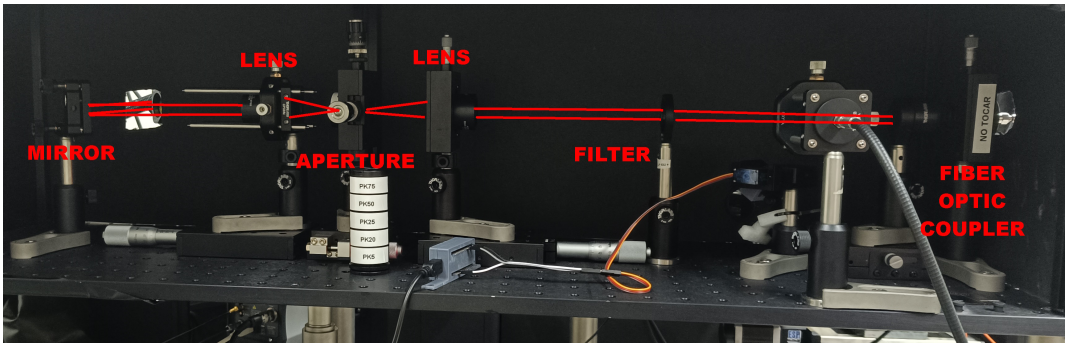

Figure 37: Confocal system in the Laboratory

4.2 Characterization at 4K

For measurements at cryogenic temperatures, an attocube attoDRY800 was used. A closed loop cryostat able to achieve temperatures of 3.8K using liquid Helium. The sample is attached to the cryostat holder using Silver Paint. The cryostat has a clear glass window for viewing and measuring the sample from the outside.

For movement of the sample, the cryostat comes equipped with a set of positioners specially designed for their use at low temperatures. Although their range at ambient temperature is of around $100\mu m$, when used at lower temperatures their spatial range is drastically reduced by half. As these positioners are based on piezoelectric steppers, their resolution is of about 300 nm.

The cryostat was a new addition in the laboratory, and the sample measured in this work was among the first to be characterized at low temperatures. Due to this, optical alignment with the collection fiber optics was not optimal, reducing drastically the number of counts measured in the spectrometer. At the time of measurement the confocal alignment could not be used, as it was lightly misaligned, resulting in a great reduction of measured intensity. Thus, the resolution in the z axis was smaller than in measurements at 300K, although, as the laser was correctly focused on the sample and only the surface is measured, this lower resolution does not hold special importance in our measurements. It is also important to add that as the system was not optimized, PL-Maps were not automated via software, and had to be done manually using the steppers. This imposed a limit on the mapping resolution due to time constraints.

The optical setup is shown in Figure 38.a with a schematic simulation is shown in Figure 38.b. The laser comes from a fiber optic cable and is incident on the sample though the use of a dichroic mirror. Meanwhile, there is a pair of adjustable beam splitters that allow for the coupling of a white light and a camera for positioning of the sample. Finally, the emitted light is filtered from the incident laser light through both the dichroic mirror and a filter. This beam is then coupled to a fiber optic cable directly connected to the spectrometer

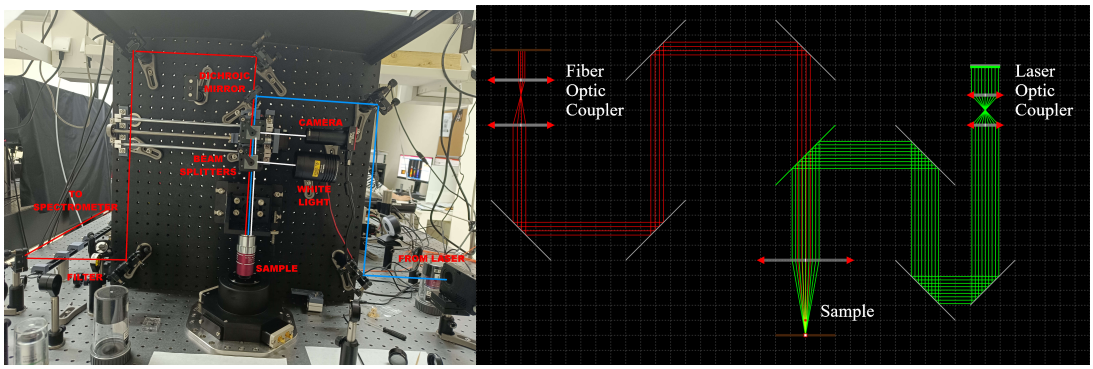

(a) *(b)*

Figure 38: (a) Optical Setup for 4K Measurements. (b) Simulation of 4K Optical Setup

4.2.1 Power Resolved Measurement Setup

When measuring the emission from a sample at 4K, one can find important to be able to compare the emission at different incident laser power intensities. As the laser beam is linearly polarized, it is natural that through the use of a polarizer, given Malus Law $I = I_0 cos^2(\theta)$ we can change the power incident on our sample. Attaching a polarizer to a motorized rotation mount (Figure 39), we can change the angle of the polarizer in respect of the polarization of the laser and create a map for each angle (power) of the spectra of the sample. As no polarizer can block all light when perpendicular to the incident polarization, we measure both minimum (90^o) and maximum (0^o) power levels, and fit using Malus law the power for each of the angle steps taken.

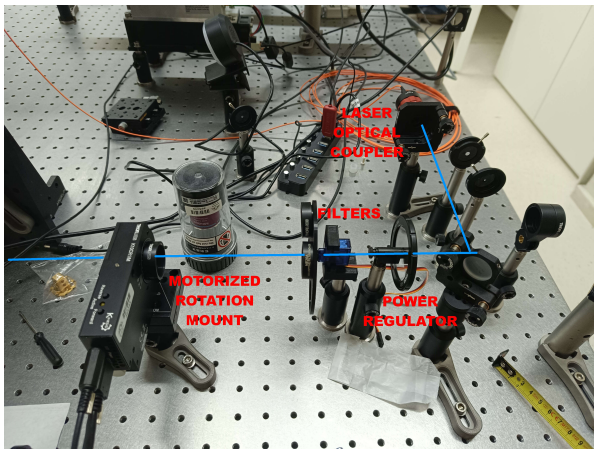

Figure 39: Polarizer Setup before the 4K optical system

5 Results

5.1 Results at 300K

The primary focus of this work was to do a statistical analysis of the optical emissions of heterostructures of $hBN/WSe_2/WS_2/hBN$ and study whether interlayer excitons could be detected on these heterostructures.

For that purpose, two batches of heterostructures were fabricated. Heterostructures 1-3 were fabricated in the first batch. Heterostructures 4-5 were fabricated to test the conclusions taken from the first batch and with higher quality encapsulating hBN. All heterostructures were measured by Micro-PL at room temperature. Maps were made with a size of 50 by 50 μm with a $1\mu m$ step size. Two different lasers were used, with wavelengths of 515 (2.41 eV) and 532 nm (2.33 eV), depending on availability at measurement time. In any case, this variation in laser used should have no effect on heterostructure emission, as both lasers emit energies much higher than 2.0 eV (the band gap of WS_2). Laser power was fixed at $250\mu W$ and a 0.1s integration time was set for each step in the map.

5.1.1 First Batch of Heterostructures

In the first batch we fabricated 3 different samples as shown in Figure 40. The first two samples were fabricated by transferring one WS_2 monolayer on top of the WSe_2 monolayer. The third sample presents both a zone comprising a single WSe_2 monolayer and 3 separated small zones presenting heterostructure.

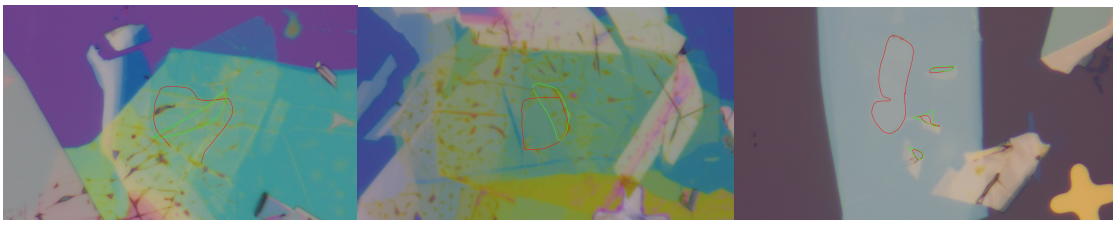

(a) *(b)* *(c)*

Figure 40: Heterostructures fabricated in the first batch as viewed in a reflection optical microscope. Outlined WSe_2 monolayer (red) and WS_2 monolayer (green) shapes pre-transference. (a) Sample 1, (b) Sample 2, (c) Sample 3. WS_2 monolayer marked in green, WSe_2 monolayer marked in red.

As it is extremely hard to see whether the heterostructure was transferred correctly and where the superposition between the monolayers was achieved with an optical microscope, the best approach is to study the heterostructures with micro-PL. Taking into account that a WS_2 monolayer will emit a single neutral excitonic peak at 2.0 eV, while a WSe_2 monolayer will emit at 1.65 eV, we can characterize the relative position of each monolayer by their photoluminescence, and define the heterostructure as the overlapping area of both the WSe_2 and WS_2 PL peaks, or a emission attributable to an interlayer exciton (in the 1.3-1.5 eV range). The integrated PL intensity for different energy emissions for WSe_2 (1.65 eV), WS_2 (2.0 eV) and the interlayer exciton (1.45 eV) is shown in in Figure 41 for sample 1, in Figure 42 for sample 2 and in Figure 43 for sample 3. We will now describe each of these samples below.

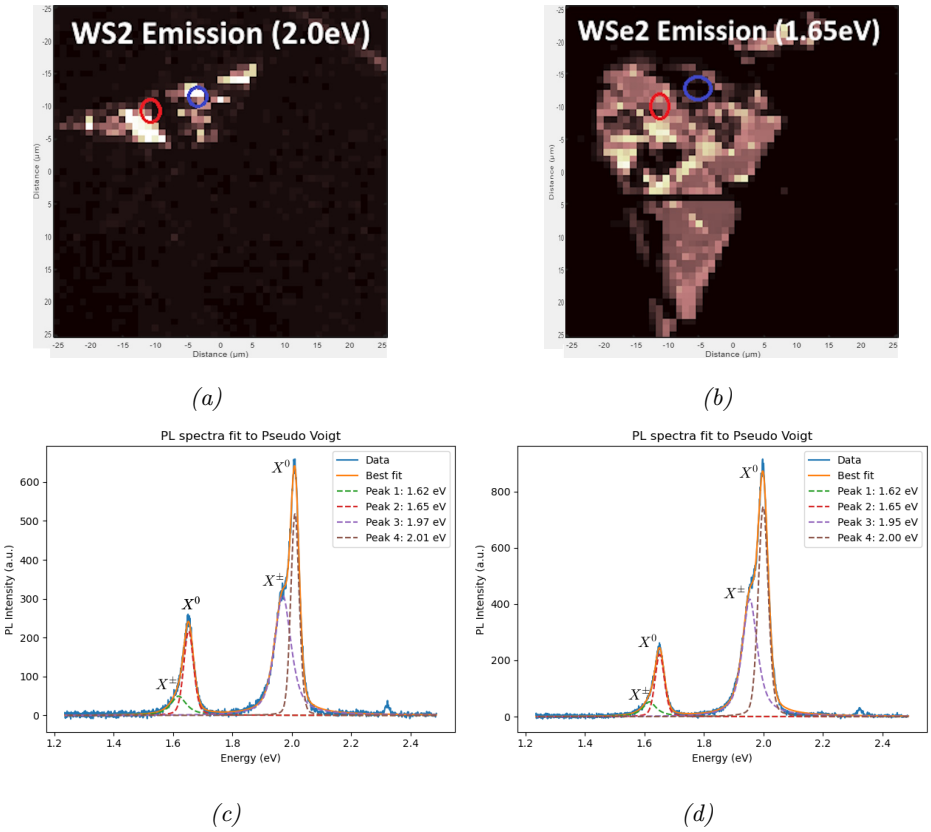

Figure 41: PL-Map of Sample 1 as transferred. (a)Integrated intensity of WS_2 (2.0 eV) emission centered PL-Map. (b) Integrated intensity of WSe_2 (1.65eV) emission centered PL-Map.(c) Spectra measured at red zone. (d) Spectra measured at blue zone. All identified excitons are marked

The first sample presents both monolayer excitonic peaks at all points delimiting the heterostructure. However, no interlayer emission (in the 1.3-1.5eV range) was found for any point in the heterostructure. The heterostructure presented emission peaks at 1.65 eV and 1.62 eV, corresponding to the intralayer neutral exciton (X^0) and trion ($X^{\pm}$) of WSe_2, respectively. For emission peaks in the WS_2 emission range, slightly different peaks centers can be measured. For example, red zone (Figure 41.c) presented peaks at 2.01 and 1.97 eV, while blue zone (Figure 41.d) presented peaks at 2.00 and 1.95 eV. For both of these zones, these peaks correspond to the intralayer neutral exciton (X^0) and trion ($X^{\pm}$) of WS_2, respectively. Additionally, the relative integrated intensities between the monolayers and total intensity are not constant. These small shifts in energies and integrated intensity in the emission of different zones are explained by the changing potential at each point of the sample, mainly produced by strain fields or interactions between the monolayers and their environment.

It must be noted that as this sample did not present any type of interlayer emission, both monolayers act as isolated monolayers, without new excitons arising from interaction between monolayers. For now, it is unknown whether this effect arises due to a large twist angle as presented in Section 2.3.2 or due to a large distance between the monolayers.

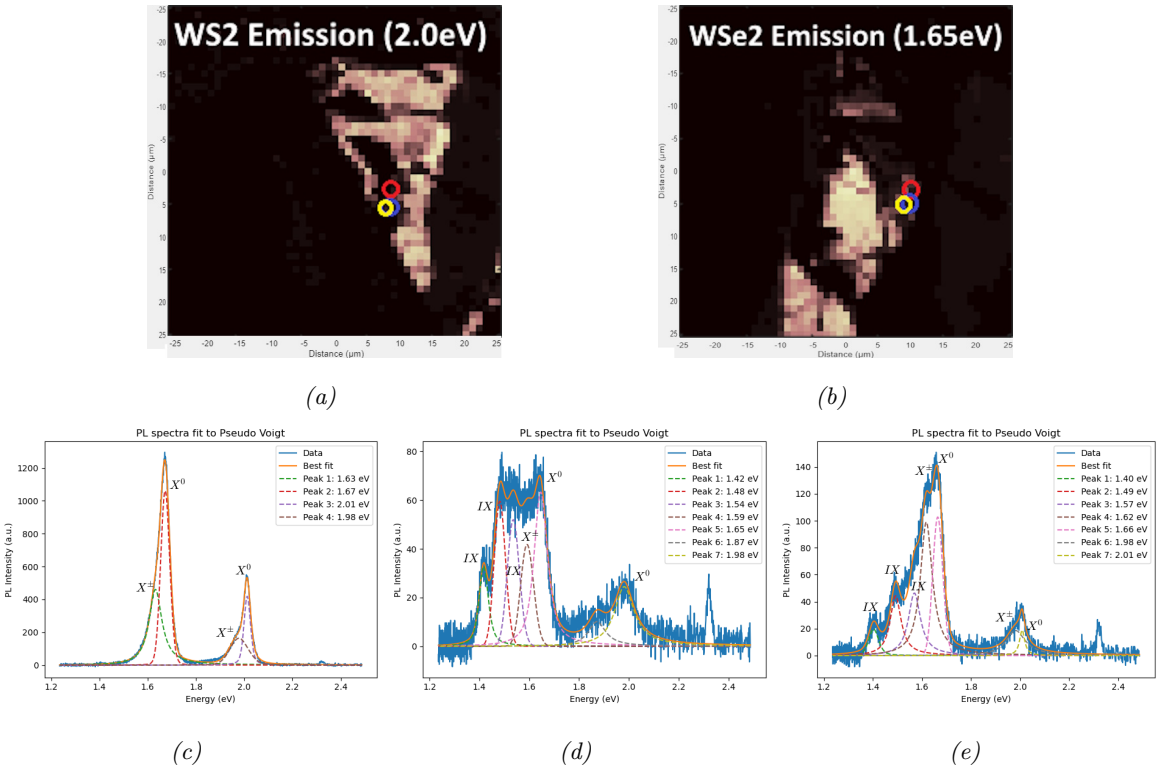

Figure 42: PL-Map of Sample 2 as transferred. (a)Integrated intensity of WS_2 (2.0 eV) emission centered PL-Map. (b) Integrated intensity of WSe_2 (1.65eV) emission centered PL-Map.(c) Spectra measured at red zone. (d) Spectra measured at blue zone. (e) Spectra measured at yellow zone. All identified excitons are marked.

The second sample, shown in Figure 42 presents two types of emission: Some zones where the heterostructure acts as two isolated monolayers such as the red marked zone (Figure 42.c) where the behaviour is the same as in sample 1. Additionally, some zones presented emission in the 1.3-1.5 eV range, such as the blue marked zone (Figure 42.d). This emission can be attributed to interlayer emission. For the WS_2 emission, a 1.98 eV intralayer peak can be fitted, corresponding to the neutral exciton. For the WSe_2 emission, two peaks can be fitted, at 1.65 eV and 1.59 eV. The former corresponds to a neutral exciton (X^0) while the latter, with a difference of energy of 600 meV (double that of sample 1), can be identified as either a charged exciton or a biexciton ($X^{\pm}$). For the interlayer peaks (IX), three could be fitted at 1.59 eV, 1.54 eV and 1.42 eV. These emission peaks can originate from either interlayer excitons or from moiré interlayer excitons. To be able to identify them, radiative lifetimes and/or power dependence measurements must be conducted [51].

It must be noted that where interlayer emission was found, the WSe_2 and the WS_2 excitonic emission presented different behaviour and shifts in energy in contrast to both Sample 1 and adjacent zones in Sample 2 ($1\mu m$ distance) that did not present interlayer emission. This is mainly due to the interaction between the monolayers generating different potentials. Additionally, interlayer emission between adjacent zones can change greatly, as shown in the blue and yellow zones (Figure 42.d and e, respectively) where there is only a distance of $1\mu m$. These changes are mainly due to the moiré pattern of the sample, as discussed in Section 2.3.2, which changes the electronic structure depending both on the position in the pattern and whether atomic reconstruction has occured, locally changing the moiré pattern.

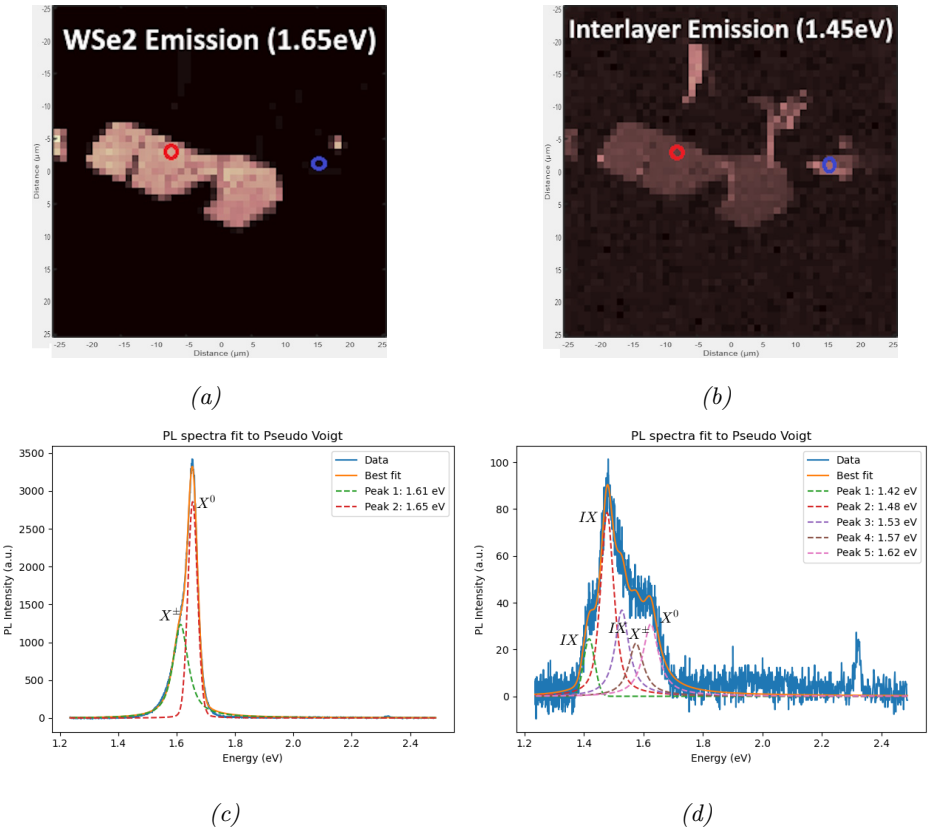

Figure 43: PL-Map of Sample 3 as transferred. (a)Integrated intensity of WSe_2 (1.65 eV) emission centered PL-Map. (b) Integrated intensity of Interlayer (1.45eV) emission centered PL-Map.(c) Spectra measured at red zone. (d) Spectra measured at blue zone. All identified excitons are marked.

The third sample, shown on Figure 43, presents a big monolayer-only zone (seen as a bright continuous zone in Figure 43.a), and a heterostructure (seen as the 3 smaller zones only present in Figure 43.b). For the WSe_2 monolayer, a neutral exciton peak at 1.65 eV (X^0) and a trion at 1.61 eV ($X^{\pm}$) can be detected (Figure 43.c), with no other emission present, as expected. The monolayers has a detectable intensity at 1.45 eV in Figure 43.b although it does not present peaks at 1.45 eV. This is because monolayer emission is extremely bright, allowing the tail to present intensities comparable to that of interlayer excitons. For the smaller zones, they present an emission spectra dominated by the interlayer peaks as seen in the blue zone (Figure 43.d). The number of interlayer peaks (IX) is the same as seen in sample 2, with small shifts in energy. The WSe_2 peaks do show an energy shift of 300 meV and 200 meV for the intralayer neutral exciton and the trion, respectively, compared to those present in sample 2. Most importantly, WS_2 intralayer peaks can not be detected (up to measurement resolution) in any of the interlayer zones, in stark contrast with sample 2. This presents an important result, as a disappearance of the WS_2 peak has not found to be reported in the literature [48] [52] [53]. This effect probably comes from a transference of the WS_2 excitons to interlayer excitons, as it is more favorable for a lower emission energy to occur.

To test the effect in the interlayer emission of varying the distance between the monolayers and whether we can incite interlayer emission on samples that did not have them previously we will anneal the three samples in a convection oven. All samples were annealed 2 hours at 200^{o}C and measured afterwards.

There was an unintended effect present on both Sample 1 and Sample 3 after annealing as shown in Figure 44: presence of a emission at 2.15 eV not attributable to an heterostructure, but to hBN, namely, the presence of defects in the hBN flake. This is surprising, as previously we commented on Section 3.4 that defects on hBN were usually created at the 500ºC range, much higher than the temperatures reached in this work. This result will probably have an effect on heterostructure emission, as there can be interaction between the interlayer excitons and these defects.

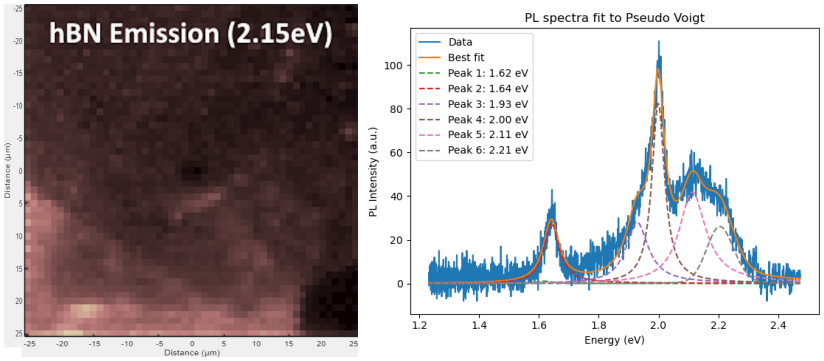

(a) *(b)*

Figure 44: (a) Integrated intensity given by PL map of sample 1 after two hours of annealing centered at 2.15 eV. (b) Representative spectra of the map

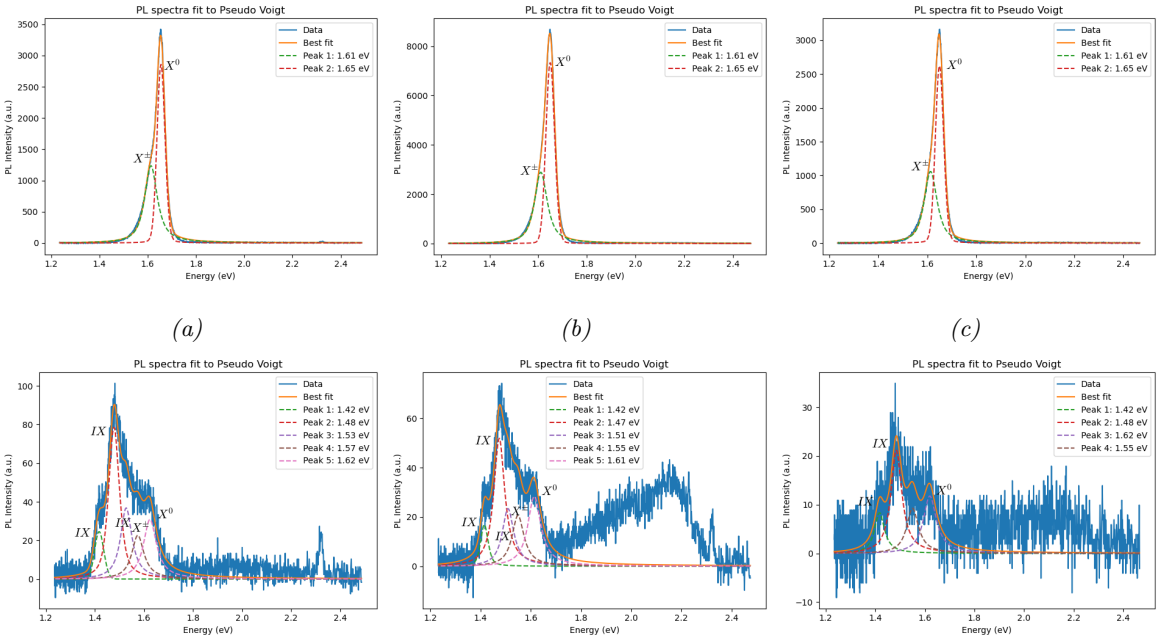

(a) *(b)* *(c)*

(d) *(e)* *(f)*

Figure 45: Evolution of sample 3 in respect to annealing (a-c) Red Zone, (d-f) Blue Zone. (a,d) As transferred spectra, (b,e) spectra after two hours of annealing, (c,f) spectra after four hours of annealing. All identified excitons are marked.

We will first study whether annealing has any effect on monolayer emission. For that, we

will first study sample 3. Taking into account the spectra from Figure 45.a-c, we can see how there is no noticeable shift in the emission peaks of the WSe_2 monolayer nor in the shape of the peak. Thus, we can say that annealing has no effect on the emission of a monolayer. Then, all shifts and changes in the emission of the heterostructures must originate from interlayer interactions, i.e., from the reduction in interlayer distance due to the evaporation of water monolayers and organic contamination or the application of strain due to relaxations in the lattice as the temperature helps the monolayers to slightly reposition.

The blue zone evolution is shown in Figure 45.d-f. When annealed for two hours, we can see how there is both a decrease in the intensity of the emission peaks and a red-shift of around 100 meV for the intralayer neutral WSe_2 exciton (1.62 to 1.61 eV) (X^0). Meanwhile, the trion ($X^{\pm}$) presents a different red-shift of around 200 meV (1.57 to 1.55 eV). For the interlayer peaks (IX), the 1.53 eV peaks shows a red-shift of 200 meV, while the 1.47 eV peak shifts by 100 meV. Meanwhile, the 1.42 eV peak has no noticeable red-shift. For an anneal time of 4 hours, there is even more of a decrease in intensity, making the deconvolution of the peaks more difficult, as there is too much noise in the measurement. Due to this we can not calculate shifts in the PL peaks clearly.

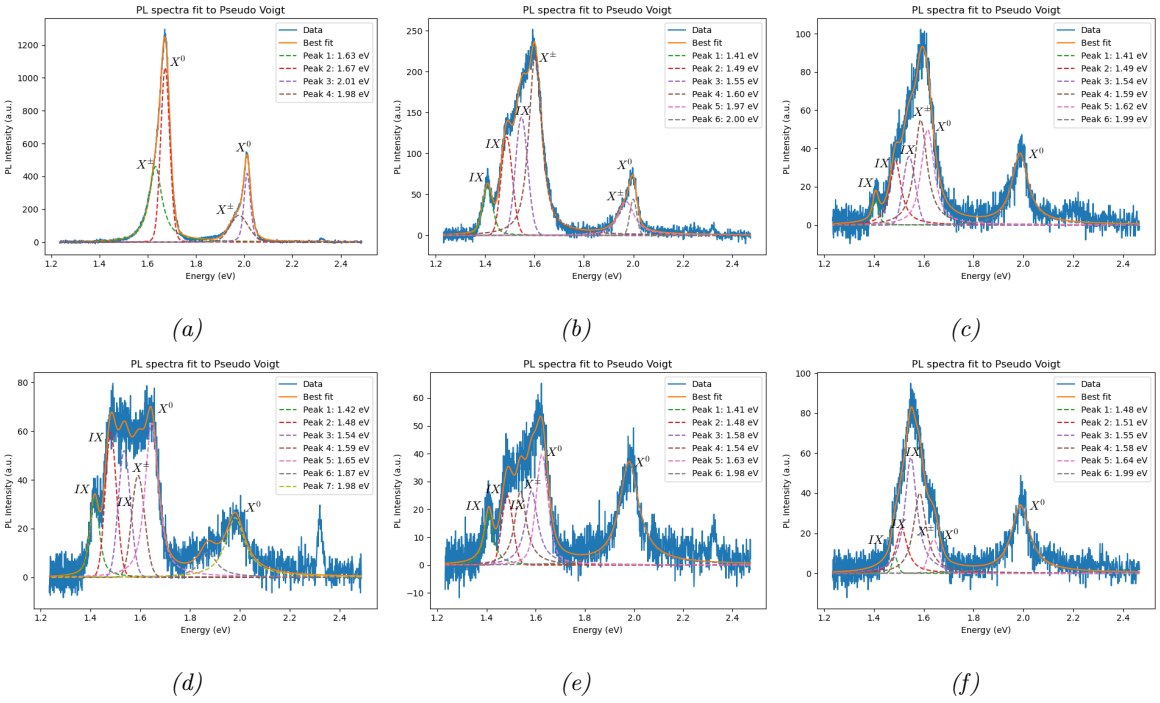

Figure 46: Evolution of sample 2 in respect to annealing (a-c) Red Zone, (d-f) Blue Zone. (a,d) As transferred spectra, (b,e) spectra after two hours of annealing, (c,f) spectra after four hours of annealing. All identified excitons are marked.

Now, we will study sample 2. In Figure 46.a-c we can see the evolution of the red zone with annealing. First of all, we can see how after an anneal of 2 hours, interlayer excitons were formed, thanks to the relaxation of monolayers and the reduction in interlayer distance. Interlayer exctions (IX) are shown at energies of 1.41 eV, 1.49 eV and 1.55 eV. It is of note that the highest energy WSe_2 exciton PL peak is at 1.60 eV, 500 meV lower than expected in a neutral exciton peak. This effect can come from two main mechanisms: a shift in energy due to a strain field (up to 200-300 meV at the highest [54]) and the transfer of neutral charged excitons from the intralayer excitons to the interlayer and charged intralayer excitons as the

1.60 eV PL peak coincides with trion recombination ($X^{\pm}$). For higher anneal times, although interlayer emission energy did not shift, we can detect the intralayer exciton at 1.62 eV (X^0), denoting that this transfer of excitons only occurred at set strain and/or interlayer distance conditions.

For the evolution of the blue zone in sample 2 with annealing, as seen in Figure 46.d-f, the behaviour is similar to the previous sample, where there was a small red-shift in PL emission. Importantly, throughout the anneal, relative intensities between peaks changed greatly, from a dominance of the WSe_2 intralayer peaks in Figure 46.e to a dominance of the interlayer peaks in Figure 46.f

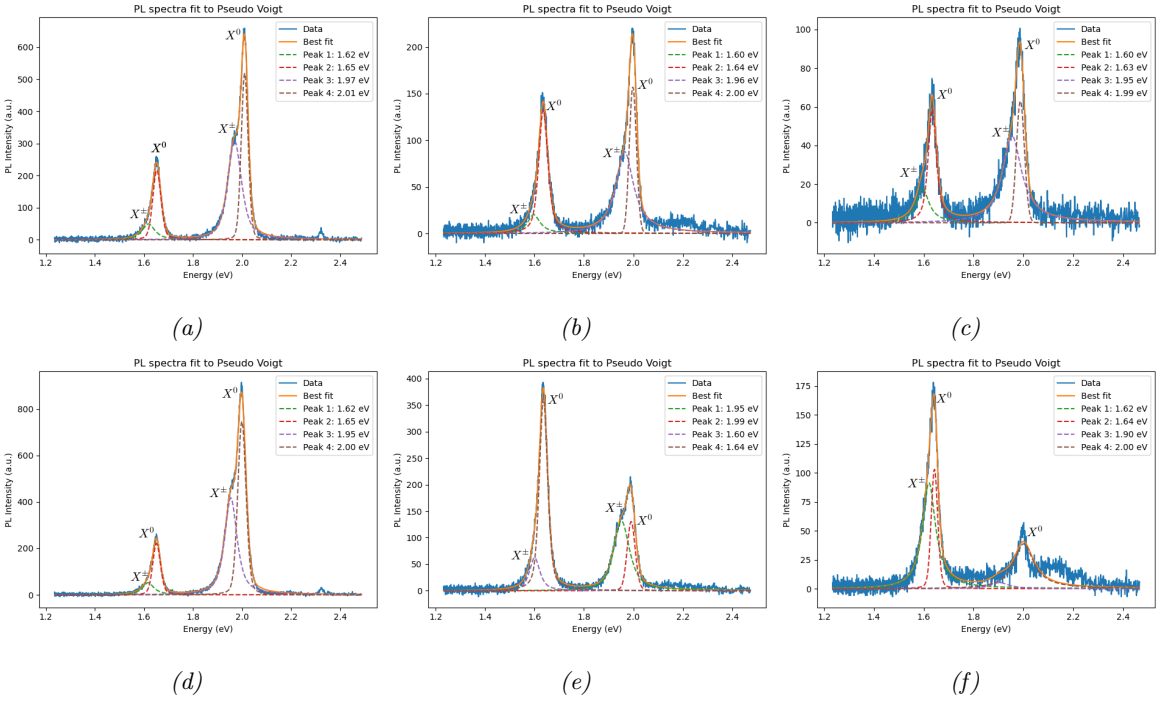

Figure 47: Evolution of sample 1 in respect to annealing (a-c) Red Zone, (d-f) Blue Zone. (a,d) As transferred spectra, (b,e) spectra after two hours of annealing, (c,f) spectra after four hours of annealing. All identified excitons are marked.

Finally, in Figure 47 we present the evolution of sample 1 in respect to annealing. There was no point in the sample that presented interlayer emission at any annealing time, even though there was a change in the relative intensities of exciton-trion and there was a slight shift in energy for both measured zones. This means that while there is some interaction between the monolayers, there is a mechanism that preventing interlayer exciton formation in this sample type.

As we can suppose that the anneal relaxed the heterostructure up to the minimum interlayer distance, the lack of interlayer exciton formation in sample 1 seems to originate from a high twist angle, as discussed in Section 2.3.2, where for twist angles higher than 3^o both monolayers acted as isolated monolayers, as the moiré pattern gives rise to too many domain walls for interlayer excitons to be energetically feasible.

In summary, we can clearly see that all interlayer emission in each of our heterostructures is slightly different in respect to each other, mainly in the relative intensities between the PL peaks. This gives us information that there are changing interaction energies along the

samples. We can also note that interlayer emission is at the 1.4-1.5 eV range, far from the theoretical estimate of 1.3 eV and experimental measurements of interlayer excitons at energies smaller than 1.42 eV [52] [48] [53]. This difference in the energy of emission in our samples, as it barely changes with annealing cannot be attributed to a relaxation of heterostructures with annealing, nor can it be attributed to effects with hBN, as both defect and defect-free samples were measured.

It is important to note that PL-Map measurements of heterostructures are not common in literature, where only emission from interesting points of the sample is shown. This creates difficulties in the study of their emission, as each point creates different emission patterns, two researchers can find different spectra in their heterostructures. Additionally, while the approach of this work was to characterize the entire heterostructure, most points in the sample are not of particular interest in literature as they might not come from high-symmetry points in the moiré pattern or specially high strains, thus, some of the spectra shown in this work show differences with spectra shown in literature.

This interlayer excitonic emission in our samples can be attributed to three main mechanisms: the application of a high strain in points of the heterostructure, thus having only small zones of emission in our heterostructure; a moiré pattern (or various) that creates high symmetry points in the emissive zones of the samples; or a energy potential minima due to the confinement of excitons in a small area heterostructure. If the origin of this interlayer emission is due to these energy potential minima, as both sample 2 and sample 3 presented interlayer emission at small zones in the heterostructure, i.e, where the heterostructure was broken into small pieces was where interlayers were formed; we can predict that in a new sample fabricated with small area heterostructures we will find interlayer emission, while a flat non-broken heterostructure will not present interlayer emission in measurable quantities. Additionally, if the flat heterostructure does present interlayer emission, as the application of strain by transferring flat heterostructures is generally low, it would be hard to argue that this interlayer emission is mainly originated from high strain fields.

5.1.2 Second Batch of Heterostructures

To test the hypothesis discussed above, a second batch of heterostructures were fabricated. As there was a need to diminish the amount of hBN defects present in the samples, high purity hBN supplied by researchers K. Watanabe and T. Taniguchi was used. One flat-like heterostructure (Figure 48.a) with barely any broken parts nor wrinkles was fabricated, while in sample 5 (Figure 48.b), two sets of broken monolayers were transferred on top of each other, creating small islands of heterostructure. This allows us to test whether only point-like heterostructures create interlayer excitons and how they change along these zones.

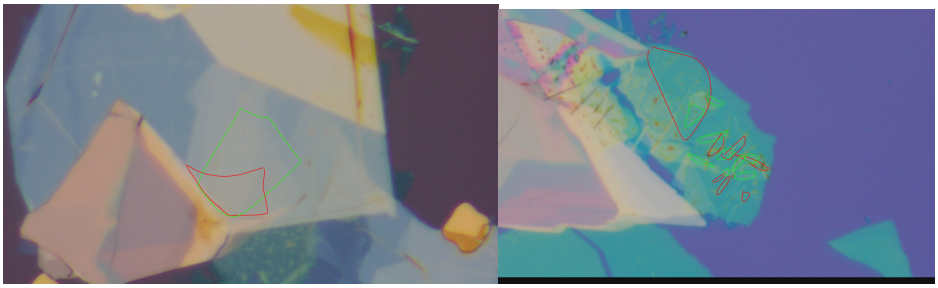

(a) Heterostructure 4 *(b)* Heterostructure 5

Figure 48: Heterostructures fabricated in the second batch as viewed in a reflection optical microscope

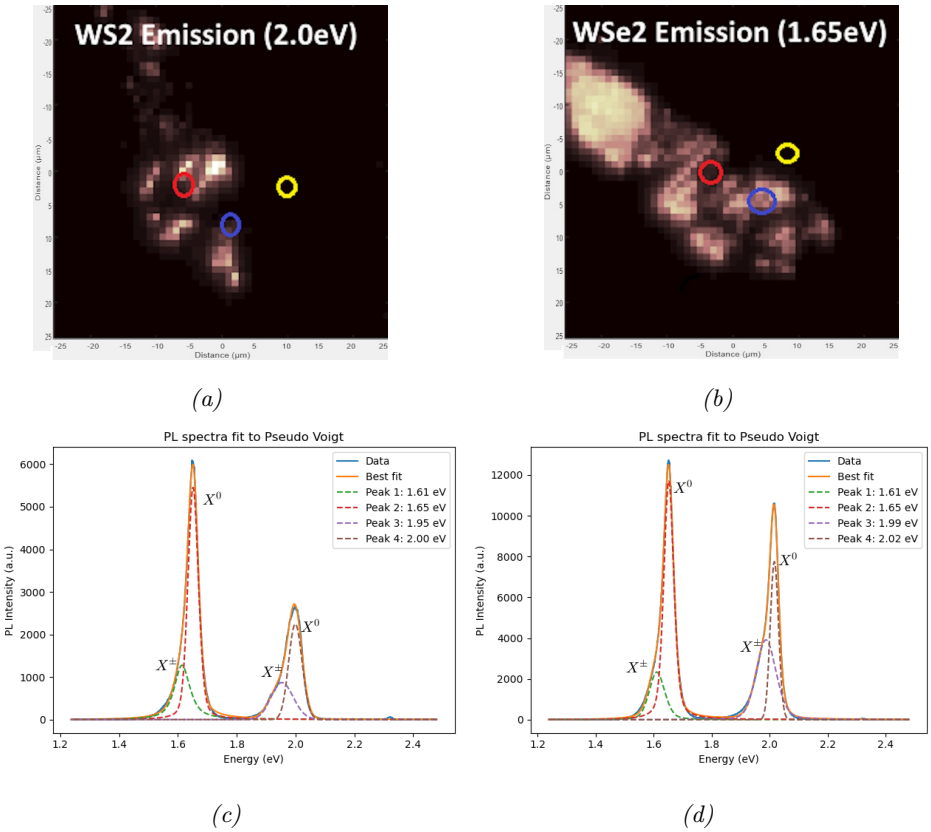

Figure 49: PL-Map of Sample 5 as transferred. (a)Integrated intensity of WS_2 (2.0 eV) emission centered PL-Map. (b) Integrated intensity of WSe (1.65eV) emission centered PL-Map.(c) Spectra measured at red zone. (d) Spectra measured at blue zone. All identified excitons are marked. WS_2 monolayer marked in green, WSe_2 monolayer marked in red.

In Figure 49 we can see the as-transferred emission PL peaks intensity in each point of space for sample 5. In Sample 5 all but one of the "heterostructure islands" show no sign of interlayer emission , although emission from intralayer excitons is much higher than in heterostructures 1-3 (5-10x higher).

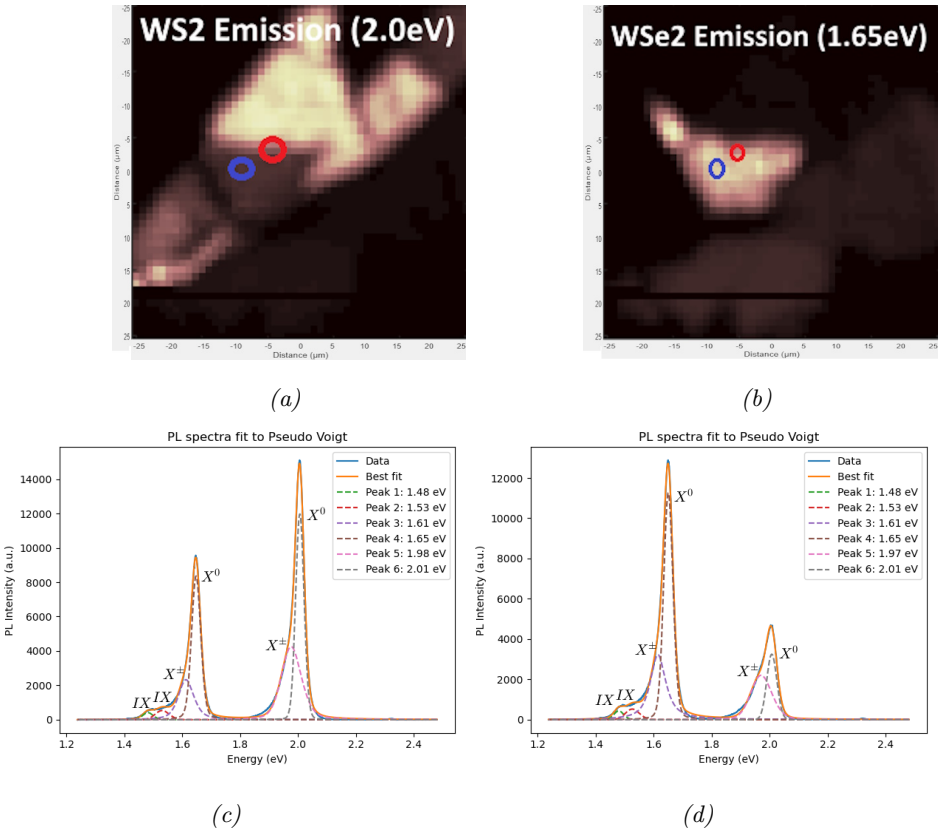

Figure 50: PL-Map of Sample 4 as transferred. (a)Integrated intensity of WS_2 (2.0 eV) emission centered PL-Map. (b) Integrated intensity of WSe_e (1.65eV) emission centered PL-Map.(c) Spectra measured at red zone. (d) Spectra measured at blue zone. All identified excitons are marked.

Meanwhile, sample 4 (shown on Figure 50), where a flat like heterostructure was fabricated, showed a spectra of the intralayer excitons with a small tail at 1.48 eV to 1.53 eV, corresponding to an interlayer-like emission. Most of the area of the heterostructure in sample 4 showed interlayer emission with this tail-like behaviour, while the only change was the absolute and relative intensity of the intralayer peaks.

As before, we will study the evolution of the emission in respect of the annealing time for our samples. We will first study whether Sample 5 can show interlayer emission when annealed. In Figure 51, we can see that there is no appreciable shift in PL peak energy with strain. However, we can see that absolute and relative intensities of the excitons do change with annealing time. This means that there is a change in the potential interaction field between the monolayers.

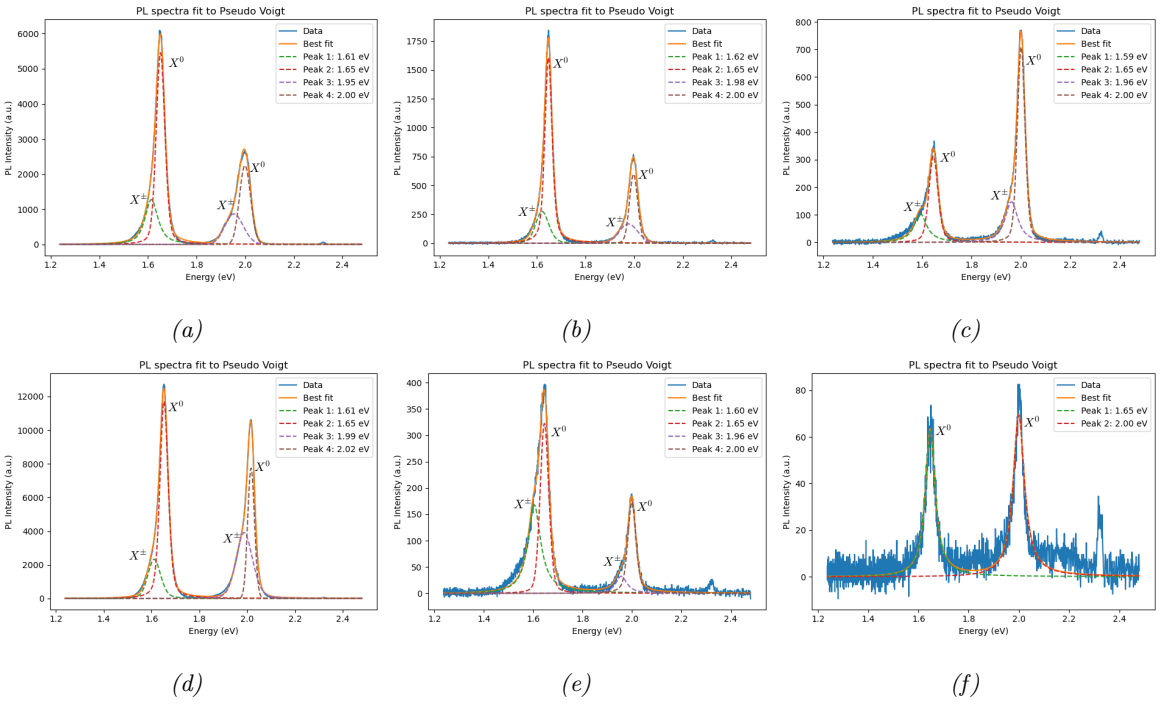

Figure 51: Evolution of sample 5 in respect to annealing (a-c) Red Zone, (d-f) Blue Zone. (a,d) As transferred spectra, (b,e) spectra after two hours of annealing, (c,f) spectra after four hours of annealing. All identified excitons are marked.

There was no interlayer emission when annealed for both red and blue zones as shown in Figure 51, similarly to sample 1 in the first batch. Only in one of the "heterostructure islands" (2 by 2 μm) of the sample can we appreciate interlayer emission (Figure 52). The emission intensity in these zones is two orders of magnitude lower than the isolated monolayers one (100 vs 10000). We could not find a zone in the sample where interlayer emission could be induced by annealing. The interlayer emission in this zone does change with annealing, as previous samples have shown. Although a good fit could not be made as there was a extremely low amount of counts, we can also see that PL peaks are again in the range of 1.4 to 1.5 eV.

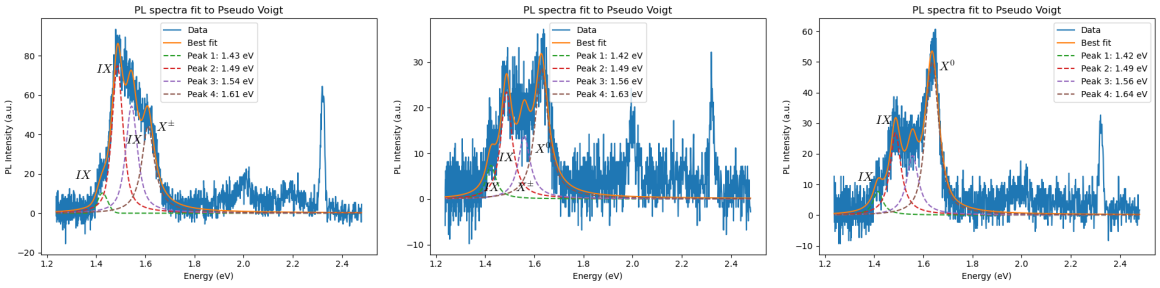

Figure 52: Evolution of one of the islands (yellow circle) of sample 5 in respect to annealing. (a) As transferred spectra, (b) spectra after two hours of annealing, (c) spectra after four hours of annealing. All identified excitons are marked.

Now, for sample 4, as there is interlayer emission across the entire heterostructure, we display both the PL map and two representative spectra of the sample at 2 hours of anneal time (Figure 53) and 4 hours of anneal time (Figure 54).

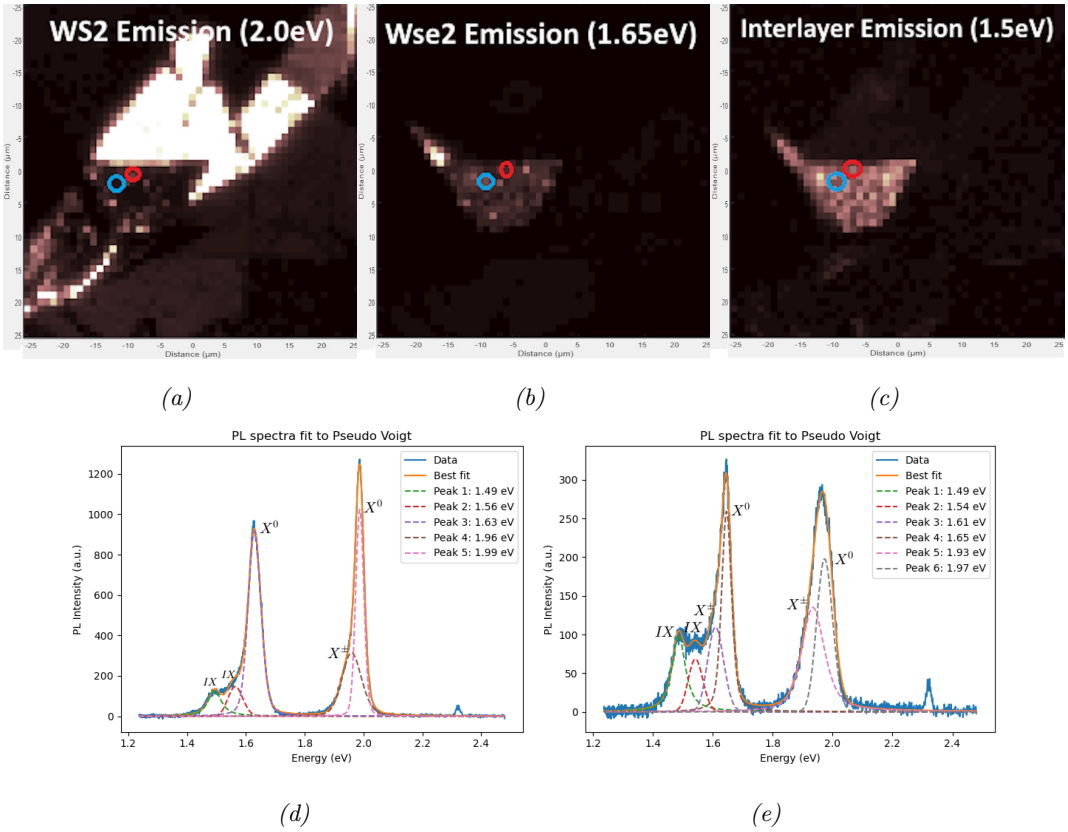

Figure 53: PL-Map of Sample 4 after 2 hours of annealing. (a)Integrated intensity of WS_2 (2.0 eV) emission centered PL-Map. (b) Integrated intensity of WSe_2 (1.65eV) emission centered PL-Map.(c) Integrated intensity of Interlayer (1.5eV) emission. (d) Spectra measured at red zone. (e) Spectra measured at blue zone. All identified excitons are marked.

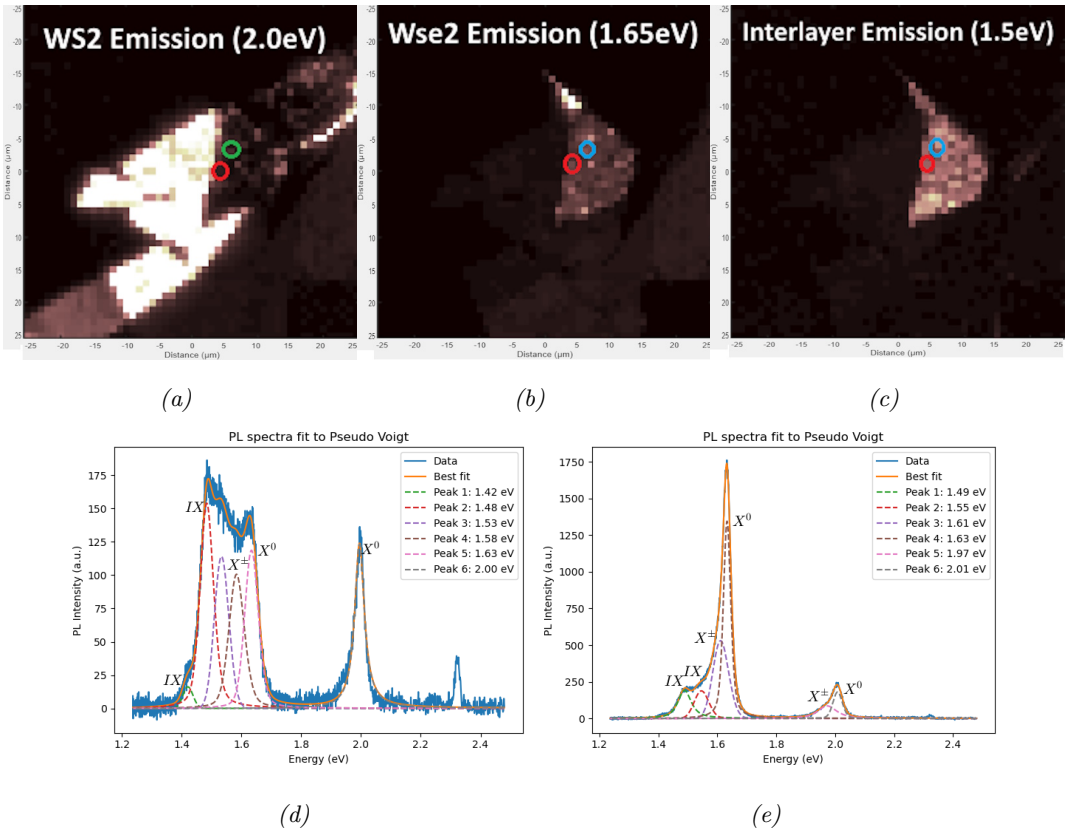

Figure 54: PL-Map of Sample 4 after 4 hours of annealing. (a)Integrated intensity of WS_2 (2.0 eV) emission centered PL-Map. (b) Integrated intensity of WSe_2 (1.65eV) emission centered PL-Map.(c) Integrated intensity of Interlayer (1.5eV) emission. (d) Spectra measured at red zone. (e) Spectra measured at blue zone. All identified excitons are marked.

When looking at the evolution of sample 4 with annealing we can see that interlayer emission changes greatly with annealing. First, points that exhibited a tail like behaviour when transferred, start to increase their intensity when annealed for 2h. And depending on the point in the heterostructure, this increase in intensity can be reversible with more annealing (Figure 53.e and Figure 54.e) or irreversible (Figure 53.d and Figure 54.d), increasing up to an interlayer emission higher than any of the intralayer excitons.

It is important to take into account that when increasing the relative interlayer emission, absolute integrated intensity of the sample decreases. As seen in Figure 53.d and Figure 54.d, we can see both the irreversible effect in annealing and that while intensity of the interlayer emission increased lightly (from 100 to 175 counts), the intensity of the intralayer excitons decreased by one order of magnitude (from 1000 to 150).

Now, if we compare the results with our hypothesis from the first batch, we can see that we can fabricate large area heterostructures with interlayer emission. Meanwhile, only one of the "heterostructure islands" did emit interlayer excitons. That must mean that there is a local effect only present on this zone that is not present in any of the others.

As a moiré pattern (or collection of them) encompasses effects from twist angle, lattice constant mismatch, strain and defects in the sample, it is important to separate the effects on an heterostructure on global (twist angle and lattice mismatch) and local (strain and defects) effects. As discussed in Section 2.3.2, interlayer emission should only appear on those

heterostructures with a low twist angle mismatch ($< 3^{o}$) giving periodic high symmetry points around the heterostructure and/or in zones where there is atomic reconstruction giving rise to local high symmetry points where interlayer recombination can occur. The former is a global effect, while the latter is a combination of both global and local effects.

For atomic reconstruction to occur, either the energy configuration of the local point in the heterostructure must be at a low enough state that a high enough strain (or defect) perturbation can minimize this energy into a configuration where monolayers can interact with each other, or the heterostructure must have a low enough twist angle that it is naturally energetically favorable for this minimization to occur in set points of the heterostructure.

When comparing to experimental conditions, as we currently have no way to measure the twist angle between heterostructures (in our laboratory), we cannot know whether the twist angle of the heterostructures that presented interlayer emission was low enough for it to occur theoretically. However, we do know that a moiré pattern arising from global effects should be detected in semi-large areas of the heterostructure, when not blocked by a non-uniform strain field as seen in Figure 22. However, even under the effect of a strain field, twist angles and the moiré pattern wavelengths do not change by great amounts [55], so there still should be interlayer emissions (though with different energies) when a non-uniform strain field is applied [40]. Given this approach to moiré patterns, when heterostructure emission is only found on a small point in the heterostructure, global causes of moiré patterns look to not be the origin of these type of emission, while more local causes such a local strain field generating atomic reconstruction do seem to fit.

We must remember that twist angle is fixed when transferring one monolayer over another, barring small differences when the monolayer is broken and rearranges slightly. Thus, we can assume that the entire heterostructure will have the same twist angle. As it is highly improbable that all heterostructures were transferred with $< 3^{o}$ angle, we must assume that most heterostructures will not present twist angles low enough for global moiré patterns allowing interlayer interaction to occur.

When presented with the experimental measurements shown in the above sections, we can infer that, all of the heterostructures that did not present interlayer emission in a large area of the heterostructure (samples 1-3 and 5) should not present twist angles lower than 3^{o}. Meanwhile, sample 4, where the heterostructure does present a continuous interlayer emission along its span, can be inferred to have a twist angle lower than 3^{o} as its configuration does gives rise to energy minima along the heterostructure [39].

Now, we need to find a difference between sample 1 and the others where interlayer emission could be detected. In samples 2,3 and 5, as emission was localized in small zones of the sample, the most probable cause of the interlayer interaction seems to be a strain field minimizing the local configuration aiding in atomic reconstruction at these small zones. As these heterostructures were broken around the emission zones and superimposed there, local strain fields can arise. However, while sample 1 did present broken zones too, interlayer interactions could not be found outside of a small energy shift.

We have to remember that atomic reconstruction in heterostructures with high twist angle does not occur because it is not energetically favorable due to the creation of domain walls, thus, it follows that the higher the twist angle, the less energetically favorable this reconstruction can be. When having a finite energy minimization given by a strain field, it seems logical to regard sample 1 as a heterostructure with a high enough twist angle that the strain fields present in the sample are not strong enough to allow the monolayers not to act as isolated monolayers. Meanwhile, sample 2 does show clearly that the strain fields in an heterostructure are changing when annealed, allowing for zones that did not previously have

interlayer interactions to present them (and vice versa).

This separation into twist angle and strain mechanisms helps us to understand the emission of interlayer excitons in a heterostructure, since these two different effects must imply two different exciton production mechanisms that we can exploit to fabricate heterostructures with specific interlayer interactions.

5.2 Results at 4K

In this section, we choose one of the samples discussed previously to measure at an optical cryostat introduced in Section 4.2. As the sample with the greater area of interlayer emission, sample 4 was chosen. When measuring TMDs at lower temperatures, thermal broadening effects are reduced, and peaks that could not be distinguished before from a single 300K curve are detected [56]. Additionally, emission from interlayer excitons is more pronounced at lower temperatures due to the reduced phonon scattering and the resulting increased interlayer electron transfer [57], these effects allows for more complex excitonic states to form in the heterostructure. Finally, reducing the temperature allows the reduction of phonons that could delocalize moiré-trapped excitons, allowing for the detection of excitonic emission from moiré states. Thus, by measuring photoluminiscence at low temperature, we can learn more about the interlayer excitonic complexes and the moiré excitonic states (i.e. moiré potentials) present at each point in our heterostructure.

5.2.1 PL-Map

First, we perform a PL map of our sample to find zones of interest for our subsequent measurements. As previouly discussed, this PL map had to be measured manually, thus, due to time constraints, a PL map with a $2\mu m$ step size and 10 steps in each direction was conducted, giving a measured area of 20 by 20 μm. A 515 nm (1.41 eV) laser was used set at 250 μW with an integration time of 2 seconds. The PL Map is shown in Figure 55. There are some points of interest shown in this map, which we will be discussing below. First of all, it is important to note that emission changes wildly at different points of the sample, whereas at 300K the change was much less pronounced. This effect is due to the increasing importance of the moiré pattern of the sample, giving rise to different energy potentials for excitons at different points in the sample. As we are measuring with a reduced number of phonons, moiré states start to dominate. Thus, as the moiré pattern changes with position [58], so does the electronic structure due to the changing moiré potential, allowing for different excitons to dominate in adjacent positions.

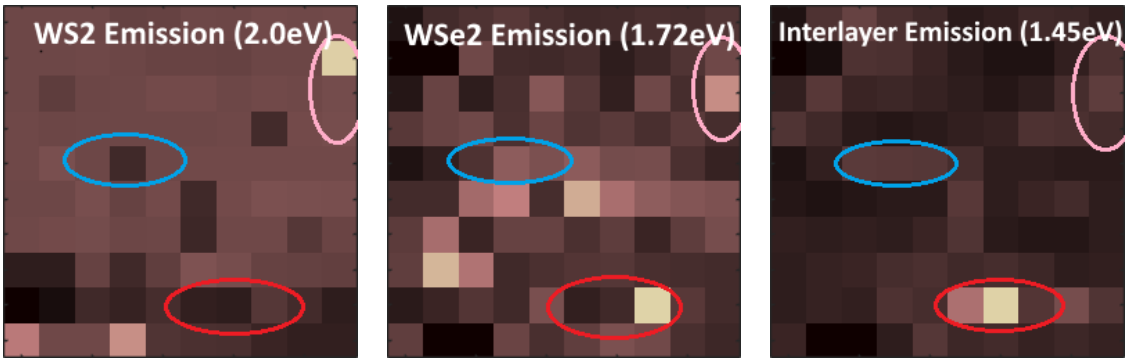

(a) *(b)* *(c)*

Figure 55: PL Map of heterostructure 4 at 4K. Represented integrated intensity of the emission peak around energy in a $20x20\mu m$ space. (a) Integrated intensity of WS_2 (2.0 eV) emission centered PL-Map. (b) Integrated intensity of WSe_2 (1.72eV) emission centered PL-Map.(c) Integrated intensity of Interlayer (1.45eV) emission.

We will now study the different PL spectra present in our heterostructure. Three eliptical segments consisting of 3 adjacent zones (pixels) in the PL map were chosen for the analysis, presenting different types of interlayer emission: the red segment shown in Figure 56, the blue segment in Figure 57 and the pink segment in Figure 58.

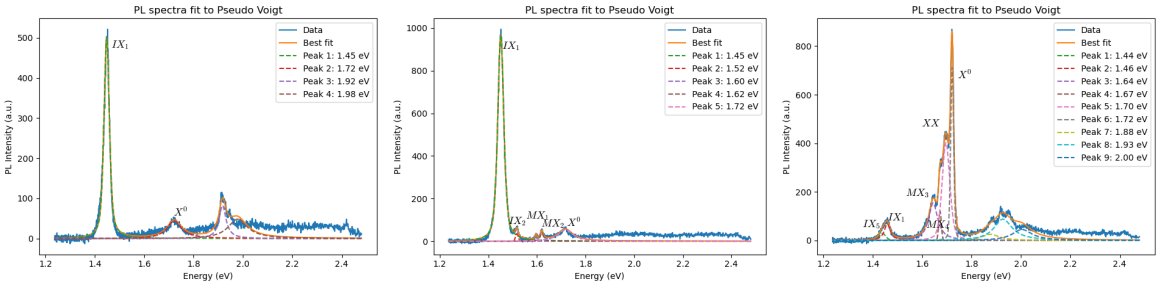

(a) *(b)* *(c)*

Figure 56: Photoluminiscence espectra measured at the red ellipse. (a) Left Side (b) Center, (c) Right Side. All identified excitons are marked. X^0 corresponds to the neutral intralayer exciton, XX corresponds to the biexciton, MX to a moiré intralayer exciton, IX corresponds to an exciton arising from interlayer interaction.

First, we will center on the segment delimited by the red ellipse. We will study these three adjacent zones first in Figure 56. As we can see, there is a high intensity interlayer emission at the center of the red ellipse, while the right zone shows bright WSe_2 emission. At the center of the ellipse (Figure 56.b) almost all of the emission is given by a single interlayer peak at 1.45 eV (IX_1). Meanwhile, intralayer WS_2 emission cannot be distinguished from measurement noise, and interlayer WSe_2 emission shows 3 peaks at 1.6, 1.62 and 1.72 eV, the latter corresponding to the neutral exciton (X^0), while the former correspond to localized exciton complexes [59] [39] arising from the moiré pattern present in our sample (MX_1 and MX_2, respectively) These excitons correspond to moiré excitons arising in the WSe_2 monolayer according to [39]. There is also an additional low intensity interlayer peak at 1.52 eV (IX_2).

For the left side (at $2\mu m$ from the center) shown in Figure 56.a, the IX_1 interlayer exciton (1.45 eV) detected in the previous zone reduces its intensity by half, while the IX_2 (1.52eV) exciton can not be distinguished from measurement noise. Localized WSe_2 intralayer emission can not be distinguished clearly.

On the other hand, the right side does show a completely different behaviour to both the center and left sides: The IX_1 exciton reduces its intensity by one order of magnitude, while IX_2 emission could not be detected. In complete contrast, WSe_2 emission shows a marked increase in intensity, with 4 discernible peaks. As before, the 1.72 eV peak corresponds to the neutral exciton (X^0), while the 1.70 eV peak fits the biexciton complex (XX) [59]. The other 2 peaks (1.64 and 1.67eV) are localized exciton complexes (MX_3 and MX_4, respectively) due to the moiré pattern.

From these observations, and mainly thanks to the WSe_2 peaks, which are extensively studied in literature, we can show how our heterostructure presents localized states due to moiré patterns, giving rise to localized excitonic emission. We can also see how these localized moiré states can present differently even at a small change in position, varying wildly the excitonic emission of our sample. It is also important to note that we were not able to fit correctly the WS_2 emission peaks either by a Gaussian function or a Pseudo-Voigt function, as a result, unless otherwise specified, WS_2 PL emission fits are not shown for the next measurements.

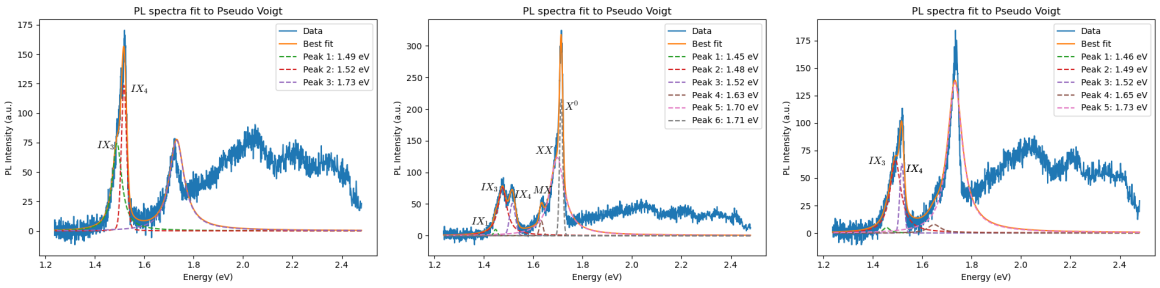

(a) *(b)* *(c)*

Figure 57: Photoluminiscence espectra measured at the blue ellipse. (a) Left Side, (b) Center, (c) Right Side. All identified excitons are marked. X^0 corresponds to the neutral intralayer exciton, XX corresponds to the biexciton, MX to a moiré intralayer exciton, IX corresponds to an exciton arising from interlayer interaction.

Now, we will study the emission around the center of the PL map, in the blue circle (Figure 57). First, we must explain the origin of the emission at 1.8 eV and higher energies in this zone. Most of the top side of the PL map presents this type of emission. Although we have utilized high quality hBN for the heterostructure, it seems that there might still be defects or localized exciton states of hBN in the heterostructure that create this emission. However, most segments do not show such a high emission as in this spectra. This segment is a clear example of the great importance of a high quality defect free heterostructure for a correct characterization of heterostructures, as with this high amount of noise precise WSe_2 exciton emission fitting is futile.

In the center of the blue circle (Figure 57.b) we can see how there are two clear interlayer peaks at both 1.52 eV (IX_2) and 1.49 eV (IX_3). This IX_3 peak is a new excitonic complex, either given by the interlayer exciton or a localized excitonic state. There is a small contri-

bution of the IX_1 exciton . Meanwhile, WSe_2 intralayer emission shows both a neutral or charged exciton peak at 1.71 eV (X^0) and biexciton emission at 1.70 eV (XX).At the right and left sidse, the WSe_2 excitons emission can not be reliably fitted, as there is a high contribution of the hBN/WS_2 noise.

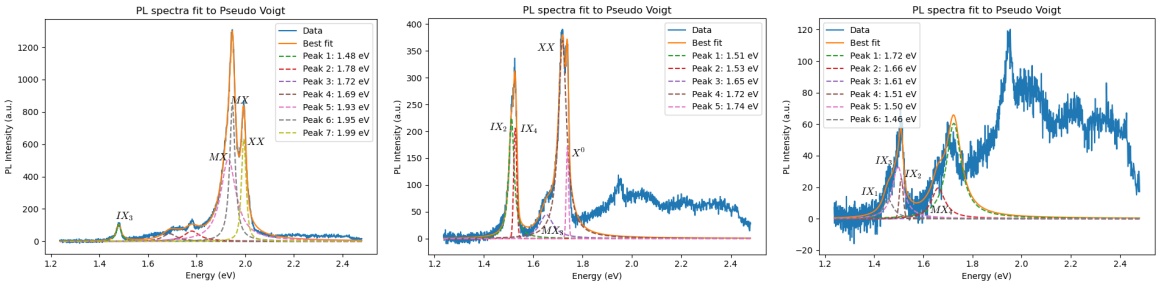

(a) *(b)* *(c)*

Figure 58: Photoluminiscence espectra measured at the orange ellipse. (a) Top, (b) Center, (c) Bottom. All identified excitons are marked. X^0 corresponds to the neutral intralayer exciton, XX corresponds to the biexciton, MX to a moiré intralayer exciton, IX corresponds to an exciton arising from interlayer interaction.

We will lastly study the emission around the top-right corner of the heterostructure, as shown in the orange ellipse (Figure 58). At the center of the zone, we can see how there is a narrow emission peak of interlayer excitons , at 1.51 (IX_2) and 1.53 eV (IX_4), and WSe_2 emission shows a neutral exciton at 1.74 eV (X^0), and a biexciton (XX) at 1.72eV. There is also a localized excitonic state emission at 1.65 eV (MX_3). For the bottom zone, the IX_1 interlayer excitonic emission peak can be detected although at a lower total intensity.

For the top zone, interlayer emission shows a single peak at 1.48 eV (IX_3), while WSe_2 emission can not be fitted correctly. WS_2 excitonic peaks show clearly with a high intensity, the 2.0 eV peak might be attributed to a trion or biexciton (XX), although as all remaining emission peaks are all lower than 1.98 eV [60], lower energy contributions (< 1.95 eV) should originate from localized excitonic states (MX).

Given this analysis of different zones of the heterostructure, we are able to infer that for future analysis a high resolution ($< 1\mu m$) PL Map is needed in order to study the transition between different moiré potentials. However, much information was achieved from this low resolution mapping. First, as WSe_2 can be separated into global excitonic states and localized excitonic states, where global excitonic states keep appearing at different points of the sample (such as the 1.72 eV neutral intralayer exciton), so do some interlayer excitons seem to appear at most positions. These were the IX_2 exciton, that could be detected at almost all of the zones measured, and the IX_1 exciton, that although sometimes had a low intensity, it was detected in most of the zones measured. These interlayer excitonic states were usually accompanied by the neutral intralayer WSe_2 exciton and the intralayer biexciton.

5.2.2 Power Resolved Measurements

To study the possible origin of the interlayer excitons, we will conduct a series of power resolved measurements. In excitonic complexes at low temperature [61] [62], there is a clear dependence of both the neutral, the charged exciton and the biexciton in respect of excitation power. For

each excitonic complex. integrated intensity (I) can be adjusted to the power law given by Equation 9, where a is a constant for the fit and α gives us the dependence of the fit [63]. For neutral and charged excitons, as their emission shows a linear dependence with excitation power, their fit should output $\alpha \approx 1$. For biexcitons, which show a quadratic dependence with excitation power, it is much easier for them to form when exciton density is higher, thus their fit should output $\alpha \approx 1.5 - 2$. For moiré trapped excitonic states, as they are formed in a localized state, their behaviour varies depending on the moiré potential, additionally at higher excitation powers the localized states can saturate hindering further excitonic emission growth. Thus, depending on the localized state that the moiré exciton forms, intensity growth can follow a lineal dependence up to a saturation power where it becomes roughly constant [64][65], or it can show sublinear growth up to a saturation excitation power [63]. Depending on the localized state, saturation can be achieved at lower or higher excitation powers, with some localized states not reaching saturation until high excitation power in the order of 0.3 mW is reached [66].

$$I = a \cdot P^{\alpha} \tag{9}$$

With this power dependence of excitons in mind, by performing a sweep over excitation powers, we should be able to distinguish between global interlayer excitons (neutral, charged and biexcitons) and localized excitons (moiré trapped). Using the polarizer setup discussed in Section 4.2.1, we are able to sweep over incident powers ranging from 8 μW to 1206 μW. With this setup we are able to create a map with respect to incident power as shown in Figure 59. Given this map, and by knowing the minimum and maximum excitation power we can fit using Malus Law the excitation power for each angle.

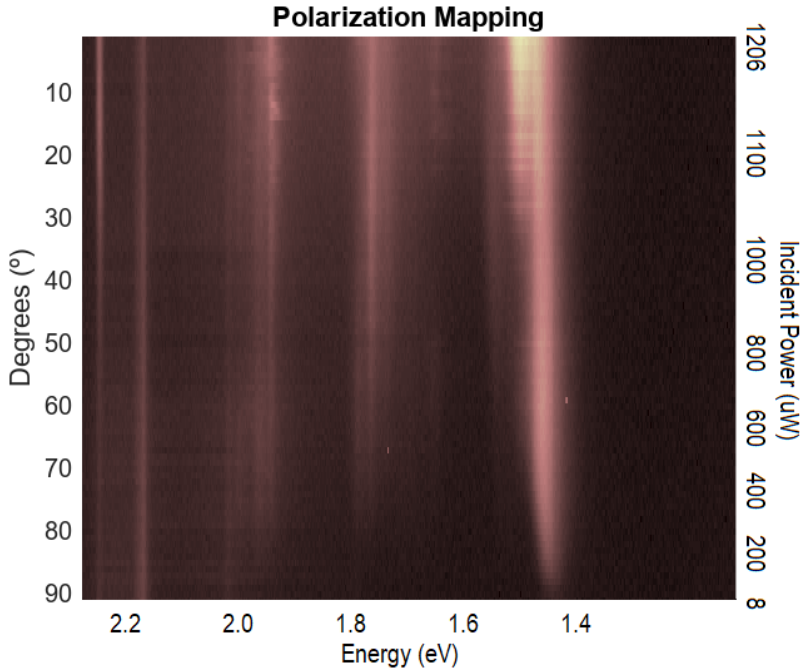

Figure 59: Polarization Map of Zone 1. Intensity for each energy step. 1206 μW at 0^{o} and 8 μW at 90^{o}. Angles can be related to incident power using Malus Law.

We will study the dependence on laser power for four different zones of the heterostructure. Due to technical limitations, the zones measured here could not be the same as the zones

measured in the previous section. The four zones studied were chosen because they represented different behaviours in the emission of the heterostructure.

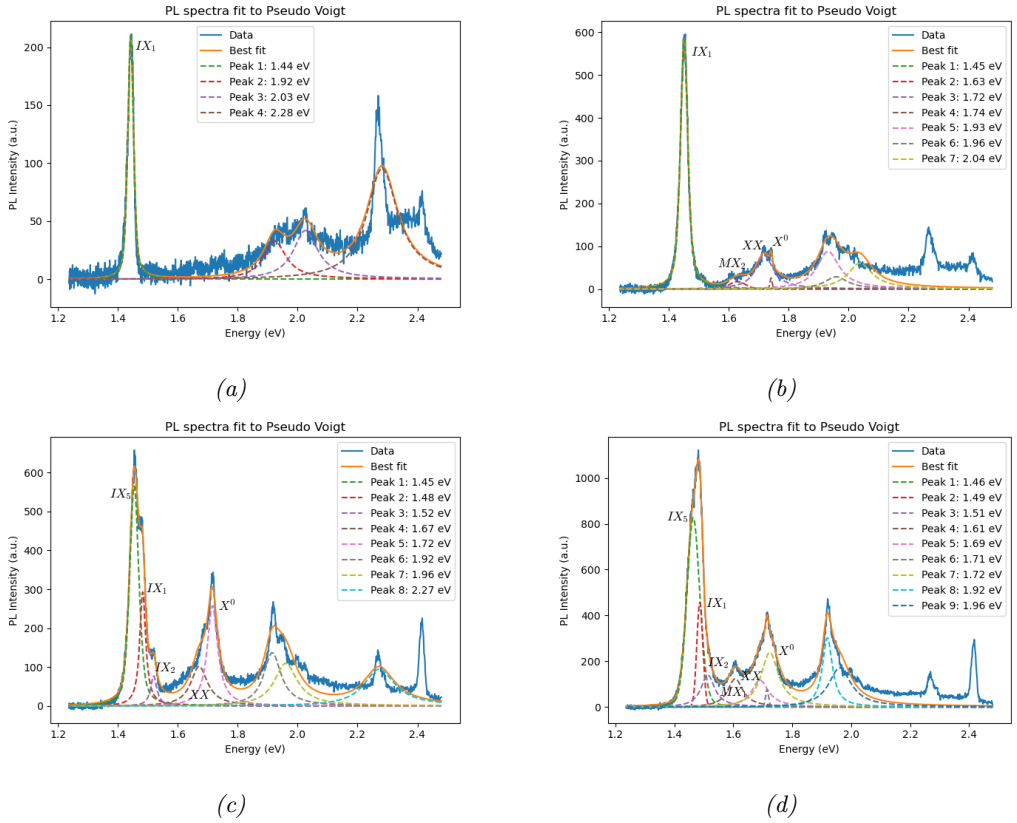

Figure 60: Spectra evolution of zone 1 under varying laser excitation power. (a) $100\mu W$, (b) $400\mu W$ (c) $900\mu W$, (d) $1200\mu W$. All identified excitons are marked. IX denotes both interlayer and moiré interlayer excitons.

We show the emission for zone 1 at 4 different excitation powers in Figure 60. First, emissions peaks higher than 1.8 eV can not be fitted properly, mainly due to the same reasons as in the previous section: the presence of defect emission of hBN. For the WSe_2 intralayer behaviour, we are barely able to detect its emission at 100 μW (Figure 60.a), while at higher excitation power its emission starts to show clearly, starting with the biexciton at 1.72 eV (XX) followed closely by the neutral intralayer exciton X^0 at 1.74 eV (Figure 60.b). There is also a localized emission at 1.63 eV (MX_2). There is a 200 meV redshift for the intralayer peaks with increasing laser power which was expected as discussed in [67]. For the interlayer behaviour, a clear narrow peak at 1.44-1.45 eV (IX_4) could be observed for higher excitation power (Figure 60.c), while for a higher incident power one more IX exciton detected, at 1.52 eV (IX_2) (Figure 60.c).

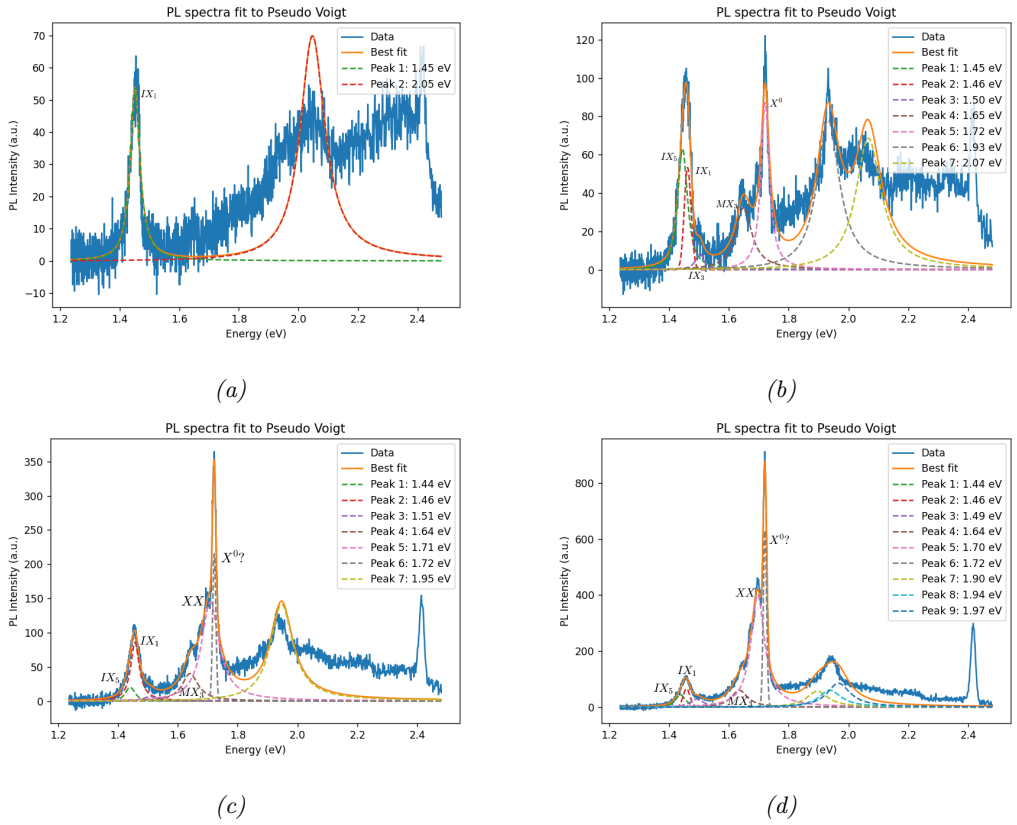

Figure 61: Spectra evolution of zone 2 under varying laser excitation power (a) $400\mu W$, (b) $700\mu W$ (c) $900\mu W$, (d) $1200\mu W$. All identified excitons are marked. IX denotes both interlayer and moiré interlayer excitons.

For the second zone shown in Figure 61, as the emission intensity is extremely low, we start to measure at an incident power of 400 μW. At low excitation power, only the 1.45 eV IX_1 peak can be fitted (Figure 61.a), incresing the excitation power, another close peak at 1.44 eV (IX_5) can also start to be discerned (Figure 61.b). At 700 μW, WSe_2 emission is high enough to measure both the 1.72 (X^0) exciton peak and the 1.65 eV (MX_3) peak, while there is also a small contribution from an interlayer exciton IX_3 at 1.50 eV (Figure 61.b). For $900\mu W$ (Figure 61.c), the IX_1 exciton starts to dominate interlayer emission. In the case of the intralayer WSe_2 emission, we measure an extremely narrow peak at 1.72 eV (X^0?), accompanied by broader peaks at 1.71 eV (XX) and 1.64 eV (MX_3). For $1200\mu W$ (Figure 61.d), it seems that the interlayer peaks have saturated, with slight interlayer emission around 1.49 eV (IX_3). For the WSe_2 exciton emission, the 1.72 eV (X^0?) emission shows a full width at half medium of 12 meV (5 nm), the narrowest recorded in this work. An emission as narrow is not common in neutral excitons. Meanwhile, there is a clear increase in the integrated intensity of the emission peak of 1.70-71 eV (XX) while that of the peak around 1.64 eV (MX_3) does not seem to increase as much with excitation power as expected of a moiré exciton.

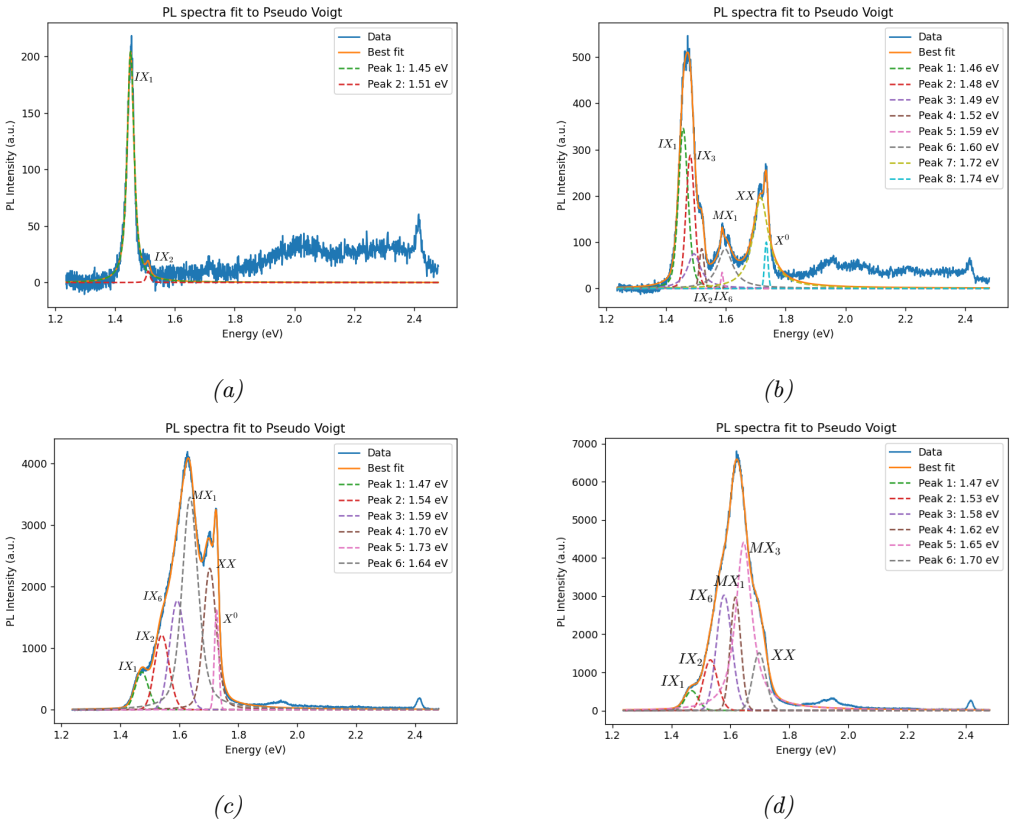

Figure 62: Spectra evolution of zone 3 under varying laser excitation power. (a) $100\mu W$, (b) $400\mu W$ (c) $900\mu W$, (d) $1200\mu W$. All identified excitons are marked. IX denotes both interlayer and moiré interlayer excitons.

For the third zone shown in Figure 62, at low power levels only two interlayer peaks can be measured reliably , a bright 1.45 eV (IX_1) exciton and a small amount of emission from an IX_2 (1.52 eV) exciton (Figure 62.a). When increasing the excitation power (Figure 62.b), IX_1 emission is measured clearly, with an extra high intensity peak close by at 1.48 eV (IX_3). 2 pair of intralayer excitons can now be observed: a pair of peaks at 1.74 eV (X^0) and 1.72 eV (XX) and another pair at 1.60 eV (MX_3) and 1.59 eV (MX_1). At excitation powers of $800\mu W$ and higher (as shown on Figure 62.c,d) interlayer and WSe_2 peaks are convoluted into one single extremely bright peak. There are also 1 more IX exciton at 1.59 eV (IX_6) that shows a clear redshift with increasing excitation power. At the highest measured excitation power, the X_0 exciton emission can not be reliably fitted. It is important to note that, as all 6 peaks are convoluted into one, these fits can not be relied upon to detect the peak center with a precision lower than 20 meV, as different fits with close starting conditions will vary around that value.

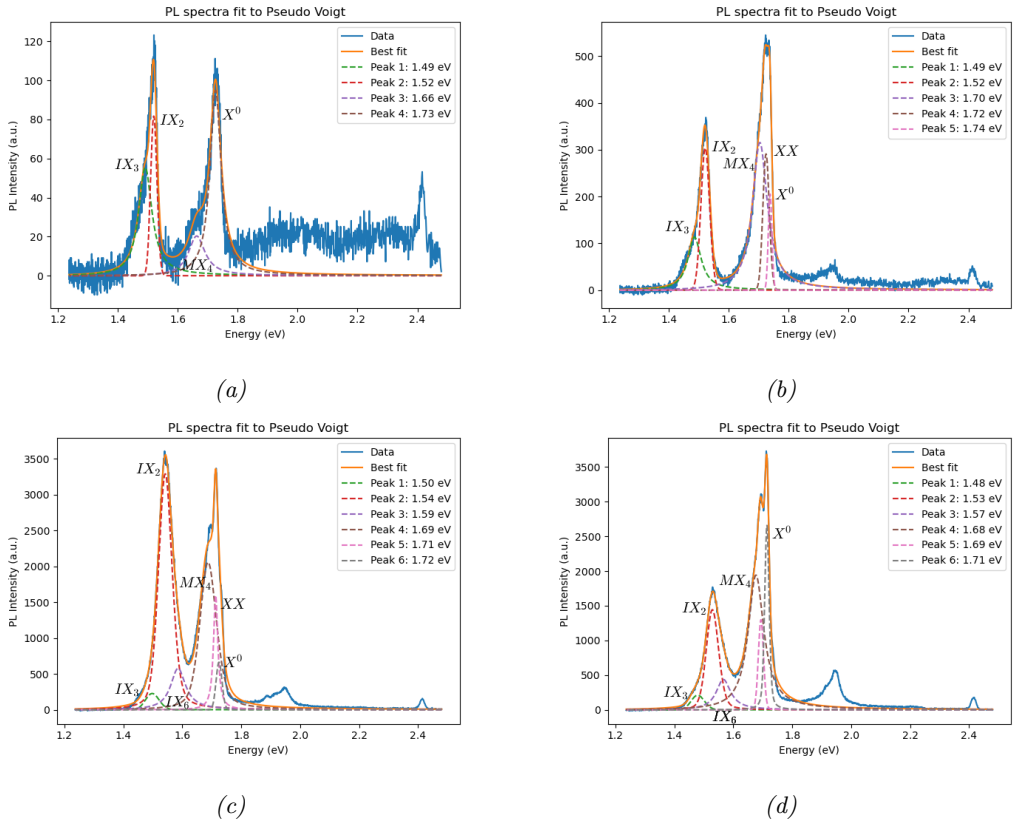

Figure 63: Spectra evolution of zone 4 under varying laser excitation power (a) $200\mu W$, (b) $400\mu W$ (c) $900\mu W$, (d) $1200\mu W$. All identified excitons are marked. IX denotes both interlayer and moiré interlayer excitons.

For the fourth zone shown in Figure 63, spectra differs from previous zones measured, as we can detect clearly at low excitation power two pairs of excitons (Figure 63.a). For the first pair, we measure interlayer excitons IX_2 and IX_3, while the second pair shows the MX_4 moiré intralayer exciton and the neutral intralayer exciton X^0. Each of this pairs combine to form a more convoluted peak at higher excitation powers (Figure 63.b). When increasing the excitation power, these pairs become trios (Figure 63.c-d), with excitonic emission at 1.59 eV (IX_6) and 1.70 eV (XX), respectively. There does seem to be a marked red shift in the WSe_2 emission of around 200 meV, meanwhile, the interlayer peaks do not show a clear tendency with excitation power.

Once these zones are all introduced and different spectra around the sample is measured, we can try to analyse the evolution of the center energy for each of the peaks and their intensity in respect to excitation power. With this approach, we can study the possible energy shifts in our excitonic emission present in our heterostructure and, by fitting to the power law given in Equation 9, find the excitonic complexes responsible for each of the peaks. With this approach, we will be able to separate the interlayer excitons into Interlayer neutral excitons (IX^0), interlayer biexcitons (IXX) and Moiré or Localized (IMX) excitons. We extract a spectra every $100\mu W$ and deconvolute the peaks inside.

As the Photoluminiscence spectra presented a low number of counts and peaks were usually close together, a precise deconvolution could not be achieved. Due to this, the center of the peak can vary by 0.1-0.2 eV in the worst case. Additionally, the integrated intensity for 2

close-by peaks could not be measured reliably, resulting in some measurement errors. Not all mentioned excitons are present in the following analysis: WS_2 peaks could not be fitted reliably in any of the zones, there were also some excitons that could not be measured in one or two excitation powers, where we skip that excitation power in our fit for that exciton. Additionally, some peaks only appeared on one or two excitation powers for each zone. As they appeared extremely close to others that did appear in most of the polarization map, we assumed it was a fitting error and added their integrated intensity to the exciton that did appear (although the change is usually in the order of $5-10\%$).

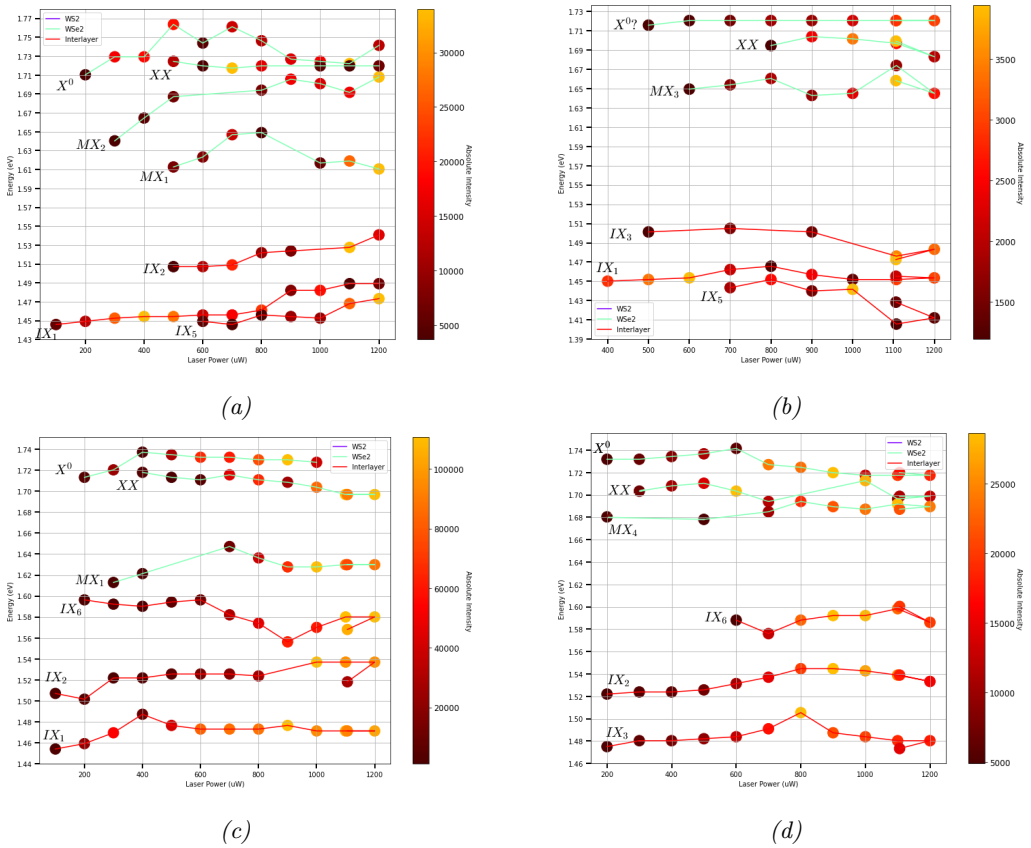

Figure 64: Exciton peak and evolution of each zone under varying laser excitation power. Color of the markers are given by their Integrated Intensity as shown in the heat bar. (a) Zone 1, (b) Zone 2, (c) Zone 3, (d) Zone 4.

In Figure 64, we plot each of the centers of the peaks analysed for each laser power in each of the zones discussed previously. The marker color is given by the integrated intensity of the peak in a heat map. As discussed above, not all peaks that could be detected previously are plotted, as they only appeared in one or two excitation powers, and a tendency could not be measured. Additionally, in order to measure the stability and reversibility of the peaks under a high excitation power, zones 2,3 and 4 were subject to an extra polarization sweep of 0^{o}-(-10^{o}), i.e., a reversal of the incident power into 10^{o}. Each zone has a different collection of peaks, but most zones have a number of repetitive interlayer excitons: the IX_1 exciton at zones 1, 2 and 3; and the IX_2 eV peak at zones 1,3 and 4. Meanwhile all zones show WSe_2 intralayer excitons X_0 and moiré intralayer exciton emission. There was emission at zones 3 and 4 just below the 1.6 eV mark (IX_6), this emission could be either from localized states appearing in the intralayer or the interlayer. As in zone 4 (Figure 63) we detected it in the

interlayer convoluted peak, we assume it came from interlayer interaction.

Now, we will focus on the shifts in the peak energy measured in our excitonic emission. As the precision of the measurement of the center of the peak is not specially reliable (in the order of 0.02 eV), we will only study the tendencies in respect of laser power.

For zone 1, shown in Figure 64.a, at low excitation power $< 600\mu W$, interlayer emission presents a slight blueshift ($2meV/100\mu W$) while WSe_2 intralayer emission presents a sharp blueshift in all of its excitons, with a maximum shift of 0.05 eV for the IX_1 exciton at 300 μW (up to $100meV/100\mu W$). At higher excitation power, all of the interlayer excitons keep presenting a blueshift, with a higher slope of around $7meV/100\mu W$; meanwhile, the intralayer excitons either show a constant behaviour with a slight redshift (which can not be reliably measured) or present a clear redshift as is the case of the MX_1 exciton, with a slope of around $5meV/100\mu W$.

For zone 2, shown in Figure 64.b, there is barely any shift with respect to laser power. Whereas the intralayer exciton shows a variation of the center of the peak in its lowest energy exciton, it is quickly recovered. In the case of interlayer excitons, all but the IX_1 exciton present clear red shift, in the order of $6meV/100\mu W$. The IX_1 interlayer exciton shows an almost constant behaviour with respect to excitation power.

When testing for reversibility, the only excitons whose emission shifted were the ones with the lowest energy (IX_5 and MX_3), which shows a blue-shift to power values closer to between 1000 and 1100 μW (≈15 meV). This effect can be explained as the heating of the sample due to the incident laser intensity , thus increasing phonon dispersion and slightly delocalizing the lowest energy moiré states. This delocalization forces the minimum energy of the states to slightly shift, either to higher or lower energies [68].

For zone 4, as shown in Figure 64.d, behaviour follows closely zone 2 for the WSe_2 intralayer peaks. For the interlayer peaks, however, instead of a red-shift, we find a slight blueshift at lower excitation power of $3meV/100\mu W$ and a redshift at higher excitation powers of $3-5meV/100\mu W$. However, the IX_6 exciton shows a slight blue-shift of the $5meV/100\mu W$ until it decreases at the highest excitation power reached. When testing for reversibility, both lower energy excitons (IX_3 and MX_4) presented a red-shift or around 7 meV in both cases.

Lastly, zone 3 (Figure 64.c) shows a different evolution from the previous zones, with a clear blue-shift of all but one exciton peaks at low excitation power ($< 400\mu W$) with a slope of $16meV/100\mu W$. Meanwhile, the IX_6 interlayer exciton shows a constant behaviour at low power. For higher excitation powers, intralayer peaks suffered a slight red-shift of around $3meV/100\mu W$, while interlayer peaks differed greatly: The IX_1 exciton showed an almost constant-like behaviour, while the IX_2 exciton increased its energy by around $3meV/100\mu W$, finally The IX_6 exciton at high incident power shows a clear redshift of around $2meV/100\mu W$ (we have dismissed the 900 μW energy as the spectra was too convoluted to calculate the center of the peak correctly). When testing for reversibility, excitonic emission showed a clear contrast in respect to the previous zones, as none of the lowest energy excitonic states (IX_1 and MX_6) suffered irreversibility. However, both the IX_2 and IX_6 excitons showed a start red-shift of 20 and 12 meV, respectively. This should point to the fact that in this zone, the most localized excitons are these two, in contrast with the other zones where the most localized excitons were those with the lowest energy.

We will now study the power dependence of integrated intensity (Figure 65- Figure 68) for the exciton peaks studied in Figure 64 in order to identify the excitonic complexes that create the emission detected. First, we will analyze the power dependence of the WSe_2 excitons, as literature has studied them previously. In order to reduce the effects of variable temperature,

the -10º emission is shown to visualize the change in intensity but was not included in the fit to the power law

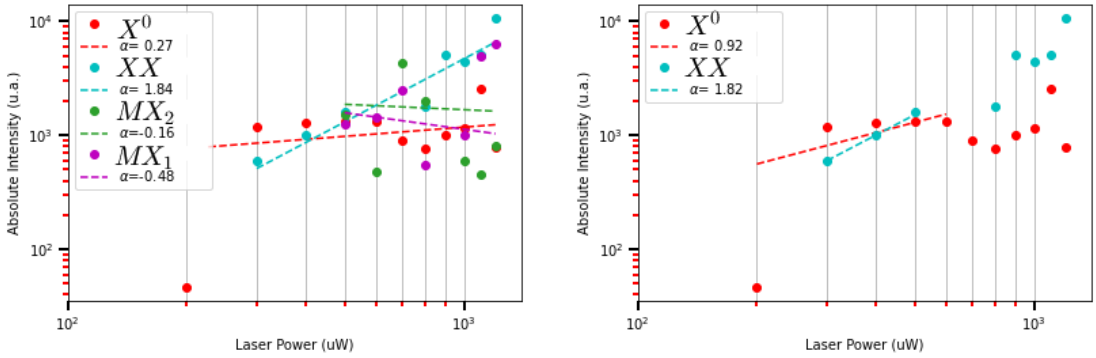

(a) *(b)*

Figure 65: Integrated Intensity evolution of Zone 1 Intralayer emission under laser excitation power. Fitted to power law given in Equation 9 for (a) all power, (b) power of less than $500\mu W$

The power dependence for Zone 1 is shown in Figure 65.a. Here, we can see how the XX peak fits to $\alpha \approx 1.84$, inside the 1.5-1.8 range that fits the biexciton [61] [62]. Additionally, this emission shows at around 1.7 eV with a slight shift, allowing the energy of the peak to also fit the WSe_2 biexcitonic emission. Thus, we can regard the XX peak as a intralayer biexciton, as expected. For the MX_1 and MX_2 emission, α is negative, as these peaks look to be saturated even when we start to be able to detect them, thus, these 2 excitons are prime examples of localized excitonic states or moiré intralayer excitons. Finally, the X_0 (1.74 eV) peak has a sublinear growth when regarding the entire excitation power sweep; however, when regarding only at low excitation powers (Figure 65.b), the exciton shows a clear linear dependence. As in [61] the neutral exciton was measured only at low excitation powers, we must use other Wannier-Mott excitons measured in other materials, which should show similar emission. From [69], neutral excitons show saturation at higher excitation powers, thus we can conclude that the 1.74 eV (X^0) peak is a neutral (or charged) intralayer exciton, which coincides with the experimental neutral intralayer exciton measured in monolayers at low temperature.

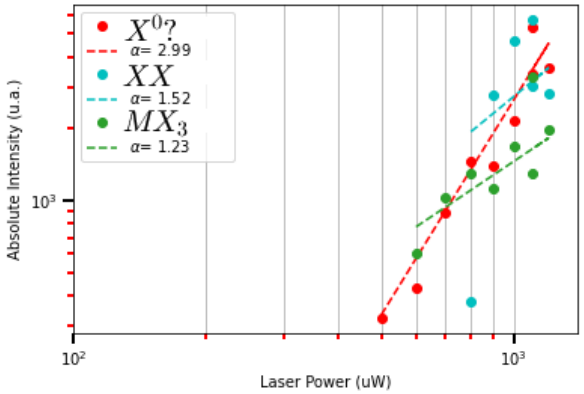

Figure 66: Integrated Intensity evolution of Zone 2 Intralayer emission under varying laser excitation power. Fitted to power law given in Equation 9.

The power dependence for Zone 2 is shown in Figure 66.a. Here, we can see how the XX peak fits to $\alpha \approx 1.52$, although given the low amount of measurements available for the fit, error in this fit is high. When fitting only the first part of the curve (from 800-1100 μW) $\alpha \approx 2.36$ is measured, giving us an upper bound on α. As we know from the analysis of zone 1, it is very probable that this is a biexciton due to its energy. For the X^0? peak, an α of 3 is fitted. This value is surprising, as a cubic dependence does not appear in previously reported papers. As the emission of this 1.72 eV (X^0?) exciton shows record narrow emission (Figure 61), in [70] it is discussed that an extremely narrow peak at the neutral exciton emission should be originated from a localized moiré exciton due to a moiré potential residing extremely close to the neutral exciton energy. Thus, we will refer to this emission as MX_5 from now on. Finally, MX_3 emission is fitted with an α of 1.23. The emission energy of this peak marks this exciton as a localized state or moiré exciton, however, it is surprising that it did not saturate even at high intensities, following the same dependence as a neutral exciton.

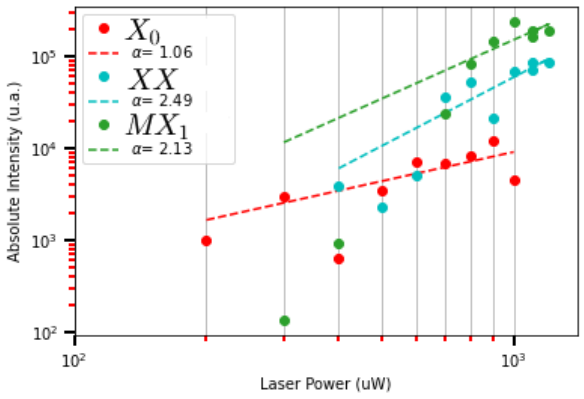

Figure 67: Integrated Intensity evolution of Zone 3 Intralayer emission under varying laser excitation power. Fitted to power law given in Equation 9.

The power dependence for Zone 3 is shown in Figure 67.a. Here, we can see how the X^0 peak fits to $\alpha \approx 1.06$, showing as in zone 1 a neutral intralayer exciton emission, as expected. For the XX peak, α is too high to be regarded as a biexciton as it is much higher 2, however, given that the exciton energy is around the previous experimental energy measured in monolayers, and the rough fitting applied in this work, α has a relatively high error in this curve as most of the spectra in sample 3 was heavily convoluted (Figure 62), this peak could be considered an intralayer biexciton XX. Finally, we fitted a high α MX_1 exciton. The emission energy of this peak marks this exciton as a localized state or moiré exciton (MX_1), however, it is surprising that it did not saturate even at high intensities and its square (up to fifth depending on number of measured points) power dependence.

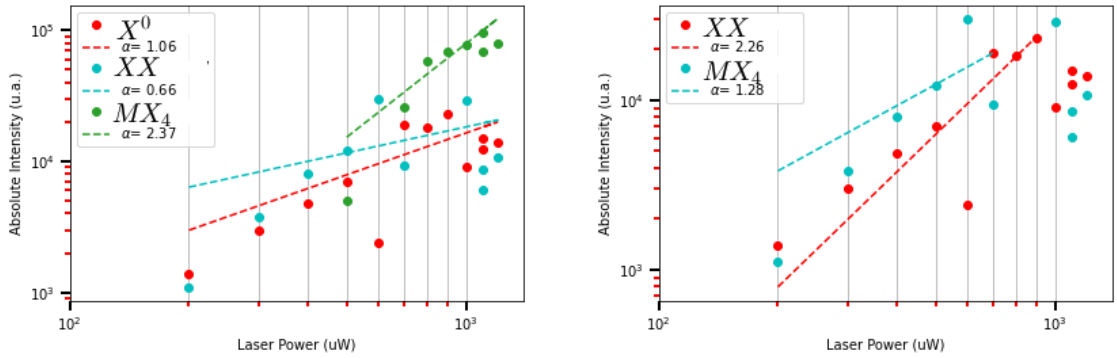

(a) *(b)*

Figure 68: Integrated Intensity evolution of Zone 4 Intralayer emission under varying laser excitation power. Fitted to power law given in Equation 9 for (a) all power, (b) power of less than $900\mu W$

The power dependence for Zone 4 is shown in Figure 68.a. Here, we can see how the X^0 peak fits to $\alpha \approx 1.06$, showing as in zone 1 a neutral intralayer exciton emission. For emission at XX, as in zone 1, emission saturates at high excitation power, however when studying the emission at lower power (Figure 68.b), α is around 2.26. Given this result, we can assume that it is a localized neutral exciton or moiré exciton MX_6. Lastly, the MX_4 exciton shows a high α which does not seem to saturate. As α is higher than 2, it seems implausible that it is a intralayer biexciton, however, its energy is high enough to not be regarded clearly as a localized state, thus we cannot find the origin of the MX_4 exciton with these limited measurements.

Given this analysis of the different zones, we are able to identify in most cases the neutral intralayer exciton X^0 (zones 1,3 and 4) and the biexciton XX (zones 1,2,3) with a sweep across different incident powers. Curiously, the 1.72 eV exciton emission in zone 2 did not come from a intralayer neutral exciton, but from a moiré exciton MX_5. There is also a plethora of diffient moiré localized excitons in each of the zones studied.

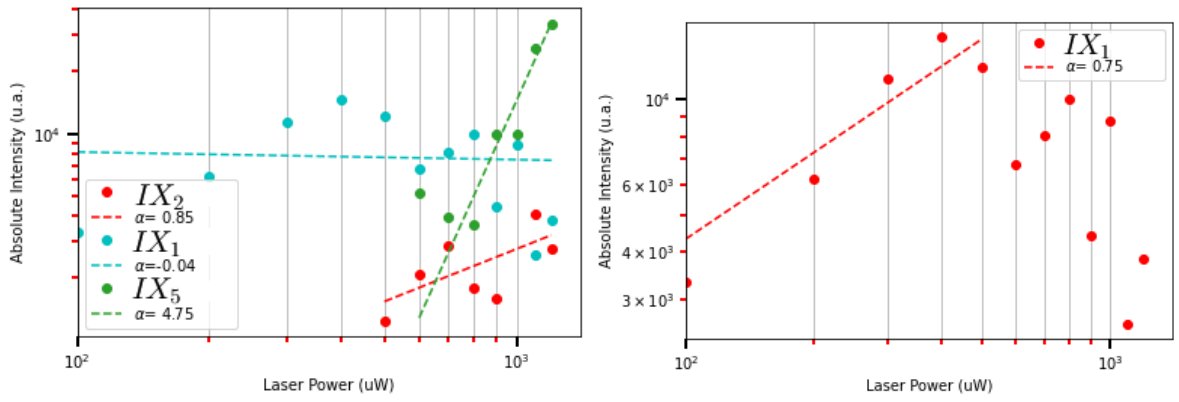

(a) *(b)*

Figure 69: Integrated Intensity evolution of Zone 1 Interlayer emission under varying laser excitation power. Fitted to power law given in Equation 9. (a) For all measured powers, (b) for power of less than $500\mu W$.

Now, we will study the interlayer emission for each of the zones. The power dependence for Zone 1 is shown in Figure 69.b. The IX_2 peak shows an almost lineal dependence ($\alpha \approx 0.85$) with excitation power, and being the highest energy exciton found, it is a good candidate to be regarded as a neutral interlayer exciton (IX^0). For the IX_1 peak, the exciton shows saturation at excitation power higher than 300 μW, denoting a localized exciton. When studying the emission at lower power (Figure 69), α is around 0.75 eV, thus the 1.45 eV (IX_1) peak is a moiré exciton (IMX_1). For the IX_5 peak, we fitted to an α of 4.75, an extremely high power dependence for excitonic emission, as its neighbour was a localized exciton, we will suppose this emission is also due a moiré exciton (IMX_5).

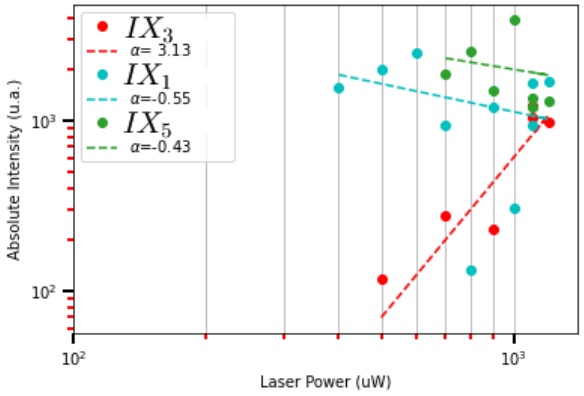

Figure 70: Integrated Intensity evolution of Zone 2 Interlayer emission under varying laser excitation power. Fitted to power law given in Equation 9.

The power dependence for Zone 2 is shown in Figure 70. Here, we can see how the IX_1 and IX_5 eV peaks fit to $\alpha < 0$, showing a clear saturation of the excitons. Thus, these two excitons are moiré excitons (IMX_1 and IMX_3). For the IX_3 exciton, an $\alpha \approx 3.1$ was measured, which complicates the analysis of its origin.

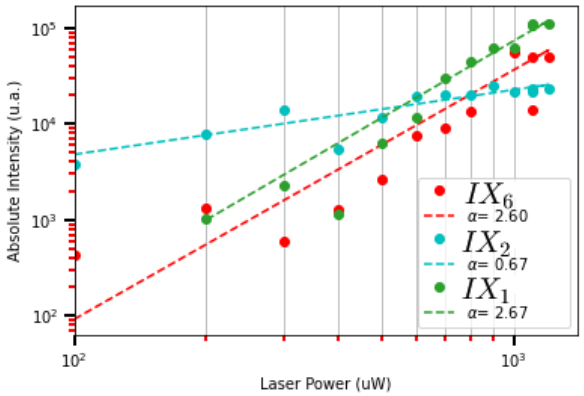

Figure 71: Integrated Intensity evolution of Zone 3 Interlayer emission under varying laser excitation power. Fitted to power law given in Equation 9.

For the power dependence of Zone 3, as shown in Figure 71, we can see how the IX_2 exciton shows a sublinear growth with excitation power, making it a candidate for a moiré excitonic emission (IMX_2). For the IX_1 and IX_6 excitons , as both show a supercuadratic dependence, a correct fit to a biexciton can not be achieved. However, due to its different

α compared to the interlayer exciton-biexciton complex [39], this emission might come from localized states present in our heterostructure (IMX_1 and IMX_6).

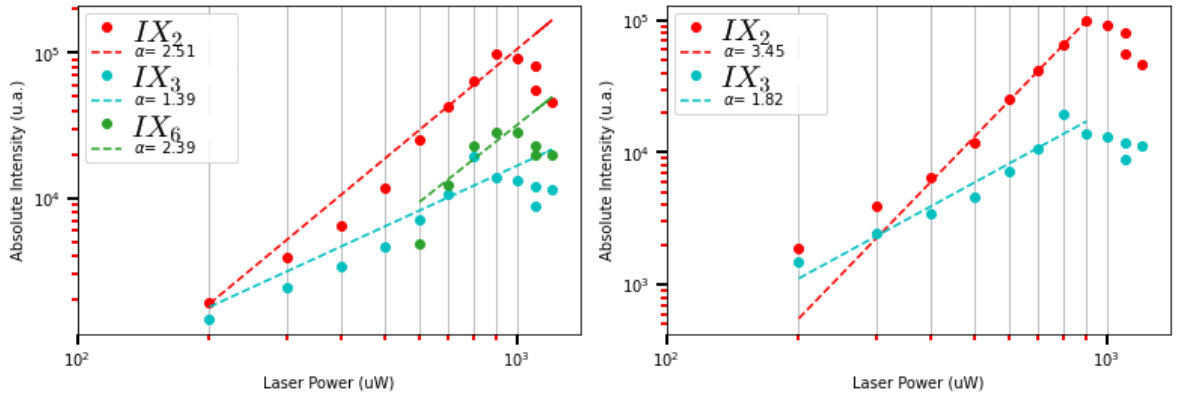

(a) *(b)*

Figure 72: Integrated Intensity evolution of Zone 4 Interlayer emission under varying laser excitation power. Fitted to power law given in Equation 9. (a) For all measured powers, (b) for power of less than $800\mu W$.

Lastly, for zone 4, as shown in Figure 72, the IX_3 exciton seems to follow a biexcitonic behaviour up to a saturation point, when studying the emission at lower power (Figure 72), α is around 1.82 eV, thus the 1.49 eV peak (IX_3) is an interlayer biexciton (IXX). For emission of peaks at IX_2 and IX_6 eV, the behaviour is the same as in Zone 3, this emission might come from localized states present in our heterostructure (IMX_2 and IMX_6).

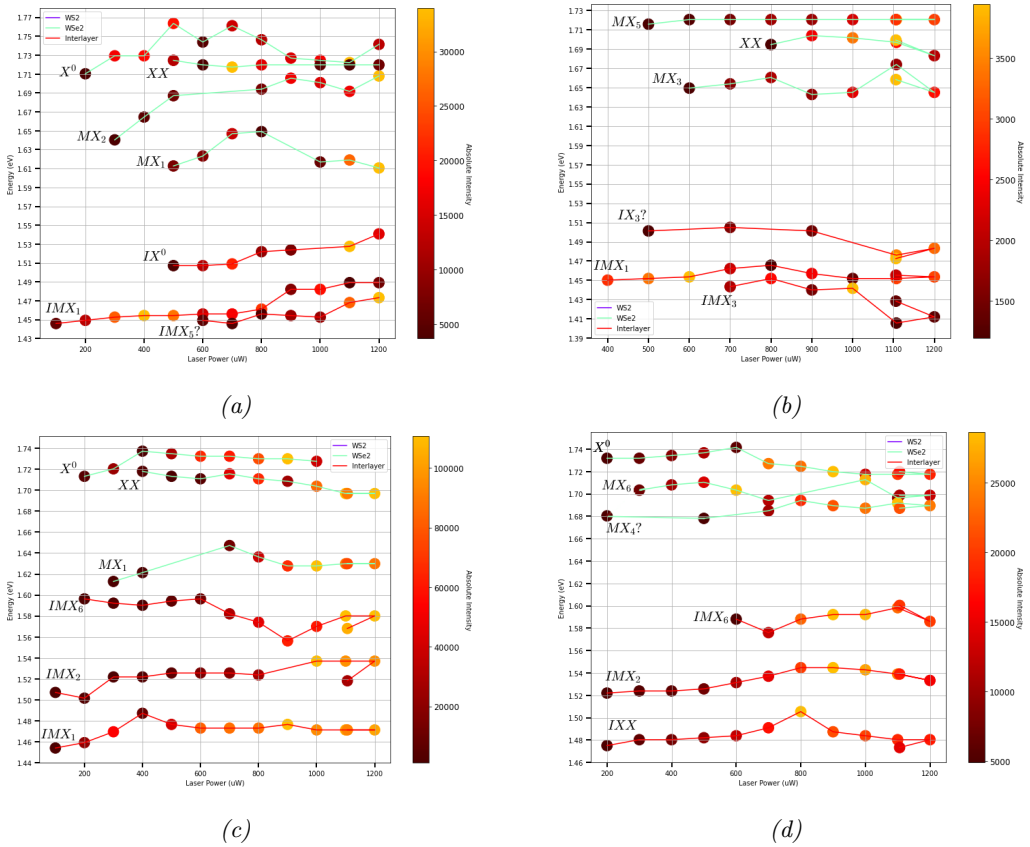

Figure 73: Exciton peak and evolution of each zone under varying laser excitation power. Color of the markers are given by their Integrated Intensity as shown in the heat bar. (a) Zone 1, (b) Zone 2, (c) Zone 3, (d) Zone 4. All identified excitons in this work are marked.

In summary, we are able to identify the intralayer excitonic complexes present in our heterostructure. We display these results in an updated fit to the evolution of the excitonic peaks in Figure 73. We find the 1.74-1.72 eV peak to be a neutral intralayer exciton X^0 (1.74eV in zone 1, 1.73eV in zone 3 and 1.72eV in zone 4, depending on zone energy shift), the 1.71-1.69 eV peak to be an intralayer biexciton XX (1.71 eV in in zone 3, 1.69 eV in zone 1, 1.70 in zone 2). We also find moiré excitons MX at different energies: 1.72 eV and 1.65 eV at zones 1, 2 and 3. These moiré excitons show different behaviours and dependence in respect to excitation laser power at different points of the sample. Meanwhile, there was a peak at 1.68 eV (MX_4) at zone 4 that could not be identified reliably, as it had a superlineal dependence with excitation power and its energy was too high.

For the interlayer excitonic complexes, identification was much more difficult. We were able to fit a 1.51 eV peak to a neutral interlayer exciton IX^0 at zone 1. Moiré excitons MIX_1 were found at 1.45 eV at zone 1, 1.44 eV and 1.46 eV at zone 2 and 1.47 eV at zone 3. A possible interlayer biexciton IXX was found at 1.49 eV at zone 4. For the rest of the peaks at each zone, the superlineal dependence hindered the identification of the excitonic complexes. However, it is highly likely that these excitons come from a moiré potential present in our heterostructure, as the energy was constant across zones at 1.51-1.53 eV (IMX_2) and 1.57-1.58 eV (IMX_6). Lastly, there was a peak at 1.44 eV (IMX_5) at zone 1 that could not be identified reliably, as it had an incredibly high superlineal dependence with excitation power. In order to properly identify them, Power Resolved Measurements with higher resolution in

a PL-Map with a $0.1\mu m$ step size should be conducted. With this approach, we will be able to study both the spatial dependence of the moiré pattern and the power dependence of the moiré excitons arising from this moiré pattern, giving us a great deal of information about the electronic structure of the sample. Additionally, by characterizing the lifetime of the excitons, we could help identify interlayer and moiré excitons, as interlayer excitons usually show high lifetimes while moiré excitons, being localized, show ultra-fast dynamics [71].

6 Conclusions

This master's thesis presents an exploration of interlayer excitons in $hBN/WSe_2/WS_2/hBN$ heterostructures, with a focus on their fabrication, optical characterization, and the phenomena of moiré excitons. This work offers insights into the complex interplay between structural, electronic, and optical properties in these two-dimensional (2D) van der Waals heterostructures and their potential applications in advanced optoelectronic devices.

The successful fabrication of $hBN/WSe_2/WS_2/hBN$ heterostructures was achieved through mechanical exfoliation and dry transfer techniques. Bulk crystals of hBN, WSe_2 and WS_2 were mechanically exfoliated using adhesive tape to produce WSe_2 and WS_2 monolayers and thin hBN flakes on a PDMS polymer.

To ensure high structural quality and minimize contamination, the heterostructures were assembled using a dry transfer method. This process involved the contact of the PDMS with the substrate in order for van der Waals forces to adhere the flake to the substrate. This process was repeated sequentially stacking each flake and monolayer onto the desired substrate. Hexagonal boron nitride (hBN) was employed as an encapsulating material.

Photoluminescence (PL) spectroscopy was employed as the tool to probe the optical emission properties of these heterostructures. Various analysis were conducted to study the effects of thermal annealing and the structural geometry of the heterostructures on their emission characteristics. The results showed that the optical emission properties were significantly influenced by the quality of hBN utilized and the structural arrangement of the TMD layers.

Thanks to these optical results and insight into high quality heterostructure fabrication, new processes are implemented for future research in heterostructures in the research group. The identification of problems due to the arrangement and annealing shown in this thesis will aid in the fabrication of new, high quality heterostructures in the research group, as this thesis was a proof of concept on the fabrication and characterization of heterostructures with the equipment of the group.

A significant part of this study was the observation and analysis of moiré excitons, arising from the periodic potential landscape created by the slight lattice mismatch, rotational misalignment and strain landscape between WSe_2 and WS_2 layers. Low-temperature experiments conducted at 4K revealed the formation of different species of intralayer and interlayer excitons within the heterostructures. The dependence of these excitons on incident power and polarization was studied, offering insights into their potential origins and implications for future electronic and optoelectronic devices. Given these insights we separated these excitons into interlayer neutral and biexcitons, and moiré excitons. These moiré excitons exhibited unique recombination dynamics and spectral features depending on their position on the moiré pattern, providing new insights into the interaction of excitons within the moiré potential.

In conclusion, this master thesis has investigated the properties of interlayer excitons in $hBN/WSe_2/WS_2/hBN$ heterostructures through fabrication and optical characterisation studies. The identification and analysis of moiré excitons represents a significant advance in the understanding of the complex behaviour of excitons in 2D materials. This work lays a foundation for future research aimed at exploiting the unique properties of interlayer and moiré excitons in TMD heterostructures.

References

[1] Charles Kittel. *Introduction to solid state physics*. Ed. by Paul McEuen. Global edition, [9th edition]. Hoboken, NJ: Wiley, 2018. 692 pp. ISBN: 9781119454168.

[2] S. M. Sze and Kwok Kwok Ng. *Physics of semiconductor devices*. 3. ed. Wiley-Interscience online books. Hoboken, N.J: Wiley-Interscience, 2007. 1815 pp. ISBN: 9780585315508.

[3] Sidney Perkowitz. *Optical characterization of semiconductors. Infrared, Raman, and photoluminescence spectroscopy*. 2. printing. Techniques of physics 14 [i.e. 15]. Zählung lt. der der Haupttitels. gegenüberliegenden S., vom Verl. doppelt vergeben. London [u.a.]: Acad. Press, 1994. 220 pp. ISBN: 0125507704.

[4] Gabriele Grosso et al. "Tunable and high-purity room temperature single-photon emission from atomic defects in hexagonal boron nitride". In: *Nature Communications* 8.1 (Sept. 2017). ISSN: 2041-1723. DOI: 10.1038/s41467-017-00810-2.

[5] Vigneshwaran Shanmugam et al. "A Review of the Synthesis, Properties, and Applications of 2D Materials". In: *Particle Systems Characterization* 39.6 (May 2022). ISSN: 1521-4117. DOI: 10.1002/ppsc.202200031.

[6] Kai Liu et al. "Elastic Properties of Chemical-Vapor-Deposited Monolayer MoS2, WS2, and Their Bilayer Heterostructures". In: *Nano Letters* 14.9 (Aug. 2014), pp. 5097–5103. DOI: 10.1021/nl501793a.

[7] Mayank Garg et al. "Different Types and Intense Classification of 2D Materials". In: *Advanced Applications of 2D Nanostructures*. Springer Singapore, 2021, pp. 11–28. ISBN: 9789811633225. DOI: 10.1007/978-981-16-3322-5_2.

[8] Kamalika Ghatak et al. "Controlled edge dependent stacking of WS2-WS2 Homo- and WS2-WSe2 Hetero-structures: A Computational Study". In: *Scientific Reports* 10.1 (Feb. 2020). ISSN: 2045-2322. DOI: 10.1038/s41598-020-58149-6.

[9] A. Yu. Ledneva et al. "Crystalline and nanostructured materials based on transition metal dichalcogenides: synthesis and electronic properties". In: *Journal of Structural Chemistry* 63.2 (Feb. 2022), pp. 176–226. ISSN: 1573-8779. DOI: 10.1134/s0022476622020020.

[10] Weijie Zhao et al. "Evolution of Electronic Structure in Atomically Thin Sheets of WS2 and WSe2". In: *ACS Nano* 7.1 (Dec. 2012), pp. 791–797. DOI: 10.1021/nn305275h.

[11] Long Yuan and Libai Huang. "Exciton dynamics and annihilation in WS2 2D semiconductors". In: *Nanoscale* 7.16 (2015), pp. 7402–7408. ISSN: 2040-3372. DOI: 10.1039/c5nr00383k.

[12] A. Kuc, N. Zibouche, and T. Heine. "Influence of quantum confinement on the electronic structure of the transition metal sulfideTS2". In: *Physical Review B* 83.24 (June 2011), p. 245213. ISSN: 1550-235X. DOI: 10.1103/physrevb.83.245213.

[13] Zongyou Yin et al. "Single-Layer MoS2Phototransistors". In: *ACS Nano* 6.1 (Dec. 2011), pp. 74–80. ISSN: 1936-086X. DOI: 10.1021/nn2024557.

[14] Oriol Lopez-Sanchez et al. "Ultrasensitive photodetectors based on monolayer MoS2". In: *Nature Nanotechnology* 8.7 (June 2013), pp. 497–501. ISSN: 1748-3395. DOI: 10.1038/nnano.2013.100.

[15] Marco M. Furchi et al. “Photovoltaic Effect in an Electrically Tunable van der Waals Heterojunction”. In: *Nano Letters* 14.8 (July 2014), pp. 4785–4791. ISSN: 1530-6992. DOI: 10.1021/nl501962c.

[16] Matin Amani et al. “Near-unity photoluminescence quantum yield in MoS 2”. In: *Science* 350.6264 (Nov. 2015), pp. 1065–1068. ISSN: 1095-9203. DOI: 10.1126/science.aad2114.

[17] Ting Cao et al. “Valley-selective circular dichroism of monolayer molybdenum disulphide”. In: *Nature Communications* 3.1 (June 2012). ISSN: 2041-1723. DOI: 10.1038/ncomms1882.

[18] Philipp Tonndorf et al. “Single-photon emission from localized excitons in an atomically thin semiconductor”. In: *Optica* 2.4 (Apr. 2015), p. 347. ISSN: 2334-2536. DOI: 10.1364/optica.2.000347.

[19] Thomas Mueller and Ermin Malic. “Exciton physics and device application of two-dimensional transition metal dichalcogenide semiconductors”. In: *npj 2D Materials and Applications* 2.1 (Sept. 2018). ISSN: 2397-7132. DOI: 10.1038/s41699-018-0074-2.

[20] Andrew Yunho Joe. “Interlayer Excitons in Atomically Thin van der Waals Semiconductor Heterostructures”. PhD thesis. Harvard University, 2021. URL: https://nrs.harvard.edu/URN-3:HUL.INSTREPOS:37368459.

[21] Ashwin Ramasubramaniam. “Large excitonic effects in monolayers of molybdenum and tungsten dichalcogenides”. In: *Physical Review B* 86.11 (Sept. 2012), p. 115409. ISSN: 1550-235X. DOI: 10.1103/physrevb.86.115409.

[22] Yilei Li et al. “Measurement of the optical dielectric function of monolayer transition-metal dichalcogenides:MoS2,MoSe2,WS2, andWSe2”. In: *Physical Review B* 90.20 (Nov. 2014), p. 205422. ISSN: 1550-235X. DOI: 10.1103/physrevb.90.205422.

[23] Jeongwoon Hwang et al. “Giant renormalization of dopant impurity levels in 2D semiconductor MoS2”. In: *Scientific Reports* 10.1 (Mar. 2020). ISSN: 2045-2322. DOI: 10.1038/s41598-020-61675-y.

[24] Ilkka Kylänpää and Hannu-Pekka Komsa. “Binding energies of exciton complexes in transition metal dichalcogenide monolayers and effect of dielectric environment”. In: *Physical Review B* 92.20 (Nov. 2015), p. 205418. ISSN: 1550-235X. DOI: 10.1103/physrevb.92.205418.

[25] Yuan Liu et al. “Van der Waals heterostructures and devices”. In: *Nature Reviews Materials* 1.9 (July 2016). ISSN: 2058-8437. DOI: 10.1038/natrevmats.2016.42.

[26] Hongxia Zhong et al. “Broken-gap type-III band alignment in monolayer halide perovskite/antiperovskite oxide van der Waals heterojunctions”. In: *Nanoscale* 15.27 (2023), pp. 11560–11568. ISSN: 2040-3372. DOI: 10.1039/d3nr00676j.

[27] Nicholas R. Glavin and SungWoo Nam. “2D layered materials and heterostructures: Past, present, and a bright future”. In: *Matter* 6.1 (Jan. 2023), pp. 4–6. ISSN: 2590-2385. DOI: 10.1016/j.matt.2022.11.030.

[28] Prasana K. Sahoo et al. “One-pot growth of two-dimensional lateral heterostructures via sequential edge-epitaxy”. In: *Nature* 553.7686 (Jan. 2018), pp. 63–67. ISSN: 1476-4687. DOI: 10.1038/nature25155.

[29] Jun-Ho Lee et al. “Semiconductor-less vertical transistor with ION/IOFF of 106”. In: *Nature Communications* 12.1 (Feb. 2021). ISSN: 2041-1723. DOI: 10.1038/s41467-021-21138-y.

[30] Suman Kumar Chakraborty et al. “Challenges and opportunities in 2D heterostructures for electronic and optoelectronic devices”. In: *iScience* 25.3 (Mar. 2022), p. 103942. ISSN: 2589-0042. DOI: 10.1016/j.isci.2022.103942.

[31] A. K. Geim and I. V. Grigorieva. “Van der Waals heterostructures”. In: *Nature* 499.7459 (July 2013), pp. 419–425. ISSN: 1476-4687. DOI: 10.1038/nature12385.

[32] Yuanyue Liu, Paul Stradins, and Su-Huai Wei. “Van der Waals metal-semiconductor junction: Weak Fermi level pinning enables effective tuning of Schottky barrier”. In: *Science Advances* 2.4 (Apr. 2016). ISSN: 2375-2548. DOI: 10.1126/sciadv.1600069.

[33] Junho Choi et al. “Twist Angle-Dependent Interlayer Exciton Lifetimes in van der Waals Heterostructures”. In: *Physical Review Letters* 126.4 (Jan. 2021), p. 047401. ISSN: 1079-7114. DOI: 10.1103/physrevlett.126.047401.

[34] Pasqual Rivera et al. “Interlayer valley excitons in heterobilayers of transition metal dichalcogenides”. In: *Nature Nanotechnology* 13.11 (Aug. 2018), pp. 1004–1015. ISSN: 1748-3395. DOI: 10.1038/s41565-018-0193-0.

[35] Hongyi Yu et al. “Anomalous Light Cones and Valley Optical Selection Rules of Interlayer Excitons in Twisted Heterobilayers”. In: *Physical Review Letters* 115.18 (Oct. 2015), p. 187002. ISSN: 1079-7114. DOI: 10.1103/physrevlett.115.187002.

[36] Yuan Cao et al. “Unconventional superconductivity in magic-angle graphene superlattices”. In: *Nature* 556.7699 (Mar. 2018), pp. 43–50. ISSN: 1476-4687. DOI: 10.1038/nature26160.

[37] Dacen Waters. “Moiré, Interlayer, and Proximity Effects in 2D van der Waals Heterostructures”. PhD thesis. 2022. DOI: 10.1184/R1/18863630.V1.

[38] Johannes Maria Holler. “Optical spectroscopy of van der Waals heterostructures”. PhD thesis. 2021. DOI: 10.5283/EPUB.51079.

[39] Chenhao Jin et al. “Observation of moiré excitons in WSe2/WS2 heterostructure superlattices”. In: *Nature* 567.7746 (Feb. 2019), pp. 76–80. ISSN: 1476-4687. DOI: 10.1038/s41586-019-0976-y.

[40] Paul Cazeaux et al. “Relaxation and Domain Wall Structure of Bilayer Moiré Systems”. In: *Journal of Elasticity* 154.1–4 (Apr. 2023), pp. 443–466. ISSN: 1573-2681. DOI: 10.1007/s10659-023-10013-0.

[41] Jie Sun et al. “Synthesis Methods of Two-Dimensional MoS2: A Brief Review”. In: *Crystals* 7.7 (July 2017), p. 198. DOI: 10.3390/cryst7070198.

[42] Yuchun Liu and Fuxing Gu. “A wafer-scale synthesis of monolayer MoS2 and their field-effect transistors toward practical applications”. In: *Nanoscale Advances* 3.8 (2021), pp. 2117–2138. DOI: 10.1039/d0na01043j.

[43] Yangang Li et al. “Recent progress on the mechanical exfoliation of 2D transition metal dichalcogenides”. In: *Materials Research Express* 9.12 (Dec. 2022), p. 122001. ISSN: 2053-1591. DOI: 10.1088/2053-1591/aca6c6.

[44] Achint Jain et al. “Minimizing residues and strain in 2D materials transferred from PDMS”. In: *Nanotechnology* 29.26 (May 2018), p. 265203. DOI: 10.1088/1361-6528/aabd90.

[45] Kei Kinoshita et al. “Dry release transfer of graphene and few-layer h-BN by utilizing thermoplasticity of polypropylene carbonate”. In: *npj 2D Materials and Applications* 3.1 (May 2019). DOI: 10.1038/s41699-019-0104-8.

[46] Mitsuhiro Okada et al. “Direct and Indirect Interlayer Excitons in a van der Waals Heterostructure of hBN/WS2/WSe2/hBN heterostructures”. In: *ACS Nano* 12.3 (Feb. 2018), pp. 2498–2505. DOI: 10.1021/acsnano.7b08253.

[47] Mengqi Zhu et al. “Exchange between Interlayer and Intralayer Exciton in WSe2/WS2 Heterostructure by Interlayer Coupling Engineering”. In: *Nano Letters* 22.11 (May 2022), pp. 4528–4534. DOI: 10.1021/acs.nanolett.2c01353.

[48] Tong Ye, Junze Li, and Dehui Li. “Charge-Accumulation Effect in Transition Metal Dichalcogenide Heterobilayers”. In: *Small* 15.42 (Aug. 2019), p. 1902424. DOI: 10.1002/smll.201902424.

[49] Yingnan Liu et al. “Thermal Oxidation of WSe2 Nanosheets Adhered on SiO2/Si Substrates”. In: *Nano Letters* 15.8 (July 2015), pp. 4979–4984. ISSN: 1530-6992. DOI: 10.1021/acs.nanolett.5b02069.

[50] M. Fischer et al. “Controlled generation of luminescent centers in hexagonal boron nitride by irradiation engineering”. In: *Science Advances* 7.8 (Feb. 2021). ISSN: 2375-2548. DOI: 10.1126/sciadv.abe7138.

[51] Pasqual Rivera et al. “Observation of long-lived interlayer excitons in monolayer MoSe2–WSe2 heterostructures”. In: *Nature Communications* 6.1 (Feb. 2015). ISSN: 2041-1723. DOI: 10.1038/ncomms7242.

[52] Juan Yu et al. “Observation of double indirect interlayer exciton in WSe2/WS2 heterostructure”. In: *Optics Express* 28.9 (Apr. 2020), p. 13260. DOI: 10.1364/oe.392052.

[53] Taishen Li et al. *Magnetically-Sensitive Valley Polarization Reversal and Revival of Defect-Localized Excitons in WSe2-WS2*. 2019. DOI: 10.48550/ARXIV.1903.06899.

[54] Zhuofa Chen et al. “Charge Separation in Monolayer WSe2 by Strain Engineering: Implications for Strain-Induced Diode Action”. In: *ACS Applied Nano Materials* 5.10 (Oct. 2022), pp. 15095–15101. ISSN: 2574-0970. DOI: 10.1021/acsanm.2c03264.

[55] M. Kögl et al. “Moiré straintronics: a universal platform for reconfigurable quantum materials”. In: *npj 2D Materials and Applications* 7.1 (Apr. 2023). ISSN: 2397-7132. DOI: 10.1038/s41699-023-00382-4.

[56] Philipp Nagler et al. “Interlayer Excitons in Transition-Metal Dichalcogenide Heterobilayers”. In: *physica status solidi (b)* 256.12 (Nov. 2019). ISSN: 1521-3951. DOI: 10.1002/pssb.201900308.

[57] Cuihuan Ge et al. “Modulating interlayer and intralayer excitons in WS2/WSe2 van der Waals heterostructures”. In: *AIP Advances* 13.11 (Nov. 2023). ISSN: 2158-3226. DOI: 10.1063/5.0159723.

[58] Chendong Zhang et al. “Interlayer couplings, Moiré patterns, and 2D electronic superlattices in MoS 2 /WSe 2 hetero-bilayers”. In: *Science Advances* 3.1 (Jan. 2017). ISSN: 2375-2548. DOI: 10.1126/sciadv.1601459.

[59] C. R. Zhu et al. “Exciton valley dynamics probed by Kerr rotation inWSe2monolayers”. In: *Physical Review B* 90.16 (Oct. 2014), p. 161302. ISSN: 1550-235X. DOI: 10.1103/physrevb.90.161302.

[60] Jingzhi Shang et al. “Observation of Excitonic Fine Structure in a 2D Transition-Metal Dichalcogenide Semiconductor”. In: *ACS Nano* 9.1 (Jan. 2015), pp. 647–655. ISSN: 1936-086X. DOI: 10.1021/nn5059908.

[61] Matteo Barbone et al. “Charge-tuneable biexciton complexes in monolayer WSe2”. In: *Nature Communications* 9.1 (Sept. 2018). ISSN: 2041-1723. DOI: 10.1038/s41467-018-05632-4.

[62] I. Paradisanos et al. “Room temperature observation of biexcitons in exfoliated WS2 monolayers”. In: *Applied Physics Letters* 110.19 (May 2017). ISSN: 1077-3118. DOI: 10.1063/1.4983285.

[63] Xueqian Sun et al. “Enhanced interactions of interlayer excitons in free-standing heterobilayers”. In: *Nature* 610.7932 (Oct. 2022), pp. 478–484. ISSN: 1476-4687. DOI: 10.1038/s41586-022-05193-z.

[64] Biao Wu et al. “Evidence for moiré intralayer excitons in twisted WSe2/WSe2 homobilayer superlattices”. In: *Light: Science ; Applications* 11.1 (June 2022). ISSN: 2047-7538. DOI: 10.1038/s41377-022-00854-0.

[65] Keisuke Shinokita et al. “Resonant Coupling of a Moiré Exciton to a Phonon in a WSe2/MoSe2 Heterobilayer”. In: *Nano Letters* 21.14 (July 2021), pp. 5938–5944. ISSN: 1530-6992. DOI: 10.1021/acs.nanolett.1c00733.

[66] Haihong Zheng et al. “Moiré Enhanced Potentials in Twisted Transition Metal Dichalcogenide Trilayers Homostructures”. In: *Small* 19.26 (Mar. 2023). ISSN: 1613-6829. DOI: 10.1002/smll.202207988.

[67] Zhipeng Li et al. “Revealing the biexciton and trion-exciton complexes in BN encapsulated WSe2”. In: *Nature Communications* 9.1 (Sept. 2018). ISSN: 2041-1723. DOI: 10.1038/s41467-018-05863-5.

[68] Bastian Miller et al. “Long-Lived Direct and Indirect Interlayer Excitons in van der Waals Heterostructures”. In: *Nano Letters* 17.9 (Aug. 2017), pp. 5229–5237. ISSN: 1530-6992. DOI: 10.1021/acs.nanolett.7b01304.

[69] Youngsin Park et al. “Carrier trapping and confinement in Ge nanocrystals surrounded by Ge3N4”. In: *Scientific Reports* 6.1 (May 2016). ISSN: 2045-2322. DOI: 10.1038/srep25449.

[70] Kyle L. Seyler et al. “Signatures of moiré-trapped valley excitons in MoSe2/WSe2 heterobilayers”. In: *Nature* 567.7746 (Feb. 2019), pp. 66–70. ISSN: 1476-4687. DOI: 10.1038/s41586-019-0957-1.

[71] Jan Philipp Bange et al. “Ultrafast dynamics of bright and dark excitons in monolayer WSe2 and heterobilayer WSe2/MoS2”. In: *2D Materials* 10.3 (July 2023), p. 035039. ISSN: 2053-1583. DOI: 10.1088/2053-1583/ace067.